広島大学学位請求論文

Crystallization of Stratlingite in High Alumina Cement Hydrates

with Silica Fume at Different Curing Temperatures and Terms

異なる養生温度と養生期間に於けるシリカフュームを添加した

ハイアルミナセメント水和物中のストラトリンジャイトの結晶化について

2016年

広島大学大学院理学研究科

地球惑星システム学専攻

新名　俊夫

目　次

1．主論文

Crystallization of Stratlingite in High Alumina Cement Hydrates with Silica Fume at Different Curing Temperatures and Terms

異なる養生温度と養生期間に於けるシリカフュームを添加したハイアルミナセメント水和物中のストラトリンジャイトの結晶化について

2．公表論文

(1) Stratlingite in Hydrate of High-Alumina Cement with Silica Fume

Toshio Shinmei, Yasuhiro Shibata, Makio Ohkawa, Ryuji Kitagawa and Mayumi Jige.

Journal of the Technical Association of Refractories, Japan, Vol.31, No. 4, PP. 237-241, 2011.

(2) Crystallization of Stratlingite in a High Alumina Cement – Silica Fume System with or without Deflocculant

Toshio Shinmei, Makio Ohkawa, Adriana Borovsky, Makoto Iiyama, Chris Parr.

Journal of the Technical Association of Refractories, Japan, Vol.32, No. 1, PP. 3-11, 2012.

(3) Effect of CO_2 gas on Crystallization of C_2ASH_8 (stratlingite) in a High Alumina Cement with Silica Fume

Toshio Shinmei, Makio Ohkawa, Adriana Borovsky, Makoto Iiyama, Chris Parr.

Journal of the Technical Association of Refractories, Japan, Vol.32, No. 3, PP. 188-193, 2012.

(4) The effect of curing temperature of the high alumina cement on the crystallization of stratlingite: In the case of curing temperatures of 10 °C and 60 °C

Toshio Shinmei, Makio Ohkawa, Makoto Iiyama, Christoph Wöhmeyer, Chris Parr.

Journal of Mineralogical and Petrological Sciences, Vol. 110, PP. 92-95, 2015.

(5) ハイアルミナセメント水和物中のストラトリンジャイトの結晶化と温度依存性：養生温度 50℃及び 30℃の場合

The dependence of curing temperature on the crystallization of Stratlingite in the high alumina cement hydrates : In the case of curing temperatures at 50 °C and 30 °C

新名俊夫, 大川真紀雄, Christoph Wöhmeyer, 飯山眞人, Chris Parr.

耐火物　第 67 巻　第 10 号　503-511 頁　2015 年 10 月.

Content of the thesis

Crystallization of Stratlingite in High Alumina Cement Hydrates with Silica Fume at Different Curing Temperatures and Terms

異なる養生温度と養生期間に於けるシリカフュームを添加した
ハイアルミナセメント水和物中のストラトリンジャイトの結晶化について

新名　俊夫　（Toshio Shinmei）

Chapter I

Introduction

Chapter II

Experimental

Chapter III

Results

主論文

Chapter I

INTRODUCTION

I.1 Stratlingite

Stratlingite is a calcium silico-aluminate hydrate, named after W. Strätling who synthesized the material in 1938. Hentschel and Kuzel (1976) was the first to describe a mineral of similar chemistry occurring in the metamorphosed limestone xenolith included in basalt from Bellerberg volcano near Mayen, Eifel, Germany. This new mineral was named in 1977 as stratlingite

It is also known that stratlingite is observed in many blended cements. Stratlingite is a constituent hydrate of the bonding matrix in low cement castable (LCC), one of the monolithic or unshaped castable refractories. Since the early 1980s, many research works were carried out on the crystallization behavior of stratlingite in the high alumina cement (HAC) hydrates (e.g. Eguchi et al., 1989; Pivinskii, 1998; Lee and Moor, 1998; Daspoddar et al., 2003; Antonovic et al., 2010). The common characteristic of all the HAC types of cement is that the reactive phases and hydrates formed are calcium aluminates (Scrivener and Capmas, 1998). However, there still remain some unclear problems of the crystallization of stratlingite. The fundamental knowledge and the history of refractory are described in the following sections, which will help to explain the purpose of the present study.

I.2 Classification of refractory

Refractory can be broadly classified into two types: shaped refractories (fired bricks) and monolithic (or unshaped) refractories. Table 1 shows the Japanese classification of refractories. The shaped refractories include common bricks and

brick shapes, and have been widely used for furnaces or ovens and as linings in boilers and stacks. On the other hand, monolithic refractories can be formed and shaped on site (Lee and Moor, 1989).

LCC has been developed from castable refractories which belong to monolithic refractories (Pivinskii 1998). Generally, calcium aluminate cement (CAC: often called high alumina cement, HAC) is used as a bonding material in castable refractories. Siliceous material, particularly silica fume (SF), is added to the LCC with a deflocculant. Castable refractories, including LCC exhibits plasticity when mixed with water, and can be casted into a mold. Therefore, it is easy to build a furnace at the installation site.

Monocalcium aluminate ($CaO \cdot Al_2O_3$, hereafter referred to as CA) that is the principal constituting phase of CAC, causes a hydration reaction with additive water. The reaction is completed commonly within one day (Kondo, 1968), and the quality of hydrated products is sensitive to the curing temperature (Parr, 2005). Further chemical reactions are affected by the environmental conditions, including humidity, temperature and the elapsed time after production (Parr et al. 2005, Table 2). CAC has the following characteristics: rapid setting and hardening, high strength and chemical corrosion resistance (Scrivener and Capmas, 1998), and hence has been used as binders for common structural concrete.

I.3 Development of castable refractories

Modern refractory technology is considered to have begun during the era of the Industrial Revolution. CAC, and its industrial productions were patented by Soc, J. & Pavin, A. of Lafarge in 1908. Its first industrial production was

commenced by the same company in 1913. The production of refractory castables using CAC as a binder was started in the United States in 1929. In Japan, the most remarkable progress of making CAC took place after World War II. Two manufacturers specialized in the production of refractory castables, NICHIBEIROZAI and NIHON REFRACTORY, were established in 1953 and 1954, respectively (The Pedigree of Tokyo Kogyo, 1997; Nishikawa, 1999). Subsequently, refractory bricks were replaced by monolithic refractories. During the period of economic development, the relationship between the material properties and the performance of the refractory castables in different conditions of use became gradually clear. Consequently, the methodologies for material design in consideration of conditions of use and development of new materials were established (Pivinskii, 1998; Lee and Moor, 1998). Eventually, the production volumes of monolithic refractories overtook those of the traditional refractory bricks from 1993 in Japan (The Association of Refractories, Japan, (2001)). Recently, the mainstream of the monolithic refractories shifts from conventional castables to LCC.

I.4 Low cement castables (LCC)

The two-stage oil crises in the 1970s had extremely serious effects on refractory technology worldwide. In Japan, the skyrocketing price of raw materials caused the manufacturers to reduce the amount of CAC used in the castable, and at the same time many researchers started to aim at the performance enhancement of the castable. Consequently, the LCC containing the ultrafine particles and deflocculating additives were developed. With further development of refractory technology, the shape and properties of refractory

products have become diverse. The technology also exerts a positive influence on the resource saving, energy conservation and environmental protection.

The CAC had been used in the construction industry until the early 1970s for the reason of having the properties of fast hardening, high early strength, better corrosion resistance to seawater, and excellent acid resistance. However, the negative effects have also been revealed. The concrete using CAC as a single binder loses strength with time. This phenomenon caused the serious structural collapses in U.K. and Spain. When CA, the main constituent phase of CAC, is mixed with water, initially metastable hydrates, hexagonal $CaO \cdot Al_2O_3 \cdot 10H_2O$ (CAH_{10}) and $2CaO \cdot Al_2O_3 \cdot 8H_2O$ (C_2AH_8), are crystalized and then convert to the stable and dense hydrate, cubic $3CaO \cdot Al_2O_3 \cdot 6H_2O$ (C_3AH_6: hydrogarnet) (Parr et al., 2005). The cause of the structural collapses was due to the strength reduction induced by cracks (Concr. Soc. Working Party, 1997) generated during the above conversion accompanied by a change of volume and density. Therefore, many researchers have studied how to avoid this conversion (Edmonds and Majumdar, 1989; Bentsen et al., 1990；Majumdar and Singh, 1992; Richard et al., 1993; Rayment and Majumdar, 1994; Ding et al., 1995, 1996a, 1996b; Fu et al., 1996, 1997; Heikal et al., 2004, 2005, 2015).

Comparative studies of the hydration of CAC in the presence of C-S-H gel (calcium silicate hydrate gel) or β-C_2S (β-$2CaO \cdot SiO_2$) with varying degrees of fineness were reported (Midgley and Rao, 1978; Rao and Viswanathan, 1980). They observed that the metastable calcium aluminate hydrates could react with the C-S-H gel to form stratlingite (C_2ASH_8). The amount of stratlingite formed was dependent on the availability of C-S-H gel for reaction. The use of a siliceous material in combination with a sodium salt in CAC was recently

reported to be more effective than the siliceous material alone in order to promote the formation of stratlingite (Edmonds and Majumdar, 1989; Majumdar and Singh, 1992; Ding et al., 1995; Fu et al., 1997) instead of hydrogarnet (Ding et al., 1995, 1996a; Fu et al., 1996). Siliceous materials, including natural zeolites (Ding et al., 1996b; Fu et al., 1996), fly ash (Fu et al., 1997; Fernández-Carrasco and Vázquez, 2009; López et al., 2008), slag (Edmonds and Majumdar, 1989; Majumdar et al., 1990a, 1990b; Fentiman et al., 1990; Richardoson and Groves, 1990; Majumdar and Singh, 1992; Fu et al., 1997; Heikal et al., 2004, 2005, 2015; Rayment and Majumdar, 1994), silica fume (SF) (Bentsen et al., 1990； Ding et al., 1995; Fu et al., 1997) and colloidal silica (Richard et al., 1993) were effective in inhibiting the hydrogarnet formation and preventing strength reduction of CAC products when added in combination with a sodium salt (Ding et al., 1995; Fu et al., 1996; Fernandez-Jimenez et al., 2011). In particular, the SF has been reported to favor the formation of stratlingite (Fig. 1, Bentsen et al., 1990). The SF reacts to form silicates in a high pH environment. This reaction is accelerated in the presence of an increased amount of alkali ions acting as a catalyst activating surfaces of SF. Silicate anions then react with hydrated calcium aluminates to produce stratlingite (Ding et al., 1995). Although the chemical analyses of stratlingite in castables or hydrations of CAC had been reported by many researchers, the reported chemical data of stratlingite show non-uniform compositions (Richardson and Groves, 1990; Lopez et al., 2008; García-Lodeiro et al., 2010).

I.5 Role of stratlingite in CAC hydrates

Many researchers reported that the formation of stratlingite is a function of

controlling the C_3AH_6 conversion (Majumdar et al., 1990a; Majumdar and Singh, 1992; Fu et al., 1996, 1997). For example, the building of Trajan's Market in Rome has been saved from the past three giant earthquakes during more than 2,000 years, Jackson et al. (2009) reported that the stratlingite formation is helpful to keep strength of the building. Jackson et al. (2014) described that stratlingite crystals evidently played a role in impeding the propagation of microcracks in Roman architectural mortar, which has the similar effect as that of polypropylene microfibers with low elastic modulus interground with cement in present-day mortars. Moreover, platy stratlingite crystals toughen interfacial zones along scoria perimeters and impede macroscale propagation of crack segments. The study of stratlingite crystallized in a concrete was conducted in order to develop the shell to cover a nuclear power reactor (Boch et al., 1992) after the Chernobyl incident. Boch et al. (1992) also reported that stratlingite can trap radioactive cesium released by nuclear accident. Furthermore, studies continued thereafter on the formations of stratlingite in concrete, which seals radioactive wastes in order to maintain a stable state over a long term (Sharp et al., 2003; Yoshino et al., 2009). However, there are few previous studies that treated the formation process of ever-changing constituent minerals (Majumdar et al., 1989, 1990a, 1990b, 1992; Singh et al., 1999).

The surface area of cement paste made of calcium aluminate cement with water is much more subjected to different chemical alterations, such as efflorescence, than its interior. The white crystals of $CaCO_3$ are formed by a chemical reaction between calcium in LCC hydrates and carbon dioxide in the atmosphere. The LCC contains the calcium aluminate hydrates such as CAH_{10}, C_2AH_8, C_4AH_{13}, C_4AcH_{11}, C_3AH_6, and C_2ASH_8 (stratlingite) (Bentsen et al.,

1990; Majumdar et al., 1989; Shinmei et al., 2012). However, the phase transitions of constituent minerals with time at the surface is unknown.

I.6 Purpose of this study

In the present work, the nature, sequence, composition and microstructure of hydrated phases present in cement pastes consisting of CAC and SF with and without deflocculant at different curing temperatures (10, 21, 23, 30, 35 50 and 60 °C) were analyzed using X-ray diffractometer (XRD) and electron probe microanalyzer (EPMA). Evolution of the cement paste hydration and the cause of changes in the hydrates in sealed glass bottles and spread on slide glasses were investigated. In addition, chronological observations of the surface of the cement paste samples spread on slide glasses were carried out to understand the effects of carbonation process on the above-mentioned hydrates. The special emphases given in this study are to reveal the following points:

1. Crystallization process of hydrates during the long-term curing
2. Role of the deflocculant
3. Influence of curing temperature on the crystallization of stratlingite
4. Carbonization of the stratlingite

Acknowledgements

The author wishes to express his sincerest gratitude to the late Professor Ryuji Kitagawa of the Hiroshima University for his great support to this work during its initial stage, and for his invaluable advice and encouragement. He also wishes to express deep gratitude to Assistant Professor Makio Ohkawa of the same University for his constant and invaluable advice rendered during the course of the present work as well as for his critical reading of the manuscript and his encouragement. The author sincerely acknowledges constant and invaluable advice of Professor Hiroshi Hidaka of the Hiroshima University, now Nagoya University rendered during the course of the work as well as for his critical reading of the manuscript. Professor Junichi Ando and associate Professor Kaushik Das of the same University helped in final formulation of this manuscript. The author is also indebted to Professors Toshimori Sekine, Naoki Suda and Ikuo Katayama of the same University for their guidance and advice. He also gratefully acknowledges his debt to Associate Professors Kenichi Hoshino, Masaaki Miyahara, Yasutaka Hayasaka, Tomoko Sato, and to Assistant Professors Tomoeki Nakakuki and Fumito Shiraishi of the same University. This work would not be completed without the kind help of Mr. Yasuhiro Shibata and Dr. Makoto Maeda of the same University during the chemical analysis and textural observations by EPMA and FE-SEM/EDX, respectively. He also is indebted to Associate Professor Mayumi Jige of the Osaka Otani University for her help in the DTA analysis.

The author wishes to express his sincerest gratitude to former Professor Makoto Watanabe for his constant and invaluable advice rendered during the course of the work as well as for his critical reading of the manuscript. He would

like to thank Professor Etsurou Sakai of the Tokyo Institute of Technology for his invaluable advice. Thanks are also due to Dr. Minoru Morioka of Denki Kagaku Kogyo Kabushiki Kaisha for helpful advice. He also gratefully acknowledges Dr. Adriana Borovsky Paulovic, Dr. Christoph Wöhrmeyer, Mr. Makoto Iiyama and Mr. Chris Parr of Kerneos for their helpful advice and encouragement. This study had been supported by research grants from Kerneos. The author wishes to express his gratitude from the heart to his wife for her constant encouragement and financial help.

Chapter II

Experimental

II. 1 Grouping of experimental materials

Two different types of raw materials, namely group A and B were used in this study, and the experimental methods were slightly different among these two groups. The experiments on A-Group were carried out prior to the experiments on B-group. Therefore, a number of improvements have been added to the experiments on B-group. The chronological observations of samples including the effects of carbonation were done only on the B-group samples.

Moreover, it is to be noted that the presently studied CAC has a compositional characteristic. CAC used in Japan generally contains more than 40 mass percent of alumina component. Since, the materials used in this study contained more than 70 mass percent of alumina component, these were highly enriched variety among CAC. Therefore, the materials are called high alumina cement (HAC) in the following text.

II. 2 Materials

II. 2.1 Materials of A-group

The raw materials of the A-group were a high-alumina cement made by Denki Kagaku Kogyo KK, labelled “HACd”, and a silica fume, which is sold under a trade name of micro-silica 940-u made by Elkem, labelled “SF4”. These two materials are commercially available. The chemical compositions of these materials in the manufacturer’s material specification are shown in Table 3. The X-ray diffraction (XRD) analysis of HACd clarifies that the constituent crystal phases are mainly CA ($CaO \cdot Al_2O_3$), Al_2O_3 (corundum) and a trace of CA_2

($CaO \cdot 2Al_2O_3$). The SF4 is a grayish and amorphous silica, whose grains are less than 1 μm in diameter, as stated in the manufacturer's material specification. The compounding ratio (mass ratio) between HACd and SF4 was determined as 3 : 2 in reference to the general combination ratio of LCC. The cement paste was obtained by mixing above-mentioned solids and water in the following prescribed ratios. Those raw materials were well-mixed, and then the deionized water in 50 mass percent was added to the mixture for kneading for 3 min. The molar ratio of CaO, Al_2O_3, SiO_2 and H_2O of the mixture was 2.00 : 3.16 : 4.52 : 40.06. The molar ratio showed a considerable excess of SiO_2 and Al_2O_3 compared to the theoretical ratio (2 : 1 : 1 : 8) of chemical composition of stratlingite. The kneaded mixture was stored in a hermetically sealed glass bottle with 20 mm of inner diameter and 40 mm in height using a plastic lid to cure at 23 °C for 22 days. This whole assembly was kept in a beaker filled with water. The cured matter was taken out from the vessel and crushed under acetone solution in order to stop any further hydration, following Edmonds and Majumdar's method (Edmonds and Majumdar, 1989). Then, the crushed samples were air-dried.

II. 2.2 Materials of B-group

The raw materials of the B-group were high-alumina cement (Secar 71) made by Kerneos, labelled "HACk", silica fume (Elkem 971-U) made by Elkem, labelled "SF7", and reagent-grade sodium tripolyphosphate (TPP). The former two materials are commercially available. The chemical compositions of the raw materials as provided by the manufacturers are presented in Table 3. The XRD analysis of HACk clarifies that the main crystal phases are CA and CA_2. The

grayish silica fume has on average particle size less than 1 μm, as stated in the manufacturer's material specification.

The above solids were mixed with water to form two different types of cement pastes. Two type of pastes were prepared to understand the role of the deflocculant by mixing the required amount of solids and deionized or distilled water at a water/solid ratio of 0.864/1 for 3 min. One cement paste consisted of 60 mass percent of HACk, 40 mass percent of SF7 and the water, while the other paste had an additional 0.41 mass percent of TPP in the former one.

Two kinds of experimental techniques were employed for the materials of B-group. The first one was that the mixed cement pastes were put into small glass bottles (φ 20 × h 40 mm), and were immediately sealed with a plastic lid. This is a conventional technique used by most of the earlier researchers. The second one where the mixed cement pastes were placed onto the glass slides were also sealed in the plastic bags together with a water-soaked cotton sheet just after mixing the starting materials. This latter technique was tried newly in the present study in order to observe the surface microstructure.

These two kind of starting samples were placed in the thermostatic oven under 10 ± 2, 21 ± 2, 30 ± 1, 35 ± 1, 50 ± 1 and 60 ±1 °C conditions. The temperatures of the sample were monitored using a thermocouple, whose hot junction was set in the vicinity of the samples. It is noteworthy that the extra heating of the sample by heat of reaction could not been controlled. The relative humidity in the sealed bag was probably kept between 95 to 100 % for the glass slide samples. However, water was added in the cotton sheet several times to avoid drying of the high-temperature samples during the long-term curing experiments.

After the production of heat of reaction was confirmed, hardening times of the products were determined by pressing a fingernail onto the surface of the samples, and were cross-checked with the X-ray data to confirm the initiation of crystallization.

The all bottle samples were split into several fragments of about 0.5 - 1.5 cm^3 volumes after 2 days of curing. These fragments were reinserted into a new glass bottle (φ 20 × h 40 mm) together with a water-soaked cotton ball, and sealed with a plastic lid. This process was done to make sample collection easier in the subsequent stages of experiments, at the same time to facilitate the release of heat of reaction quickly from the sample, and also to maintain the water vapor saturated condition surrounding the fragments. The re-bottled samples were cured for the desired length of time under the same temperature conditions as before, i.e. 10 ± 2, 21 ± 2, 30 ± 1, 35 ± 1, 50 ± 1 and 60 ± 1 °C. The small amount of chip was taken from the sample stored in a bottle every day in order to analyze. The chip was washed in acetone to stop the hydration just after the cutting, and then air-dried. The plate sample was taken out from the plastic bag after the desired time, and then was analyzed by XRD. Since the plate samples did not include a reference material for XRD, a separate standard plate sample was prepared by adding Al_2O_3 of 10 mass percent reagent into the cement paste.

Both the bottle and plate samples, whose curing times were 92 days at 10 °C and 60 °C, 27 days at 21 °C and 35 °C, 300 days at 30 °C and 50 °C, respectively, were analyzed by electron probe microanalyzer (EPMA).

These group B reaction samples were labeled as hf and hft, in which h, f and t stand for high alumina cement, SF and TPP, respectively. The samples marked with b for bottle sample and p for plate sample and numbers 10, 21, 30, 35, 50

and 60 referred to the respective curing temperature. For example, hft-10b stands for bottle sample with high alumina cement with silica fume and TPP at 10 °C.

II. 3 XRD analyses

The small piece of A-group sample was pulverized to make the powder specimen for XRD analysis. The XRD apparatus is MAC Science, M18XHF using CuKα radiation (0.15418 nm) emitted by 40 kV and 100 mA conditions.

The B-group samples were analyzed with RIGAKU MultiFlex X-ray diffractometer using CuKα (0.15418 nm) emitted by 40 kV and 40 mA conditions. The fragment samples of c.a. 0.3 g were taken with a spatula from the bottles, and then they were ground to the fine powder of less than 63 μm in size under acetone to stop the progression in hydration. The previous research reported that the XRD peak intensity for minerals like gibbsite [$Al(OH)_3$] was considerably reduced due to overgrinding of the run product powder (Tsuchida and Ichikawa, 1989), though they were produced by the experiments. Keeping in mind this fact, extreme caution was taken while grinding the run product as minerals like gibbsite was expected in the present series of experiments. The diffraction peaks of a special grade of reagent of Al_2O_3 was used as the reference material to evaluate the intensity and to obtain the d-spacing of the samples. The Al_2O_3 reagent of 10 mass percent was mixed into the grounded samples.

The plate samples were taken out from the plastic bag, and then were set directly on the diffractometer. The relative peak intensity of the plate samples were estimated by comparison with the diffraction peak intensities of Al_2O_3 of the standard plate sample.

The XRD analyses were carried out in the following time schedule: every 10 to 20 minutes between the first 2 - 10.75 hours after mixing; daily in the first week; weekly during the following five weeks; and at least once after nearly 454 days (a few after 1,288 days) in the final period.

II.4 TG - DTA analyses

TG - DTA analyses were done on the reacted products cured after 22 days at 23 ± 0.5 ºC in the A-group samples. Some of the experimental products include significant amount of bigger crystals with nearly 5 mm in size. These crystals were selectively picked up and were ground to the fine powder of less than 63 μm, and then the powders of 15 mg was batched off. Differential thermal analysis and gravimetric analysis were carried out by heating at a rate of 10ºC/min using thermal analysis equipment (RIGAKU TG8120).

II.5 EPMA analyses

The chemical compositions of the reacted products were measured by using the EPMA (JEOL JXA-8200) with an accelerating voltage of 15 kV, a beam current of 5 nA, and beam diameter of 3 μm. Back-scattered electron (BSE) imaging was also done on the same area of chemical measurement. The measured components were as follows: SiO_2, CaO, Fe_2O_3, Al_2O_3, P_2O_5, Na_2O, K_2O, MgO and TiO_2. The remaining values from 100 weight percentage in the results was assigned as H_2O or CO_2 components.

EPMA analyses were done on the reacted products cured after 22 days for A-group of samples. The chunk of specimen was embedded into resin and mirror-polished using the diamond paste (DP) Lubricant Blue solution with

ethanol as the main component (Marumoto Struers KK). The polished samples were coated with vapor-deposited carbon for the EPMA analysis. Elemental mapping of Ca, Al and Si was carried with 5 kV, a beam current of 5 nA.

The bottle samples of about 5 - 8 mm in size of B-group were embedded in a resin at vacuum environment, and then mirror-polished. In order to prevent further hydration of the samples, a liquid lubricant DP-Lubricant Blue (Struers Corp.) was used for the polishing agent. The surfaces of the polished samples were coated with a vapor-deposited carbon for the chemical composition analysis and BSE imaging using the EPMA.

II. 6 FE-SEM analyses

The microstructures of the polished specimen were observed using field-emission gun scanning electron microscope (FE - SEM), Hitachi S-5200 with an accelerating voltage of 20kV, emission current of 1000 - 9500 nA, installed at N-BARD, Hiroshima University.

Chapter III

Results

III.1 Results of hardening time

The hardening times of the B-group samples are shown in Table 4. Generally, the hardening time became shorter with the increase of curing temperature (Fig. 2). The hardening time of the bottle samples cured at 10 °C was short same as that at 30 °C samples. While, hardening time of the hf-plate sample cured at 10 °C was extremely long (Fig. 2).

III.2 Results of XRD analyses

III.2.1 Results of XRD analyses of the A-group

Results of XRD analyses of the A-group samples are shown in figure 3. The detected hydrates were stratlingite (C_2ASH_8), CAH_{10} and gibbsite (AH_3). Corundum (Al_2O_3) was also present. Both CA and CA_2, the major constituents of HACd were not found. The peaks of stratlingite correspond to the d-values of 1.25, 0.625, 0.417, 0.342, 0.2875, 0.2800, 0.2612, 0.2485, 0.2408, 0.2365, 0.2113, 0.2015, 0.1884, 0.1823 and 0.1795 nm. The lattice parameters obtained from these values are: a = 0.5743(3) nm and c =3.753(5) nm. All of the detected peaks correspond to the above mentioned minerals.

III.2.2 Results of XRD analyses of the B-group

Results of XRD analyses of the B-group are shown in figures 4 to 27. In this group, the result for each of the constituent minerals will be described in the following section according to the general order of appearance from low to high temperature experiments.

(1) CAH_{10}

CAH_{10} hydrate only crystallized at the curing temperature of 21 °C or less, and did not crystallize at higher temperature. CAH_{10} crystallized in all samples except hf-10p on the first day at 10 °C (Figs. 4 to 5, 16 to 17 and 28). This hydrate crystallized in hf-b on the first day at 21 °C (Figs. 7 and 28), while in hft-b, crystallization occurred after one day (Figs. 6 and 28).

The results of the long term curing at 10 °C are shown in figures 4 and 5. The peak intensity of CAH_{10} hydrate in hft-10b increased until it reached a constant value after 3 weeks (Fig. 4). On the other hand, the peak intensity of CAH_{10} hydrate in hf-10b reached the maximum intensity after 5 days, and then the intensity decreased gradually until it reached a plateau after 4 weeks (Fig. 5). The peak intensity of CAH_{10} hydrate in hft-21b increased until it reached a constant value after 12 days, and from 28 days the peak intensity decreased until it reached a constant value after 94 days (Fig. 6). The peak intensity of CAH_{10} hydrate in hf-21b increased until it reached a constant value after 4 days, and from 21 days the peak intensity decreased until it reached a constant value after 28 days (Fig. 7). The XRD peak intensities of the CAH_{10} hydrates of all the bottle samples are shown in figure 29. The XRD peak intensities of CAH_{10} in the sample with TPP increased gradually, while those without TPP increased rapidly.

(2) C_2AH_8

The initiation of crystallization of C_2AH_8 hydrates are confirmed by XRD in the early stage of hardening (Table 5, Fig. 30), except in hf-10b and hf-10p

samples. Crystallization of C_2AH_8 hydrate in hft-10b occurred in a day (Table 5, Fig. 30). The time required for crystallization of C_2AH_8 hydrates became shorter with the increase in the curing temperature except hft-21p (Fig. 30).

The results of the long term curing of C_2AH_8 are shown in figures 4, 5 to 16, 18 to 27 and 31 to 32. The time required to reach the maximum X-ray peak intensity of the bottle samples with TPP was shorter as the curing temperature increased (Table 6, Fig. 33). Further, after the intensity reached the maximum, it continued to decrease and eventually disappeared (Figs. 4, 6 to 16 and 18 to 27). In the samples without TPP, likewise, the intensities showed the same tendency. Especially, C_2AH_8 in hf-60 and hf-50 crystallized immediately showing high XRD peak intensity, and then disappeared rapidly (Fig. 32).

The times required to reach the maximum XRD peak intensity of C_2AH_8 hydrates are shown in figure 33. Hft-bottle sample especially had shown tendency that, at low curing temperature, the time to reach the maximum intensity increased significantly. Other samples except those for 50 ºC and 60 ºC required 2 - 3 days to reach the maximum intensity, while 50 ºC and 60 ºC samples except hft-50b reached the maximum in 3 - 3.5 hours.

The maximum XRD intensities of the C_2AH_8 hydrates are shown in figure 34 and table 7, and are shown the low data than that of CAH_{10} hydrates (Fig. 35). C_2AH_8 hydrates were abundant at 30 - 35 ºC in the bottle samples, while in the plate samples the hydrates were abundant at higher temperature than the bottle samples. The plate sample with TPP at 60 ºC had the highest intensity, while the bottle sample with TPP had low value, almost the same as that of 10 ºC.

(3) C_4AH_{13} and C_4AcH_{11}

C_4AH_{13} and C_4AcH_{11} (c = CO_2) were detected in all plate samples from early stage of hardening (Figs. 16 to 27). C_4AH_{13} hydrate in the bottle samples was detected for a short period of time in hft-21b, which completely disappeared after 1 day (Fig. 6). C_4AH_{13} in hft-30b was detected only once after 2 days with low intensity and did not appear again (Fig. 8). C_4AcH_{11} was detected in hf-30b after 2 days with low intensity (Fig. 9), and was continued to detect up to 8 days. It did not appear after 8 days.

(4) C_2ASH_8 (Stratlingite)

Stratlingite was crystallized in the bottle samples at the curing temperature of 21 °C or above, and also at 10 °C only in hft-10b sample. The XRD peak intensities of stratlingite in the samples except hft-10b continued to show a constant value during the rest period of the experiment (Figs. 4 and 6 to 15). The crystallized stratlingite was confirmed only once in 149 days for hft-10b (Table 8, Figs. 36 and 37). Stratlingite did not crystallize in hf-10b during the entire period of experiment.

The times required for crystallization of stratlingite are shown in table 8 and figure 36. In hft-60b, the earliest crystallization occurred after 2 hour 20 minutes. The times required to reach the maximum XRD peak intensity of stratlingite are shown in table 9 and figure 37.

The maximum XRD peak intensities of stratlingite are shown in table 10 and figure 38. The highest intensity was observed in hft-60p, followed by that in the hft-30b and hft-50b. The low intensity was observed in the hf-50b. Crystallized stratlingite in the bottle samples showed the same XRD peak intensity all along (Figs. 6 to15 and 39 to 42).

(5) $Al(OH)_3$ (Gibbsite and Bayerite)

Gibbsite ($Al(OH)_3$) was crystallized in all the samples. The crystallization of gibbsite was markedly delayed in the samples without TPP at 10 ˚C (Table 11, Fig. 43). The crystallization was observed after 759 days in hf-10p (Fig. 17)

Bayerite ($Al(OH)_3$) was crystallized in the plate samples mostly after long period of curing (Figs. 16, 18 to 21, and 25). The XRD peak intensity of bayerite increased rapidly in hft-21p and hf-50p (Figs. 18 and 25).

(6) C_3AH_6 (Hydrogarnet)

C_3AH_6 hydrate (hydrogarnet) did not crystallize in the samples cured at ≤ 21 °C (Figs. 4 to 7 and 16 to 19). The crystallization of C_3AH_6 in the samples with TPP was delayed compared to the sample without TPP. For example, C_3AH_6 was detected after 9 days in hf-35b (Fig. 11), while the crystallization occurred only after 5 weeks in hft-35 (Fig. 10).

C_3AH_6 hydrates crystallized earlier than stratlingite (Fig. 13).

(7) $CaCO_3$ (Calcite)

Calcite ($CaCO_3$) was identified regardless of the TPP present in the bottle samples at 30 °C, 35 °C and 50 °C after long time of curing.

Calcite was identified in all plate samples. Moreover, the samples with TPP rapidly crystallized calcite than those without TPP with the exception of 10 °C experiment (Figs. 16 to 27).

(8) $CaCO_3$ (Vaterite and Aragonite)

Vaterite crystallized after the crystallization of calcite in hft-35b (Fig. 10) and crystallized in all plate samples except hf-21p (Fig. 16 to18 and 20 to 27).

Aragonite crystallized in hft-35b after the crystallization of calcite (Fig. 10), while aragonite disappeared in a very short period of time after crystallization in the plate samples, hf-30p, hft-50p and hf-50p (Fig. 21, 24 and 25).

III. 3 Results TG - DTA analyses

TG and DTA profiles of the A-group sample are shown in figure 44. The profile show a continuous decrease from the beginning of heating to 100 °C. A clear peak of the endothermic reaction was observed around 230 °C. The TG profile displayed drastic decrease in the vicinity of 230 °C and was compatible with the changes in DTA profile. In the DTA profile, no endothermic peak was observable after this. While, TG line continued to decrease in a low inclination, and after nearly 600 °C the decrease in slope became gentler. The existences of endothermic peaks of gibbsite (AH_3) (223 °C and 301 °C: Kloprogge et al., 2002; Colombo and Violante, 1996) and C_3AH_6 (300 °C: Richardson and Groves, 1990) were difficult to ascertain from the TG - DTA profiles of the studied experimental materials.

III.4 Results of EPMA analyses

BSE images of the A-group samples are shown in figures 45 to 48. The EPMA analysis data of platy structures in BSE image (points S1 to 11) are shown in table 12. Table 13 shows the calculated relative molar ratio normalized to one Al_2O_3. The area containing S12 also displayed a thin platy structure, but there were a number of pores in the radiated region of the electron beam (as in

fig. 45) and therefore the analytical values were of a lower reliability. As shown in figure 45, agglomerates of SiO_2 presumed to be the SF4 of the starting material were observed (S13 and S14). Considerable amount of SiO_2, but with extremely low amount of CaO and Al_2O_3 were observed at the dark-gray area (S13), while the presence of some amount of Al_2O_3 and relatively less CaO were observed at the bright area (S14). Relatively bright areas were often observed outside of SF4 agglomerate, and those contained a relatively high amount of CaO (S3). Platy crystals (S1 and S2) were often observed in the SF4 agglomerate (S13). Moreover, a platy crystal in many cases developed in a radial pattern (S3 and S12) at the fringe of the agglomerate (S14). The black-looking area is pore (P) and the bright granular crystal (A) is Al_2O_3. Figure 46 shows a large radial crystal. The rim of the crystal looked to be relatively massive than the central area of the crystal, and the chemical analysis of the S4 area (Table 12 and 13) yielded the value close to that of C_2ASH_8. However, the chemical analysis of the S5 indicated that the SiO_2 ratio was rather high despite the fact that S5 area was just adjacent to S4 (Table 12 and 13). Figure 47 shows the presence of large crystals similar to those in Figure 46. The chemical analysis of the central area of the crystal (S6) displayed lower CaO ratio (Table 13), compared to other measurement points. Figure 48 shows the presence of platy crystals. The chemical compositions were different at different measurement points (S9 to S11) in the same crystal. Chemical mapping was carried out for the area surrounding the square mark in figure 48 to understand the cause. As a result, it became apparent that distributions of Ca, Al and Si were especially heterogeneous (chemical mapping figure 49).

BSE images of the B-group samples are shown in figures 50 to 70. The

EPMA analysis data of the bottle samples cured at 21 and 35 °C of the B-group samples are shown in the table 14 to 16. The H_2O or CO_2 contents were calculated assuming that all the residues in the mass percent values were H_2O or CO_2 molecules, respectively. Table 17 to 19 show the calculated relative molar ratio normalized to one Al_2O_3, and also show the presumed main phases of each analyzed point. BSE images revealed large masses of SF7 of about 100 – 200 μm in diameter on a rough surface of the bottle samples (Fig. 50). The space between the masses was filled with plate crystals and amorphous mater (Figs. 51 and 52). Furthermore, big crystals of different hydrates were often surrounded by the SF7 masses (Fig. 53). The samples appeared to have heterogeneous texture as shown in figures 50, 55, 59 and 63.

Figures 50 to 54 show BSE images of hft-21b. Well-developed plate-shaped crystals of C_2AH_8 hydrate are shown in figure 51. EPMA analyses of the bright part (P1) in Plate 6c revealed the presence of CAH_{10}, with an irregularly-shaped white area (P2) made up of unhydrated HAC. EPMA analyses of a smooth part (P3) of large bright crystals observed in the center of figure 53 showed that the composition was close to that of the stratlingite ($CaO : Al_2O_3 : SiO_2 : H_2O = 2 : 1 : 1 : 8$). While, the composition of the rough part (P4) yielded slightly lower molar ratio of CaO and a higher molar ratio of SiO_2 than the theoretical value of stratlingite (Table 14 and 17). Figure 54 shows the bulk mass of agglomerates of SF. At the center of figure 54, semi-circular bright crystals are present. The massive crystals can be distinctly observed inside the agglomerates of SF at the bottom left corner of this photomicrograph. The analysis data of P5 also confirmed a slightly lower molar ratio of CaO and higher SiO_2 (Table 17) than the theoretical value of stratlingite. The well-developed plate-like crystals are

visible in the BSE images of hft-35 (Figs. 56 and 57). The analysis data of P6 in figure 56 indicated that the crystal was C_2AH_8, while those of P7 and P8 suggested that some SiO_2 was likely to be adhered to the C_2AH_8 crystals (Table 14 and 17). Based on the area calculations, the bright area (P9) in the BSE image (Fig. 57) corresponded to CAH_{10} (Table 14 and 17). However, XRD analysis did not detect any CAH_{10}. Round–shaped crystals were observed at the edge of the large mass of SF agglomerate of about 100 μm in diameter (Fig. 58). The compositions of the crystals in P10, P11 and P12 indicated that these crystals might have slightly lower molar ratio of CaO, and higher molar ratio of SiO_2 than the theoretical value of stratlingite. BSE images of hf-21 (Figs. 59 to 62) show large hydrate crystals of 50 μm in diameter or more surrounding the larger chunks of SF. The compositions of the crystals in P13 to P18 and P24 (Table 14 and 17) indicated slightly lower molar ratio of CaO and much higher molar ratio of SiO_2 than the theoretical value of stratlingite. Analyses of the crystals in P21 to 23 showed that these crystals have higher molar ratio of SiO_2 than the theoretical value of CAH_{10} hydrate (Figs. 61 and 62, Tables 14 and 17). The compositions of the P19 and P20 showed that the SF mass was contaminated with a massive substance composed of SiO_2 (Fig. 60, Table 14) and fine grains of alumina (Fig. 61, Table 14).

The BSE images of hf-35 (Figs. 63 to 65) reveal that the quite large crystals inside and at the edge of SF masses (Figs. 63 to 65). The compositions of these crystals in P25, P26, P28 and P29 (Fig. 64) showed the lower molar ratio of CaO and higher molar ratio of SiO_2 than the theoretical value of stratlingite. In figure 65 smooth parts (P31 and P33) of the large crystals exhibited the composition which was close to stratlingite, while rough parts P30, P34 had a lower molar

ratio of CaO and a higher molar ratio of SiO_2 than the theoretical value of stratlingite (Table 14 and 17). Big chunks were confirmed to be composed of SF in P27 (Fig.64) and in P32 (Fig.65). In figure 66, plenty of small bright grains are seen in the matrix. Although the XRD analysis did not confirm the presence of hydrogarnet (C_3AH_6), the composition of the crystal corresponded to C_3AH_6 with some additional SiO_2 (Table14 and 17).

BSE images of 21 – 35 °C curing plate samples are shown in figures 67 to 70. Large crystals of more than 50 μm in size are clearly visible in figures 67 and 68. In the hf samples, on the other hand, the well-developed plate crystals can be observed (Figs. 69 and 70). Interestingly, the spherical crystals of vaterite were not found in any plate samples (Figs. 67 to 70) although the vaterite was detected from XRD data.

Figure 67 is an image of hft-21p. EPMA analyses of the bright crystals in P76, P77, P80, P81 and P82 indicated that the crystals had 51.6 to 56.9 mass percent of CaO. XRD analyses of these large crystals showed the strong peaks of calcite ($CaCO_3$), and no peaks of other components. The analyses of the points P78 and P79 yielded 52.35 to 53.90 mass percent of CaO and 1.30 to 4.99% of Al_2O_3. The composition of P83 indicated that the crystal was CAH_{10} (Table 16 and 19).

Figure 68 is an image of hft-35p. The plate-like crystals are radially-covered with CaO. EPMA analysis data showed that the concentration of SiO_2 and Al_2O_3 were observed in P101 (Table 16). SiO_2 was not detected in P102 (Table 16) and alumina gel or gibbsite was found to be contaminated with about 17.61 mass percent of CaO. Although the data of agglomerates of SF of about 200 μm in diameter indicated the CaO and SiO_2 molar ratio of 1:1, the XRD measurements

did not confirm the presence of any hydrate. The data of the P103, P105 and P106 suggested that the crystal was $CaCO_3$ (Table 15 and 18). $CaCO_3$ contained 2.96 mass percent of Al_2O_3 at P104 (Table15 and 18).

Figure 69 is an image of hf-21p. It suggested that SF, gibbsite or alumina gel covered the substrate in P74 (Table16 and 19). A number of small crystals with the chemical composition of $CaCO_3$ were found in P69 and P73 (Table 15 and 18). This result was identical with the result by XRD analysis in which intense peaks of calcite and vaterite were detected. The composition of large crystals of more than 30 μm in size in P71 and P72 confirmed these crystals as calcite (Table 15 and 18). P70 did not contain any CaO and only consisted of SiO_2 and Al_2O_3 (Table16 and 19). Although the mineral name could not be identified, well-developed foil-like minerals were found in substrate holes.

Figure 70 is an image of hf-35p. The surface consisted of SF and gibbsite or alumina gel (P54). A number of large crystals were observed in P46, P47 and P55, and their composition were $CaCO_3$ (Table 15 and 18). These results were supported by the intense peak of calcite detected from XRD data. The exact mineralogical name of the well-developed foil-like body found in substrate holes was not identified.

III.5 Results of FE-SEM analyses

The FE-SEM observation at 30,000 magnifications was carried out for a cross-sectional surface of the crystal on the A-group sample. The analyzed areas were that of a homogeneous single crystal and neither fine structures nor inclusions were observed.

The cross-sectional surface of C_2ASH_8 crystals with a high SiO_2 molar ratio

was observed by FE-SEM on the B-group sample and is shown in Figures 71 to 73. The FE-SEM image of the area near P36 showed the presence of irregular-shaped grains of about 0.5 μm in size clearly attached to the surface of C_2ASH_8 crystal (Fig. 72). They were found to be composed of SF. These grains of SF can increase SiO_2 molar ratio of the surface (Fig. 74), and such a possibility of these structures cannot be denied. Figure 73 shows the irregularshaped particles of less than 0.5μm in size, which formed the chunk of SF as shown in Figure 63. Elemental analyses by energy-dispersive spectroscope (EDX) of P37 detected mostly Si and some Al with some residual quantity of Ca (Fig. 75). Figure 76 shows the smooth matrix of plate-like crystal which is present in the upper side of Figure 64. Any adhesion/attachment of SF particles was not recognized on the surface at 300,000 magnifications (Figs. 77). The EDX elemental analyses of P38 (Figs. 76 and 77) indicated molar ratios of main components close to C_2ASH_8 (Fig. 78). However, the flat side of the polished surface was too small to carry out any detailed observation.

Chapter IV

Discussion

IV.1 Hardening time and its variation

Bushnell-Watson and Sharp (1986, 1990a, 1990b) showed that an anomalous retardation occurred at 28 - 30 ˚C on the neat cement paste made of calcium aluminate cement with water. They concluded that CAH_{10}, which acted as nucleus for the crystal growth in HAC - H_2O system, required considerable amount of crystallization time at 28 - 30 ˚C. In the present study, although the measurement method is not precise, slight retardations are recognized at 21 and 35 ˚C (Fig. 2). Unlike Bushnell-Watson and Sharp (1986, 1990a, 1990b) this study is carried out with the addition of SF and TPP. Since almost no difference is observed in the presence or absence of the TPP (Fig. 2), the addition of SF might have a causal influence on the retardation phenomenon.

IV.2. Experimental products and their formation processes based on the results of XRD analyses

IV.2.1 A-group

It is evident from the figure 3 that both CA and CA_2 were impossible to detect in the experimental run product of HACd. This fact indicates that complete hydration and consumption were executed until 22 days. Corundum (Al_2O_3) was also included in the starting material, and remained without hydration. Gibbsite (AH_3) crystallized by the hydration of CA and/or CA2 following the equations 1 and 2 below,

$$2CA + 11H \rightarrow C_2AH_8 + AH_3 \qquad (1)\ \text{Parr et al. (2005)}$$

$2CA_2 + 17H \rightarrow C_2AH_8 + 3AH_3$ (2) Klaus et al. (2013)

C : CaO, A : Al_2O_3, H : H_2O

C_2AH_8 was not detected by the XRD analysis. Bentsen et al. (1990) described that C_2AH_8 transferred to stratlingite (C_2ASH_8) (eqn. 3). On the other hand, Hirose and Yamazaki (1991) did not observe other hydrates than CAH_{10} in the early period of hydration, and indicated that the peak intensity of CAH_{10} decreased gradually, while the peak intensity of stratlingite increased gradually in their specimen at 20 °C. They proposed a possibility that CAH_{10} transferred to stratlingite (eqn. 4). Mostafa et al. (2012) also described that CAH_{10} transferred to stratlingite based on their experiments, in which a sodium sulfate was added to CAC + SF as an activator. It is also known that CAH_{10} transfers to C_2AH_8 (Parr et al., 2005, eqn. 5). In the present study, however, C_2AH_8 was not observed in the sample cured after 22 days, and there was no evidence whether C_2AH_8 transferred to stratlingite.

$C_2AH_8 + S \rightarrow C_2ASH_8$ (3) Bentsen et al. (1990)

$2CAH_{10} + S \rightarrow C_2ASH_8 + AH_3 + 9H$ (4) Mostafa et al. (2012)

$2CAH_{10} \rightarrow C_2AH_8 + AH_3 + 9H$ (5) Parr et al. (2005)

IV.2.2 B-group

For this group of experiments, the results for each of the constituent minerals will be discussed in the following sections in accordance to the order of crystallization from low to high temperature experiments.

(1) CAH_{10}

Parr et al. (2005) indicated the dominance of the formation of CAH_{10} below 10 °C and this continued up to around 27 °C.

$$CA + 10H \rightarrow CAH_{10} \qquad (6)\ \text{Parr et al. (2005)}$$

The result of the present study (Fig. 4 to 7) shows almost the same trend as Parr et al. (2005). Addition of TPP promoted the retardation on the crystallization of CAH_{10}. According to Maeda et al. (2007), Ca ion from alumina cement firstly reacted with tripolyphosphoric acid ion of TPP to form calcium phosphate ($Ca_5(P_3O_{10})$). After phosphoric acid were consumed, then crystallization of CAH_{10} started. Although it is well known that CAH_{10} gradually transforms to C_2AH_8 (e.g. Parr et al., 2005), the result of the present study implies that the transformation does not occur at 21 °C. This is evident as the X-ray intensity of C_2AH_8 continues to keep constant even after 450 days at this temperature.

(2) C_2AH_8

The early crystallization of C_2AH_8 implies that it was formed from CA and/or CA_2 (via eqn. 1 and/or 2). The transformation from CAH_{10} to C_2AH_8 seems unlikely to occur in the present set of experiments, because it takes a long time even at a suitable temperature (Parr et al., 2005). TPP contributes to the crystallization of C_2AH_8 based on the comparison of hft-10b with hf-10b (Table 5, Fig. 30). The crystallization time and disappearance time of C_2AH_8 became faster as the curing temperature increased. It can be suggested that the carbonation reaction of C_2AH_8 (eqn. 7) is strongly enhanced at high

temperatures about 50 to 60 ºC.

$C_2AH_8 + 2CO_2 \rightarrow 2Cc + AH_3 + 8H$ (7)

c : CO_2, Cc : $CaCO_3$

(3) C_4AH_{13} and C_4AcH_{11}

It is well known that C_4AH_{13} and C_4AcH_{11} are unstable minerals and transform to other minerals in a short period of time (Rojas and Rojas, 2005 and references therein). Matschei et al. (2007) described that C_4AH_x was not only metastable but also labile. In the present experiments, C_4AH_{13} altered to C_4AcH_{11} in a few days after appearance (Figs. 16 to 27). The higher the curing temperature, the faster this transition occurs, and eventually C_4AcH_{11} disappears after a few weeks (Figs. 16 to 27).

Fierens et al. (1974) and Bentsen et al. (1990) described C_4AH_{13} as a transient hydrate for C_4AcH_{11} and C_3AH_6 hydrates. Rojas and Rojas (2003) and Rojas (2006) described stratlingite and C_4AH_{13} phases as not stable and could be transformed to hydrogarnet (C_3AH_6) after long period of time. Since C_3AH_6 as an expected end product of chemical equation (8) was not detected, C_4AH_{13} and/or C_4AcH_{11} (Figs. 16 to 27 except 22) might have been transferred to calcite as shown via chemical equations (9) and (10).

$C_4AcH_{11} \rightarrow C_3AH_6 + CaCO_3 + 5H$ (8) Fentiman (1985)

$C_4AH_{13} + CO_2 \rightarrow C_4AcH_{11} + 2H$ (9) Fischer and Kuzel (1982)

$C_4AcH_{11} + 3CO_2 \rightarrow 4CaCO_3 + AH_3 + 8H$ (10)

C_4AH_{13} and C_4AcH_{11} are dominant in almost all of the plate samples. This fact indicates that those hydrates are easy to be formed on the surface of the cement paste.

(4) C_2ASH_8 (Stratlingite)

There are two possibilities about the transformation process of stratlingite. One is through the equation 3 mentioned above (Bentsen et al., 1990), and the other is through the equation 4 (Mostafa et al., 2012, and also Hirose and Yamazaki, 1991). In the present study, XRD intensities of C_2AH_8 varied inversely to that of stratlingites (Figs. 6 to 15, 41 and 42). It can be concluded that C_2AH_8 hydrate transformed to stratlingite (eqn. 4). Stratlingite crystallized rapidly in the samples with TPP cured at high temperature (Tables 8 and 9, Figs. 36 and 37). The addition of TPP promoted to crystallize stratlingite because its sodium ions have a significant influence on stratlingite formation (Ding et al. 1995). In the plate samples, those relationship is unclear. This fact possibly indicates that stratlingite forms in the interior of the cement paste rather than on the surface.

Crystallized stratlingite in the bottle samples kept the same XRD intensity throughout the rest of the period of experiments (Figs. 6 to15, 39 and 40). The fact indicates that they have not been exposed to conditions in which alteration occurs. If stratlingite is exposed to high temperature, humidity and atmospheric CO_2, it might transform to calcite, vaterite or aragonite following the equation 11. These transferred minerals are present in the plate samples (Figs. 21 to 27).

$$C_2ASH_8 + 2CO_2 \rightarrow 2CaCO_3 + AH_3 + SiO_2 + 5H_2O \qquad (11)$$

The CA and CA_2 phases (Figs. 12 to 15) disappeared more rapidly at higher curing temperatures, while their dissolution was delayed at lower curing temperatures (Figs. 4 to 7). The addition of TPP accelerated the stratlingite formation even at lower temperatures, and seemed to promote the delay of the dissolution of CA and CA_2 phases. Ding et al. (1996a) reported that the dissolution of CA in HAC was obviously delayed as sodium silicate was added. It would be reasonable to think that the sodium ions in TPP gave the same effect as that of sodium silicate.

(5) $Al(OH)_3$ (Gibbsite and Bayerite)

The marked delay of the crystallization of gibbsite ($Al(OH)_3$) in the samples without TPP indicates that the TPP promoted the crystallization of gibbsite (Table 11, Fig. 43).

Bayerite ($Al(OH)_3$) was crystallized in the plate samples, while in the bottle samples this hydrate could not be confirmed. This phenomenon is likely to be associated with carbonation, but further study is needed to clearly understand this.

(6) C_3AH_6 (Hydrogarnet)

TPP retarded the crystallization of C_3AH_6 hydrate (hydrogarnet), while high temperature accelerated its crystallization (Figs. 12 to 15). In several plate samples, the crystallization of C_3AH_6 was not detected (Figs. 20 and 22). C_3AH_6 is known among researchers as an extremely stable hydrate that becomes stable over a long period of time (Gosselin et al., 2010; Calvo et al., 2013; Kira et al.,

2013; Reig et al., 2016). If crystallized C_3AH_6 is kept in hot and humid atmosphere with high concentration of CO_2, it is transferred to calcite, vaterite or aragonite as shown in the following equation 12.

$$C_3AH_6 + 3CO_2 \rightarrow 3CaCO_3 + AH_3 + 3H \qquad (12)$$ Goñi and Guerrero (2003)

This transformation might have occurred in some plate samples (Figs. 23 and 25 to 27)

(7) $CaCO_3$ (Calcite)

Calcite ($CaCO_3$) is considered as one of the most stable minerals. Calcite was identified in all plate samples, which were always in contact with the atmosphere. Calcite was generated by a reaction of atmospheric CO_2 with Ca ion from CAH_{10}, C_2AH_8, C_4AH_{13}, C_4AcH_{11}, C_2ASH_8, and C_3AH_6, and the TPP promote the crystallization of calcite. During the growth of calcite, Ca ion from these hydrates was consumed and eventually disappeared. Calcite was also identified in the bottle samples after long time of curing, although the bottles were sealed with plastic lids. This is possibly a consequence of atmospheric CO_2 that had entered into the bottle during every sampling.

(8) $CaCO_3$ (Vaterite and Aragonite)

Vaterite and aragonite were together observed at 35 ºC in one specimen of bottle sample (hft-35b). Although the experimental conditions are considerably different from this study, Ogino et al. (1989) showed that the formation of three polymorphs (calcite, vaterite and aragonite) was observed at 40 to 50 ºC. Hence,

the coexistence of the two minerals in the present experimental study does not seem unusual.

The result of the plate samples showed that vaterite finally disappeared at temperatures below 30 ºC. This result is consistent with Ogino et al. (1989), implying that calcite is stable than vaterite at low temperature.

IV. 3 Thermal responses of the reactions from TG - DTA analyses

Consecutive decrease in DTA line and TG line from the beginning of heating to 100 °C, as shown in figure 44, are attributable to the evaporation of free water, and the dehydration and/or the pyrolysis of CAH_{10}, AH_3, and AH_3 gel (Heikal et al., 2004; Kosmac et al., 1993). According to Singh et al. (1999), the peak of the endothermic reaction of stratlingite (C_2ASH_8) can be observed at the temperature between 180 °C and 220 °C. However, the obtained value in this research was around 230 °C and deviated from the so far known value of stratlingite. The endothermic peak occurred when AH_3 gel transferred to gibbsite (γ-AH_3) at 225 °C for samples cured at 40 °C, and at 235 °C for samples cured at 60°C (Heikal et al., 2004). Therefore, it may cause the presumable peak overlapping of the endothermic reaction of stratlingite and the transition of AH_3 gel to gibbsite. It is to be noted that the gibbsite was already crystalized in the sample as determined by XRD analyses. In that case, a certain amount of unreacted AH_3 gel had remained in the sample.

The TG line displays a sudden decrease in the vicinity of 230 °C and is compatible with the changes in DTA line. In the endothermic DTA curve, there is no observable peak after this temperature, while TG line continued to decrease slowly. This decrease in slope of the TG line becomes gentler over temperature

around 640 °C. The existences of AH_3 (gibbsite, having endothermic peak at 223 °C and 301 °C (Kloprogge et al., 2002; Colombo and Violante, 1996)) and C_3AH_6 (having an endothermic peak at 300 °C (Richardson and Groves, 1990) are not possible to ascertain from the present TG - DTA line. Non-detection of C_3AH_6 peaks is comparable with the results of the XRD analyses.

IV.4 Chemical characterization from EPMA analyses

In the A-group samples, all of the crystals from analyzed point S1 to S11 displayed a platy structure in the BSE image on the mirror-polished surface of the sample (Figs. 45 to 48). It was considered at first that these crystalline hydrates might be stratlingite (C_2ASH_8), which also showed a strong peak in the XRD analyses (Fig. 3). However, the results of the chemical analysis showed that all of the points except S4 had the lower CaO-content and higher SiO_2-content than the theoretical value of stratlingite ($CaO : Al_2O_3 : SiO_2 : H_2O = 2 : 1 : 1 : 8$) (Table 12). In other words, the chemical composition of these analyzed points was fairly close to the ratio of the starting material.

In the B-group bottle samples, BSE images on the mirror-polished surface of the samples imply that stratlingite crystals occur in close association with agglomerates of SF. With a few exceptions, C_2AH_8 was not observed in the samples (Table 13). This suggests the transformation from C_2AH_8 to stratlingite. The compositions of stratlingite crystals showed that these crystals had lower molar ratio of CaO and higher molar ratio of SiO_2 than the theoretical value of stratlingite (Table 13). This non-stoichiometric composition of stratlingite has been reported by many researchers (Richardson and Groves, 1990; Hirose and Yamazaki, 1991; Lopez et al., 2008; García-Lodeiro et al., 2010). Furthermore,

in the B-group plate samples, since the surface polishing was not performed, the sample surface was covered by a large amount of calcite crystals (Table 14), and therefore details of the structure had become difficult to recognize.

IV.5 Microscopic observations by FE-SEM and chemical variability

Lopez et al. (2008) reported that the molar ratios of the hydrate obtained from EDX analysis did not fit with that of stratlingite (C_2ASH_8). They concluded that the excess of Si was due to the signal from the surrounding unreacted SF. García-Lodeiro et al. (2010) suggested the possibility that a solid solution between stratlingite and C-S-H, which had not been yet identified, might be present. However, there is no evidence that the solid solution exists.

For the A-group sample, the SiO_2 content of the crystalline hydrates is higher compared to the molar ratio of stratlingite, and the element composition within the identical crystal is also heterogeneous. It is therefore considered that either a lot of unreacted SF exist around the microscopic crystal of stratlingite (Lopez et al., 2008), or a number of fine SF grains are present heterogeneously within a crystal of stratlingite. The analytical results obtained for the A-group sample failed to provide a reliable explanation for this problem.

For the B-group sample, the observation on the mirror-polished surface of stratlingite crystals with a high SiO_2 molar ratio revealed that irregularly-shaped grains composed of SF are attached on the mirror- polished surface of high SiO_2 region of the crystal. On the other hand, any adhesion/attachment of SF particles was not recognized on the smooth matrix of stratlingite crystal in which molar ratios of main components are close to stratlingite. Therefore, it can be concluded that SF grains were included into the stratlingite crystal during the

crystal growth.

Chapter V

Conclusion

Calcium aluminate cement (CAC) pastes with silica fume (SF) mixed with or without sodium tripolyphosphate (TPP) deflocculant were investigated to understand the stability behavior of the constituent phases at different physico-chemical conditions. The mixed pastes were casted into bottles or onto glass slides, and then cured at 10 °C, 21 °C, 23 °C, 30 °C, 35 °C, 50 °C and 60 °C. The time-dependent changes of phases in the samples were analyzed by XRD. The selected samples were observed and analyzed by EPMA, FE-SEM and TG - DTA. Several conclusions can be drawn from the present study as follows:

(1) C_2AH_8 hydrate had crystallized in almost all of the samples from the beginning of hydration, and its formation was further accelerated at higher curing temperature. The XRD intensity of C_2AH_8 decreased as time proceeded, while the intensity of stratlingite increased inversely. This result is consistent with those of previous researches that the C_2AH_8 hydrate was transferred to stratlingite.

(2) Crystallization of stratlingite was strongly affected by the curing temperature. The formation was further accelerated at higher curing temperatures, while the formation was extremely delayed at lower curing temperatures.

(3) EPMA analyses showed that stratlingite crystals occurred in close association with agglomerates of SF, and had higher molar ratio of SiO_2 than the theoretical value of stratlingite. This non-stoichiometric composition of stratlingite had been reported by many researchers.

(4) FE-SEM images and EDX analyses revealed the presence of irregularly

shaped small grains composed of SF as observed on the mirror-polished surface of high SiO_2 region of the stratlingite crystal. The high SiO_2 ratio of stratlingite can be explained by the contamination of the SF grains.

(5) Even after long-term curing, the peaks of the XRD intensity of stratlingite, gibbsite and C_3AH_6 hydrates (hydrogarnet) remained in the bottle samples, regardless of the presence or absence of TPP. Stratlingite, gibbsite and C_3AH_6 hydrates are considered to be stable phases. But these hydrates transferred to $CaCO_3$ in presence of atmospheric CO_2 on plate samples.

(6) The observations on surface of plate samples showed that the sample surfaces were strongly affected by the carbonation. Calcite ($CaCO_3$) had been crystallized in almost all of the samples from the beginning of hydration and was stable after long time of curing. Vaterite and aragonite ($CaCO_3$) crystallized after the crystallization of calcite, but finally disappeared.

(7) As an effect of deflocculant, sodium ions accelerated the crystallization of C_2AH_8 and stratlingite, as also pointed out in the previous studies. In addition, deflocculant also promoted the carbonation of sample surface. Furthermore, the effect of delaying the crystallization of C_3AH_6 (hydrogarnet) is suggested, but further detailed study is needed.

(8) An anomalous retardation of hardening time occurred at 28 - 30 ˚C on the neat calcium aluminate cement paste, which was pointed out in the previous studies, was not observed on the calcium aluminate cement paste added with SF in presence or absence of deflocculant. The addition of SF might have a causal influence on the retardation phenomenon.

References

Antonovic, V., Pundine, I., Stonys, R., Cesniene, J. and Keriene, J. (2010) A review of the possible applications of nanotechnology in refractory concrete. Jaournal of Civil Engineering and Management, Vol. 16 [4] pp. 595-602.

Bentsen, S., Seltveit, A. and Sandberg, B. (1990) Effect of microsilica on conversion of high alumina cement. Calcium Aluminate Cements, E.& F. N. Spon pp. 294-319.

Boch, Ph., Seisso, M., Vetter, G. and Jacquin, M. (1992) High-alumina cements for cesium trapping. Cement and Concrete Research, Vol.22 [2-3] pp. 369-374.

Bushnell-Watson, S. N. and Sharp, J. H. (1986) The effect of temperature upon the setting behavior of refractory calcium aluminate cements. Cement Concrete Reseach, Vol.16, [6] pp. 876-884.

Bushnell-Watson, S. N. and Sharp, J. H. (1990a) Further studies of the effect of temperature upon the setting behavior of refractory calcium aluminate cements. Cement Concrete Reseach, Vol.20, [4] pp. 623-635.

Bushnell-Watson, S. N. and Sharp, J. H. (1990b) On the case of the anomalous setting behavior with respect to temperature of calcium aluminate cements. Cement Concrete Reseach, Vol.20, [5] pp. 677-686.

Calvo, J. L. G., Alonso, M. C., Hidalgo, A., Luco, L. F. and Flor-Laguna, V. (2013) Development of low-pH cementitious materials based on CAC for HLW repositories: Long-term hydration and resistance against groundwater aggression. Cement and Concrete Research, Vol.51, pp. 67-77.

Colombo, C. and Violante, A. (1996) Effect of time and temperature on the chemical composition and crystallization of mixed iron and aluminum species. Clays and Clay Minerals Vol. 44 [1] pp. 113-120.

Concrete Society Working Party (1997) Calcium aluminate cement in construction: A re-assessment. Technical Report, No. 46, pp. 1-63.

Daspoddar, D., Das, S. K. and Daspoddar, P. K. (2003). Effect of silica sol of different routes on the properties of low cement castables. Bull. Mater. Sci., Vol. 26, [2] pp. 227-231.

Ding, J., Fu, Y. and Beaudoin, J. J. (1995), Strätlingite formation in high alumina cement-silica fume systems: significance of sodium ions. Cement Concrete

Reseach, Vol.26, [6] pp. 1311-1319.

Ding, J., Fu, Y. and Beaudoin, J. J. (1996a), Study of hydration mechanisms in the high alumina cement-sodium silicate system. Cement Concrete. Reseach, Vol. 26, [5] pp. 799-804.

Ding, J., Fu, Y. and Beaudoin, J. J. (1996b), Effect of different inorganic salts/alkali on conversion-prevention in high alumina cement products. Adovn. Cem. Bas. Mat. Vol. 4, pp. 43-47.

Edmonds, R. N. and Majumdar, A. J. (1989) The hydration of mixtures of monocalcium aluminate and blastfurnace slag. Cement Concrete. Reseach, Vol. 19, [5] pp. 779-782.

Eguchi, T., Takita, I., Yoshitomi, J., Kiritan,i S. and Sato, M. (1989) Low-cement-bonded castable refractories. Journal of the Technical Association of Refractories Japan (Taikabutsu Overseas), Vol. 9, [1] pp. 10-24.

Fentiman, C. H. (1985) Hydration of carbo-aluminous cement at different temperature. Cement Concrete. Reseach, Vol. 26, [4] pp. 622-630.

Fentiman, C. H., Rashid S., Bayoux, J. P., Bodin A. and Testud, N. (1990) The effect of curing conditions on the hydration and strength development in fondu : slag. Calcium Aluminate Cements, E.& F. N. Spon pp. 272-281.

Fernández-Carrasco, L. and Vázquez, E. (2009) Reactions of fly ash with calcium aluminate cement and calcium sulphate. Fuel 88 pp. 1533-1538.

Fernandez-Jimenez, A., Vazquez, T. and Palomo, A. (2011) Effect of sodium silicate on calcium aluminate cement hydration in high alkaline media: A microstructural characterization. J. Am. Ceram. Soc. Vol. 94, [4] pp. 1297-1303.

Fierens, P., Verhaegen, A. and Verhaegen, J. P. (1974) Etude de la formation de l'hydrocarboaluminate de calcium. Cem. Concr. Res., Vol 4, [5] pp. 695-707.

Fischer, R. and Kuzel, H. J. (1982) Reinvestigation of the system $C_4A{\cdot}nH_2O$ – $C_4A{\cdot}CO_2{\cdot}nH_2O$. Cem. Concr. Res., Vol. 12, [4] pp. 517-526.

Fu, Y., Ding, J. and Beaudoin, J. J. (1996) Zeolite-Based Additives for High Alumina Cement Products. Advanced Cement Based Materials, Vol 3, [1] pp. 37-42.

Fu, Y., Ding, J. and Beaudoin, J.J. (1997) Conversion-preventing additive for

high alumina cement products. US Patent, 5624489.

García-Lodeiro, I., Fernández-Jiménez, A, Macphee, D. E., Sobrados, I., Sanz, J. and Palomo, A. (2010) Stability of Synthetic Calcium Silicate Hydrate Gels in Presence of Alkalis. Journal of theTransportation Research Board Vol. 2142, [2] pp. 52-57.

Goñi, S. and Guerrero A. (2003) Accelated carbonation of Friedel's salt in calcium aluminate cement paste. Cem. Concr. Res., Vol. 33, [1] pp. 21-26.

Gosselin, C., Gallucci, E. and Scrivener, K. (2010) Influence of self heating and Li2SO4 addition on the microstructural development of calcium aluminate cement. Cem. Concr. Res., Vol. 40, [10] pp. 1555-1570.

Heikal, M., Radwan, M. M. and Morsy, M. S. (2004) Influence of curing temterature on the physico-chemical, characteristics of calcium aluminate cement with air-cooled slag or water-cooled slag. Ceram.-silikaty Vol. 48, [4] pp. 185-196.

Heikal, M., Morsy, M. S. and Radwan, M. M. (2005) Electrical conductivity and phase composition of calcium aluminate cement containing air-cooled and water-cooled slag at 20, 40 and 60°C. Cem. Concr. Res., Vol. 35, [7] pp. 1438-1446.

Heikal, M., Al-Duaij, O. K. and Ibrahim, N. S. (2015) Microstructure of composite cements containing blast-furnace slag and silica nano-particles subjected to elevated thermally treatment temperature. Construction and Building Materials Vol. 93, pp. 1067-1077.

Hentschel, G. and Kuzel, H. J. (1976) Strätlingit, $2CaO{\cdot}Al_2O_3{\cdot}SiO_2{\cdot}\ 8H_2O$, ein neues Mineral. Neues Jahrb. Mineral., Monatsh., pp. 326-330 (in German with English abs.).

Hirose, S., Yamazaki, Y. (1991) Hydration of high alumina cement mixed with blast furnace slag. Gypsum and Lime, No. 233, pp. 216-220.

International Centre for Diffraction data (ICDD. 2002) Power Diffraction File (PFD), Card No. 00-029-0285.

Jackson, M. D., Logan, J.M., Scheetz, B. E., Deocampo, D. M., Cawood, C. G., Marra, F. Vitti, M. and Ungaro, L. (2009) Assessment of material characteristics of ancient concretes, Grande Aula, Markets of Trajan, Rome. Journal of Archaeological Science, No. 36, pp. 2481-2492.

Jackson, M. D., Landis, E. N., Brune, P. F., Vitti, M., Chen, H., Li, Q., Kunz, M.,

Wenk, H.-R., Monterio, P. J. M. and Ingraffea, A. R., (2014) Mechanical resilience and cementitious processes in Imperial Roman architectural mortar. PNAS, December 30, vol. 111, No. 52, pp. 18484-18489.

Kirca, Ö., Yaman, İ. Ö. and Tokyay, M. (2013) Compressive strength development of calcium aluminate cement-GGBFS blends. Cement & Concrete Composites, Vol. 35, pp. 163-170.

Klaus, S. R., Neubauer, J. and Goetz-Neunhoeffer, F. (2013) Hydration Kinetics of CA_2 and CA-Investigations performed on a synthetic calcium aluminate cement. Cem. Concr. Res., Vol. 43, pp. 62-69.

Kloprogge, J. T., Ruan, H. D. and Frost, R. L. (2002) Thermal decomposition of bauxite minerals: infrared emission spectroscopy of gibbsite, boehmite and diaspore. Journal of Material Science, Vol. 37, pp. 1121-1129.

Kondo, R. (1968) Chemistry of alumina cements. Concrete Journal, Vol.6, No.12, pp. 4-8. (in japanese).

Kosmac, T., Lahajnar, G. and Sepe, A. (1993) Proton NMR relaxation study of calcium aluminate hydration reactions. Cement Concrete Reseach, Vol.23, No.1, pp. 1-6.

Lee, W.E. and Moor, R. E. (1998). Evolution of *in situ* refractories in the 20th century. Journal American Ceramic Soociety Vol. 81, [6] pp. 1385-1410.

López, A. H., Calvo, J. L. G., Olmo, J. G., Petit, S. and Alonso, M. C. (2008) Microstructural evolution of calium aluminate cements hydration with silica fume and fly ash additions by Scanning electron microscopy, and mid and near-infrared spectroscopy. Journal American Ceramic Soociety. Vol. 91, [4] pp. 1258-1265.

Maeda, E., Jono, K., Kanatani, S. and Haraoka, T. (2007) Analysis of setting mechanism of low-cement castables. Taikabutu Vol. 59, [5] pp. 224-234.

Majumdar, A. J., Singh, B. and Edmonds, R., N. (1989) Hydration of mixture of $C_{12}A_7$ and granulated blastfurnace slag. Cement and Concrete Research, Vol. 19, [6] pp. 848-856.

Majumdar, A. J., Edmonds, R., N. and Singh, B. (1990a) Hydration of Secar71 aluminous cement in presence of granulated blast furnace slag. Cement and Concrete Research. Vol. 20, [1] pp. 7-14.

Majumdar, A. Singh, B.J. and Edmonds, R. N. (1990b) Hydration of mixtures of 'Ciment Fondu' aluminous Cement and granulated blast furnace slag.

Cement and Concrete Research. Vol. 20, [2] pp. 197-208.

Majumdar, A. J. and Singh, B. (1992) Properties of some blended high- alumina cements. Cement and Concrete Research, Vol. 22, [6] pp. 1101-1114.

Matschei, T., Lothenbach, B. and Glasser, F. P. (2007) The AFm phase in portland cement. Cement and Concrete Research, Vol. 37, [2] pp. 118-130.

Midgley, H. G. and Rao, P. B. (1978) Formation of stratlingite $2CaO \cdot SiO_2 \cdot Al_2O_3 \cdot 8H_2O$ in relation to the hydration of high alumina cement. Cement and Concrete Research, Vol. 8, [2] pp. 169-172.

Mostafa, N. Y., Zaki, Z. I. and Elkader, O. H. A. (2012) Chemical activation of calcium aluminate cement composites cured at elebated temperature. Cement & Concrete Composites, Vol. 34, [10] pp. 1187-1193.

Nishikawa, A. (1999) Technology Monolithic Refractories, Revised Edition, Plibrico Japan Co., p. 24.

Ogino, T., Suzuki, T. and Sawada, K. (1989) The formation and transformation mechanism of calcium carbonate in water. Geochimica et Cosmochimica acta Vol. 51, pp. 2757-2767.

Parr, C., Simonin, F., Touzo, B., Wöhrmeyer, C., Valdelievre, B. and Namba, A. (2005) The impact of calcium aluminate cement hydration upon the properties of refractory castables. Taikabutsu, Vol. 57, [9] pp. 468-480.

Pivinskii, Y. E. (1998) New refractory concretes and binding system : Basic trends of development, production, and use of refractories in the 21st century, Refractries and Industrial Ceramics Vol. 39, [5-6] pp. 151-159.

Rao, P. B. and Viswanathan, V. N. (1980) Proc. Inter. Congr. Chem. Cem. Paris, ed. M. Regourd, Paris France, pp. 51-56.

Rayment, D. L. and Majumdar, A. J. (1994) Microanalysis of high-alumina cement clinker and hydrated HAC/SLAG mixtures. Cement and Concrete Research, Vol. 24, [2] pp. 335-342.

Reig, L., Soriano, L., Borrachero, M.V., Monz,_ J. and Pay, J. (2016) Influence of calcium aluminate cement (CAC) on alkaline activation of red clay brick waste (RCBW). Cement and Composites, Vol.65, pp. 177-185.

Richard, N., Lequeux, N. and Boch, P. (1993) : Journal de Physique IV, Colloque C7, supplément au Journal de Physique III, Vol. 3, pp. 1403-1406.

Richardson, I. G. and Groves, G. W. (1990) The microstructure of blastfurnace slag / high alumina cement pastes. Calcium Aluminate Cements, E. & F. N. Spon, pp. 282-293.

Rojas, M. F. and Rojas, M. I. S. (2003) The effect of high curing temperature on the reaction kinetics in MK/lime and MK-blended cement matrices at 60°C. Cement and Concrete Research, Vol. 33, (5) pp. 643-649.

Rojas, M. F. and Rojas, M. I. S. (2005) Inflence of metastable hydrated phases on the pore size distribution and degree of hydration of MK-blended cements cured at 60°C. Cement and Concrete Research, Vol. 35, [7] pp. 1292-1298.

Rojas, M. F. (2006) Study of hydrated phases present in a MK-lome system cured at 60°C and 60 months of reaction. Cement and Concrete Research, Vol. 36, [5] pp. 827-831.

Scrivener, K. L. and Capmas, A. (1998) Chapter 13. Calcium Aluminate Cements. Lea's Chemistry of Cement and Concrete (Fourth edition) pp. 713-782.

Sharp, J. H., Hill, J., Milestone, N. B. and Miller, E. W. (2003) Cementitious systems for encapsulation of intermediate level waste", Proc. of the Ninth International Conference on Radioactive Waste Management and Environmental Remediation, Oxford, Paper ICEM'03-4554.

Shinmei T., Ohkawa, M., Borovsky, A., Iiyama, M. and Parr, C. (2012a) Crystallization of stratlingite in high alumina cement-silica fume system with or without deflocculant, Journal of the Technical Association of Refractories Japan (Taikabutsu Overseas), Vol. 32, [1] pp. 3-11.

Singh, B., Majumdar, A. J. and Quillin, K. (1999) Properties of BRECEM : Ten-year results. Cement Concrete Reseach, Vol. 29, [3] pp. 429-433.

Soc, J. and Pavin, A. (1908) de Lafarge : French patent applications 320290, 391454.

The Pedigree, Tokyo Kogyo Boyeki Shokai,Ltd., (1997) p.5 (in Japanese).

The Association of Refractories, Japan (2001) Statistics : Refractories Production in japan. The monthly report, [5].

Tsuchida, T. and Ichikawa, N. (1989) Mechanochemical phenomena of gibbsite, bayerite and boehmite by grinding. Reactivity of solids, Vol. 7, pp. 207-217.

Yoshino, R, Mori, T., Hasegawa, A., Kinno, M., Uematsu, M., Hayashi, K. and Nakata, M. (2009) Development of low-activation design method for reduction of radioactive waste below clearance level (7) Trans.,SMiRT 19 paper #HW1/3.

Tables

Table 1. Classification of refractories (after the Japan Refractories Association).

1. Bricks and Shapes refractories (Fired bricks)
2. Monolithic refractories (Unshaped refractories)
2.1 Castable
2.2 Plastics
2.3 Gunning mix
2.4 Ramming mix
2.5 Patching, Coating, etc.
2.6 Mortar
2.7 Classify uncertain

Table 2. Hydration scheme for monocalcium aluminate (Parr et al., 2005).

Temperature	Hydration Reaction
<10 ºC	$CA + 10H \rightarrow CAH_{10}$
10 - 27 ºC	$2CA + 11H \rightarrow C_2AH_8 + AH_3$ $CA + 10H \rightarrow CAH_{10}$
>27 ºC	$3CA + 12H \rightarrow C_3AH_6 + 2AH_3$
F(t ºC + time)	$2CAH_{10} \rightarrow C_2AH_8 + AH_3 + 9H$ $C_2AH_8 \rightarrow 2C_3AH_6 + AH_3 + 9H$

Table 3. Chemical composition of the HAC and SF.

	HACd	HACk	SF4	SF7
Ig. Loss	0.16	0.14	<3	0.5
SiO_2	0.67	0.21	>93	98.4
Al_2O_3	73.73	69.49	<1	0.20
Fe_2O_3	0.20	0.17	<1	0.01
TiO_2	0.06	0.02		
CaO	25.10	29.79	<1.2	0.20
MgO	0.05	0.27	<0.5	0.10
Na_2O		0.21	<0.5	0.15
K_2O			<1	0.20
C			<2	0.50
Total	99.97	100.30		100.26

HACd: High-alumina cement, produced by Denki Kagaku Kogyo KK

HACk: Secar 71, 70% alumina cement, produced by Kerneos

SF4: SF-940-U silica fume produced by Elkem.

SF7: SF-971-U silica fume produced by Elkem.

Table 4. The hardening time of the B-group samples at different temperatures.

	10 ºC	21 ºC	30 ºC	35 ºC	50 ºC	60 ºC
hft-bottle	5h35m	8h10m	5h00m	6h20m	3h20m	2h20m
hf-bottle	5h00m	8h30m	5h50m	5h40m	3h20m	3h30m
hft-plate	7h25m	7h10m	5h00m	5h20m	3h00m	2h00m
hf-plate	*24h00m	6h50m	5h00m	5h00m	3h00m	2h25m

* The sample was not checked during the period from 7h25m to 24h00m.

Table 5. The initiation of crystallization as confirmed by XRD of the C_2AH_8 hydrates at different temperatures.

	10 ºC	21 ºC	30 ºC	35 ºC	50 ºC	60 ºC
hft-bottle	*24h00m	8h10m	5h00m	6h20m	3h20m	2h20m
hf-bottle	-	8h30m	8h50m	5h40m	3h20m	3h30m
hft-plate	7h25m	**24h00m	5h00m	5h20m	3h00m	2h00m
hf-plate	-	6h50m	5h00m	5h00m	3h00m	2h25m

* The sample was not checked during the period from 7h25m to 24h00m.

** The sample was not checked during the period from 8h30m to 24h00m.

- : not crystallized.

Table 6. The time required to reach the maximum XRD intensities of the C_2AH_8 hydrates at different temperatures.

	10 ºC	21 ºC	30 ºC	35 ºC	50 ºC	60 ºC
hft-bottle	13days	7days	3days	3days	1day	7h10m
hf-bottle	-	3days	2days	3days	3h20m	3h30m
hft-plate	2days	2days	5h00m	2days	3h00m	2h00m
hf-plate	-	6h50m	1day	1day	3h00m	2h25m

- : not crystallized.

Table 7. Maximum XRD intensity of the C_2AH_8 hydrates crystallized at different temperatures (I/Io).

	10 ºC	21 ºC	30 ºC	35 ºC	50 ºC	60 ºC
hft-bottle	0.14	0.28	1.15	1.08	0.38	0.17
hf-bottle	-	0.17	1.11	0.99	0.67	1.29
hft-plate	0.31	0.11	0.41	0.18	0.66	2.69
hf-plate	-	0.9	0.38	1.50	0.86	2.02

- : not crystallized.

Table 8. The initiation of crystallization as confirmed by XRD of the stratlingite at different temperatures.

	10 ºC	21 ºC	30 ºC	35 ºC	50 ºC	60 ºC
hft-bottle	149days	13 days	6 days	2 days	1 day	2h20m
hf-bottle	-	16 days	5 days	5 days	1 day	1 days
hft-plate	-	14 days	-	3 days	2 days	1 days
hf-plate	-	-	9 days	5 days	8 days	1 days

- : not crystallized.

Table 9. The time (days) required to reach the maximum XRD intensities of the stratlingite at different temperatures.

	10 ºC	21 ºC	30 ºC	35 ºC	50 ºC	60 ºC
hft-bottle	149	34	14	8	3	8
hf-bottle	-	34	11	10	1	3
hft-plate	-	14	-	3	5	2
hf-plate	-	-	11	10	9	1

- : not crystallized.

Table 10. The maximum XRD intensities of stratlingite at different temperatures (I/Io).

	10 ºC	21 ºC	30 ºC	35 ºC	50 ºC	60 ºC
hft-bottle	0.07	0.20	1.33	0.60	1.20	0.59
hf-bottle	-	0.15	0.25	0.66	0.05	0.38
hft-pottle	-	0.25	-	0.05	0.43	3.62
hf-plate	-	-	0.10	0.45	0.20	0.38

- : not crystallized.

Table 11. The initiation of crystallization as confirmed by XRD of the gibbsite at different temperatures.

	10 ºC	21 ºC	30 ºC	35 ºC	50 ºC	60 ºC
hft-bottle	2days	1 day	5h00m	6h20m	3h20m	2h20m
hf-bottle	14 days	2 days	5h50m	1 day	3h20m	3h30m
hft-plate	2 days	2 days	5h00m	1 day	3h00m	2h00m
hf-plate	759 days	7 days	5h00m	1 day	1 day	5h00m

Table 12. The results of EPMA analyses of the HACd + SF4 pastes (mass percent).

	CaO	Al_2O_3	SiO_2	H_2O^*
S1 plate-shaped hydrate	19.70	18.54	39.19	21.88
S2 plate-shaped hydrate	19.01	19.21	41.75	19.51
S3 plate-shaped hydrate	20.48	19.89	37.58	21.41
S4 plate-shaped hydrate	29.78	28.63	12.38	28.70
S5 plate-shaped hydrate	21.80	21.44	34.63	21.33
S6 plate-shaped hydrate	15.93	26.14	33.05	24.24
S7 plate-shaped hydrate	18.76	28.24	41.20	21.36
S8 plate-shaped hydrate	18.91	20.54	37.31	22.68
S9 plate-shaped hydrate	20.28	20.05	39.42	19.71
S10 plate-shaped hydrate	23.64	22.23	28.65	25.03
S11 plate-shaped hydrate	24.74	23.64	26.43	24.65
S12 thin-plate-shaped hydrate	13.17	14.90	10.05	61.60
S13 matrix	1.54	3.12	53.56	41.00
S14 matrix	3.19	38.87	39.44	17.71
S15 matrix	1.40	10.72	36.26	51.12

* H_2O is estimated as100 - (total mass% of SiO_2, TiO_2, Al_2O_3, Fe_2O_3, MgO, CaO, Na_2O, K_2O and P_2O_5)

Table 13. The results of EPMA analyses of the HACd+SF4 pastes (molar ratio).

	CaO	Al_2O_3	SiO_2	H_2O^*
S1 plate-shaped hydrate	1.93	1.00	3.59	6.68
S2 plate-shaped hydrate	1.80	1.00	3.69	5.75
S3 plate-shaped hydrate	1.87	1.00	3.21	6.09
S4 plate-shaped hydrate	1.89	1.00	0.73	5.67
S5 plate-shaped hydrate	1.85	1.00	2.73	5.63
S6 plate-shaped hydrate	1.11	1.00	2.15	5.25
S7 plate-shaped hydrate	1.87	1.00	3.83	6.63
S8 plate-shaped hydrate	1.67	1.00	3.08	6.25
S9 plate-shaped hydrate	1.84	1.00	3.34	5.56
S10 plate-shaped hydrate	1.93	1.00	2.19	6.37
S11 plate-shaped hydrate	1.90	1.00	1.90	5.90
S12 thin-plate-shaped hydrate	1.61	1.00	1.14	23.40
S13 matrix	0.90	1.00	29.09	74.28
S14 matrix	0.15	1.00	1.72	2.58
S15 matrix	0.24	1.00	5.74	27.00

* H_2O is estimated as100 - (total mass% SiO_2, TiO_2, Al_2O_3, Fe_2O_3, MgO, CaO, Na_2O, K_2O and P_2O_5).

Table 14. The results of EPMA analyses of the bottle samples at 21 ˚C and 35 ˚C (mass percent).

	CaO	Al_2O_3	SiO_2	H_2O^*
P1	18.82	34.84	1.00	45.08
P2	34.49	63.21	0.05	2.02
P3	24.80	24.85	17.20	32.99
P4	19.63	20.96	33.78	25.22
P5	17.47	17.65	40.87	23.71
P6	35.43	29.57	1.79	33.03
P7	32.81	29.49	6.04	31.51
P8	31.99	29.62	6.67	31.47
P9	28.08	39.59	2.93	29.06
P10	17.43	16.78	44.33	21.27
P11	21.25	21.11	35.13	22.19
P12	19.96	19.33	39.44	21.03
P13	18.29	18.27	39.99	23.20
P14	18.08	17.64	41.24	22.80
P15	17.38	17.14	42.01	23.26
P16	16.82	17.61	41.43	23.90
P17	18.60	19.24	37.82	24.04
P18	18.53	19.82	35.36	26.11
P19	0.91	2.15	53.62	42.97
P20	2.77	31.16	56.34	9.29
P21	16.76	22.18	38.45	22.38
P22	16.95	23.38	36.62	22.54
P23	15.68	24.10	37.90	22.04
P24	17.51	19.46	37.07	25.72
P25	21.69	20.56	36.54	21.01
P26	19.03	18.91	42.47	19.37
P27	0.75	3.41	73.55	21.85
P28	19.35	20.24	37.88	22.33
P29	22.22	22.60	27.95	27.09
P30	17.09	20.47	37.12	25.18
P31	25.98	25.69	16.94	31.25
P32	0.78	2.78	57.88	38.24
P33	27.69	25.48	13.73	33.02
P34	19.72	18.90	37.34	23.86
P35	34.34	22.40	20.68	22.35

* H_2O is estimated as100 - (total mass% SiO_2, TiO_2, Al_2O_3, Fe_2O_3, MgO, CaO, Na_2O, K_2O and P_2O_5)

Table 15. The results of EPMA analyses of the plate samples at 21 ˚C and 35 ˚C (mass percent).

	CaO	Al_2O_3	SiO_2	CO_2*
P46	57.28	0.10	0.04	42.54
P47	56.23	0.24	0.07	43.41
P55	42.15	0.28	0.19	57.36
P69	54.86	0.09	0.06	44.97
P71	35.89	0.11	0.13	63.84
P72	56.81	0.17	0.16	42.73
P73	56.11	0.08	0.03	43.72
P76	55.56	0.35	0.04	43.65
P77	56.93	0.22	0.00	42.28
P78	52.35	4.99	0.09	42.33
P79	53.90	1.30	0.05	44.58
P80	54.74	0.14	0.00	44.97
P81	55.37	0.10	0.02	44.36
P82	51.63	0.22	0.00	48.06
P103	56.68	0.07	0.00	42.99
P104	51.41	2.96	1.92	43.64
P105	52.76	0.90	0.32	45.57
P106	50.40	0.25	0.38	48.83

* CO_2 is estimated as 100 - (total mass% of SiO_2, TiO_2, Al_2O_3, Fe_2O_3, MgO, CaO, Na_2O, K_2O and P_2O_5).

Table 16. The results of EPMA analyses of the plate samples at 21 ˚C and 35 ˚C (mass percent).

	CaO	Al_2O_3	SiO_2	H_2O*
P54	7.52	54.67	9.62	27.61
P70	1.18	23.62	71.24	2.55
P74	0.64	8.95	79.45	9.91
P83	22.22	36.08	0.62	40.57
P101	4.59	49.39	30.53	1.75
P102	17.61	54.43	0.24	27.57

* H_2O is estimated as100 - (total mass% SiO_2, TiO_2, Al_2O_3, Fe_2O_3, MgO, CaO, Na_2O, K_2O and P_2O_5).

Table 17. The results of EPMA analyses of the bottle samples at 21˚C and 35˚C (molar ratio).

	CaO	Al_2O_3	SiO_2	H_2O^*	Main phases (presumed)
P1	0.98	1.00	0.05	7.32	CAH_{10}
P2	0.99	1.00	0.00	0.18	CA+H
P3	1.81	1.00	1.17	7.51	C_2ASH_8
P4	1.70	1.00	2.74	6.81	C_2ASH_8 + SF
P5	1.80	1.00	3.93	7.60	C_2ASH_8 + SF
P6	2.18	1.00	0.10	6.32	C_2AH_8
P7	2.02	1.00	0.35	6.05	C_2AH_8
P8	1.96	1.00	0.38	6.01	C_2AH_8
P9	1.29	1.00	0.13	4.15	CAH_{10}
P10	1.89	1.00	4.48	7.18	C_2ASH_8 + SF
P11	1.83	1.00	2.82	5.95	C_2ASH_8 + SF
P12	1.88	1.00	3.46	6.16	C_2ASH_8 + SF
P13	1.82	1.00	3.71	7.19	C_2ASH_8 + SF
P14	1.86	1.00	3.97	7.32	C_2ASH_8 + SF
P15	1.84	1.00	4.16	7.68	C_2ASH_8 + SF
P16	1.74	1.00	3.99	7.68	C_2ASH_8 + SF
P17	1.76	1.00	3.34	7.07	C_2ASH_8 + SF
P18	1.70	1.00	3.03	7.46	C_2ASH_8 + SF
P19	0.76	1.00	42.3	112.97	SF
P20	0.16	1.00	3.07	1.69	SF + AH_3
P21	1.37	1.00	2.94	5.71	CAH_{10} + SF
P22	1.32	1.00	2.66	5.53	CAH_{10} + SF
P23	1.18	1.00	2.67	5.18	CAH_{10} + SF
P24	1.64	1.00	3.23	7.48	C_2ASH_8 + SF
P25	1.92	1.00	3.02	5.78	C_2ASH_8 + SF
P26	1.83	1.00	3.81	5.80	C_2ASH_8 + SF
P27	0.40	1.00	36.6	36.27	SF
P28	1.74	1.00	3.18	6.24	C_2ASH_8 + SF
P29	1.79	1.00	2.10	6.78	C_2ASH_8 + SF
P30	1.52	1.00	3.08	6.96	C_2ASH_8 + SF
P31	1.84	1.00	1.12	6.89	C_2ASH_8
P32	0.51	1.00	35.34	77.88	SF
P33	1.98	1.00	0.91	7.33	C_2ASH_8
P34	1.90	1.00	3.35	7.15	C_2ASH_8 + SF
P35	2.79	1.00	1.57	5.65	C_3ASH_6

Abbreviations- AH_3 : $Al_2O_3 \cdot 3H_2O$, H : H_2O, CAH_{10} : $CaO \cdot Al_2O_3 \cdot 10H_2O$, C_2AH_8 : $2CaO \cdot Al_2O_3 \cdot 8H_2O$, C_2ASH_8 : Stratlingite, SF : Silica fume. * H_2O is estimated as100 - (total mass% SiO_2, TiO_2, Al_2O_3, Fe_2O_3, MgO, CaO, Na_2O, K_2O and P_2O_5).

Table 18. The results of EPMA analyses of the plate samples at 21˚C and 35˚C (molar ratio).

	CaO	Al_2O_3	SiO_2	CO_2^*	Main phases (presumed)
P46	1063	1.00	0.68	2457	$CaCO_3$
P47	433	1.00	0.52	1041	$CaCO_3$
P55	278	1.00	1.16	1176	$CaCO_3$
P69	1146	1.00	1.13	2926	$CaCO_3$
P71	599	1.00	1.98	3315	$CaCO_3$
P72	622	1.00	1.60	1457	$CaCO_3$
P73	1244	1.00	0.68	3017	$CaCO_3$
P76	290	1.00	0.19	710	$CaCO_3$
P77	475	1.00	0.00	1098	$CaCO_3$
P78	19	1.00	0.03	48	$CaCO_3$ + A
P79	75	1.00	0.07	194	$CaCO_3$ + A
P80	732	1.00	0.00	1872	$CaCO_3$
P81	1027	1.00	0.29	2562	$CaCO_3$
P82	425	1.00	0.00	1231	$CaCO_3$
P103	1538	1.00	0.00	3632	$CaCO_3$
P104	32	1.00	1.10	83	$CaCO_3$ + A
P105	107	1.00	0.61	288	$CaCO_3$
P106	373	1.00	2.62	1123	$CaCO_3$

Abbreviation, A : Al_2O_3, $CaCO_3$: $CaO \cdot CO_2$.

* CO_2 is estimated as 100 - (total mass% of SiO_2, TiO_2, Al_2O_3, Fe_2O_3, MgO, CaO, Na_2O, K_2O and P_2O_5).

Table 19. The results of EPMA analyses of the plate samples at 21˚C and 35˚C (molar raitio).

	CaO	Al_2O_3	SiO_2	H_2O	Main phases (presumed)
P54	0.25	1.00	0.30	2.86	AH_3
P70	0.09	1.00	5.12	0.61	SF
P74	0.13	1.00	15.05	6.27	SF+A
P83	1.12	1.00	0.03	6.36	CAH_{10}
P101	0.17	1.00	1.05	1.75	SF+A
P102	0.59	1.00	0.01	2.87	A

Abbreviation, A : Al_2O_3, AH_3 : $Al_2O_3 \cdot 3H_2O$, SF : Silica fume, CAH_{10} : $CaO \cdot Al_2O_3 \cdot 10H_2O$,

*H_2O is estimated as 100 - (total mass% of SiO_2, TiO_2, Al_2O_3, Fe_2O_3, MgO, CaO, Na_2O, K_2O and P_2O_5).

Figures

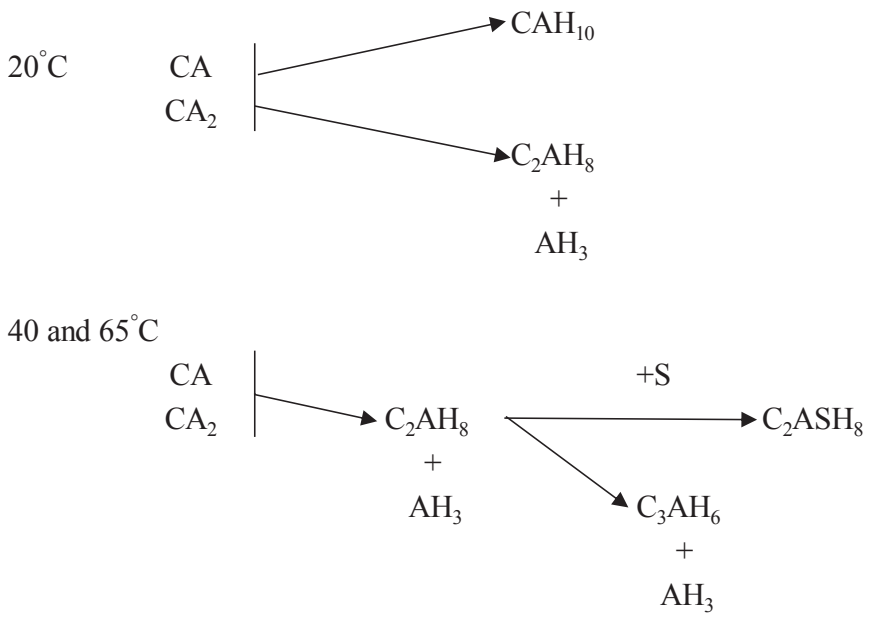

Figure 1. The conversion schemes of the hydrates of calcium aluminate cement with silica fume (after Bentosen et al., 1990). CA : $CaO \cdot Al_2O_3$, CA_2 : $CaO \cdot 2Al_2O_3$, CAH_{10} : $CaO \cdot Al_2O_3 \cdot 10H_2O$, C_2AH_8 : $2CaO \cdot Al_2O_3 \cdot 8H_2O$, AH_3 : $Al_2O_3 \cdot 3H_2O$, C_3AH_6 : $3CaO \cdot Al_2O_3 \cdot 6H_2O$, S : SiO_2, C_2ASH_8 : $2CaO \cdot Al_2O_3 \cdot SiO_2 \cdot 8H_2O$.

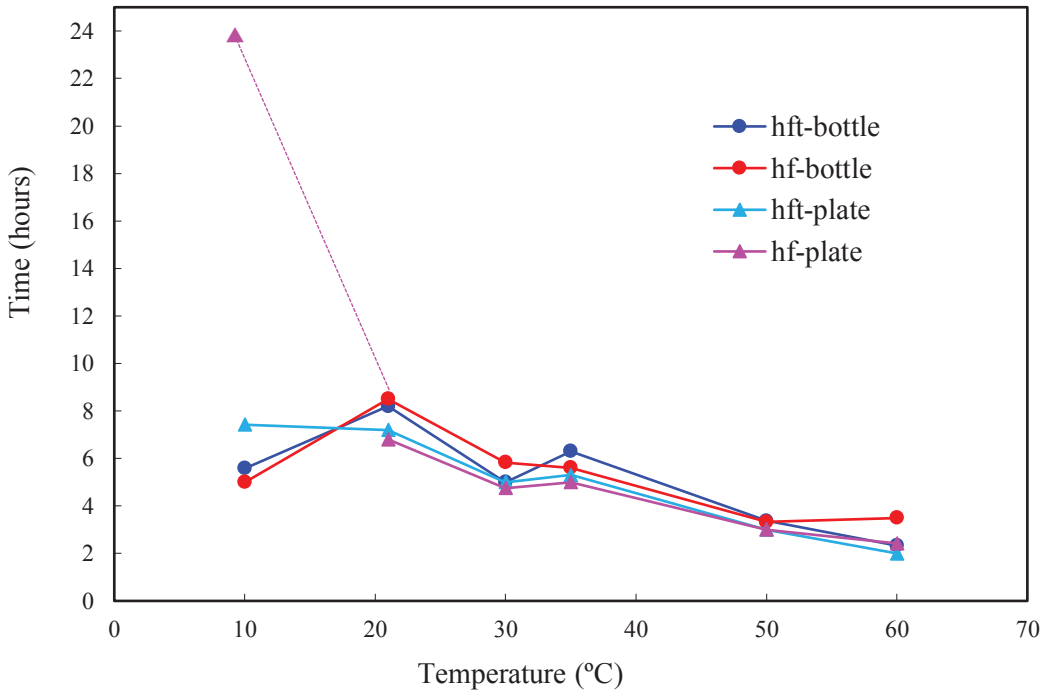

Figure 2. The hardening time of the B-group samples at different temperatures. Dotted line portion is connection based on speculation.

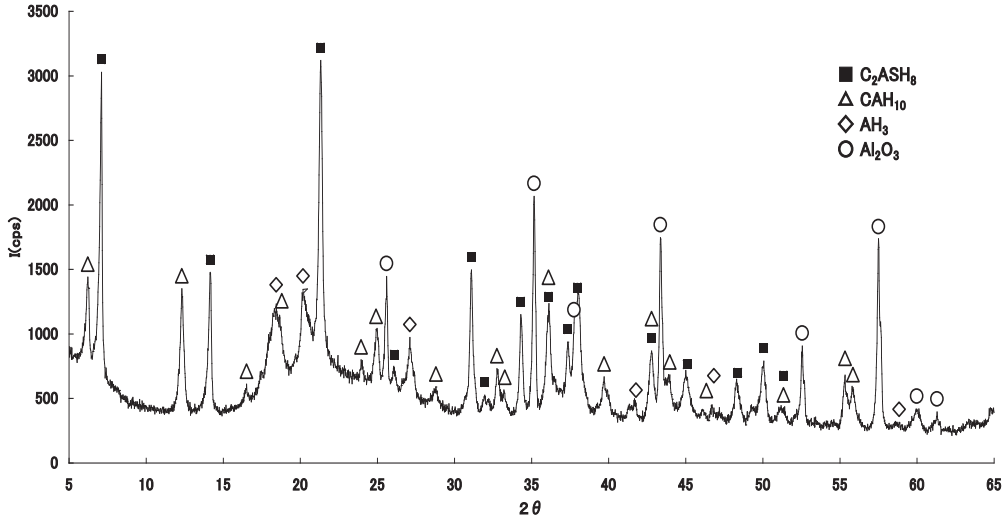

Figure 3. The powder X-ray diffraction pattern of the hydrated HAC+SF. Peaks indexed are marked as ■: C_2ASH_8 (stratlingite), △: CAH_{10}, ◇: AH_3, ○: Al_2O_3.

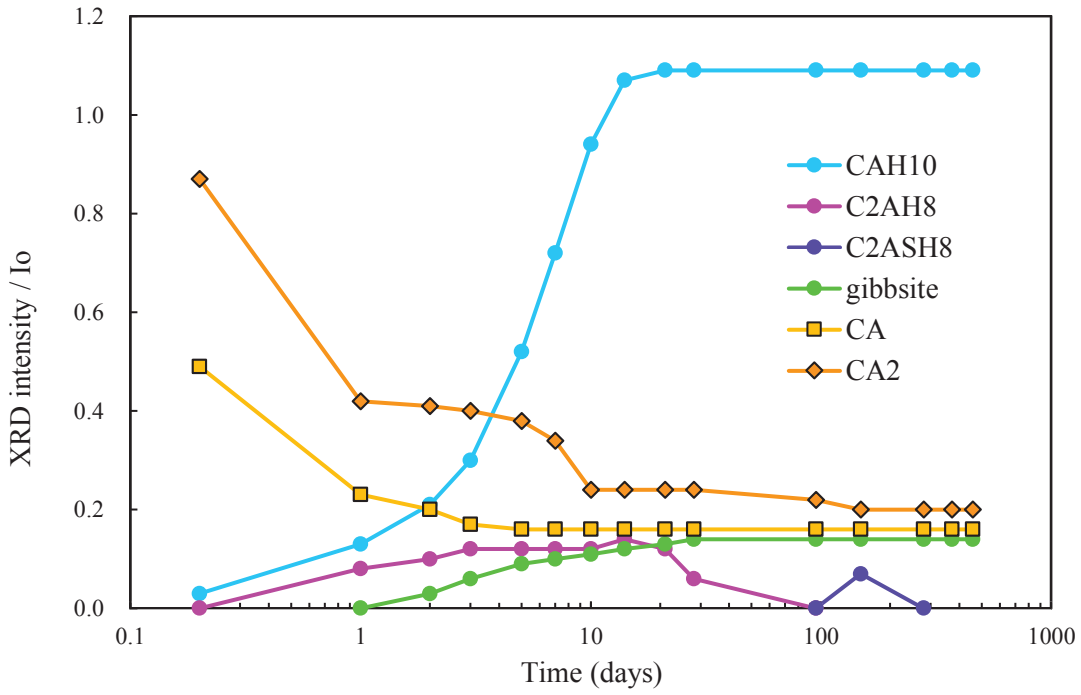

Figure 4. The XRD intensity ratios of different phases and their variations with curing time for the bottle sample hft-10b. Note that the horizontal time axis is in logarithmic scale. It is the same for all the subsequent figures, e.g. till figure 27.

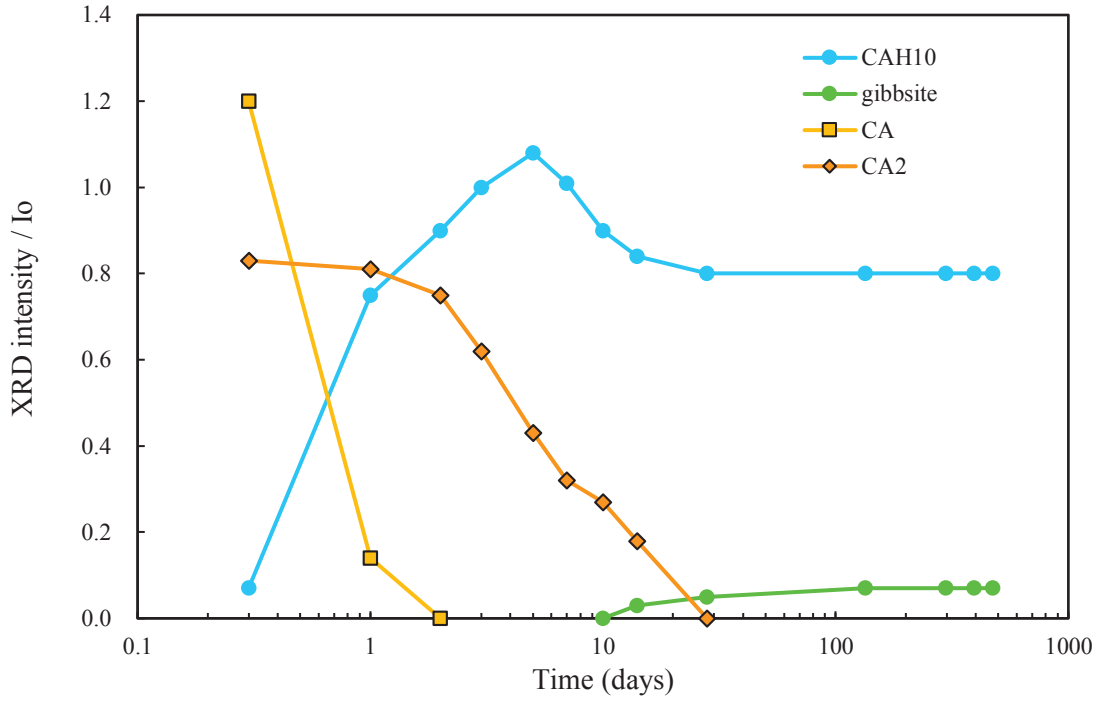

Figure 5. The XRD intensity ratios of different phases and their variations with curing time for the bottle sample hf-10b.

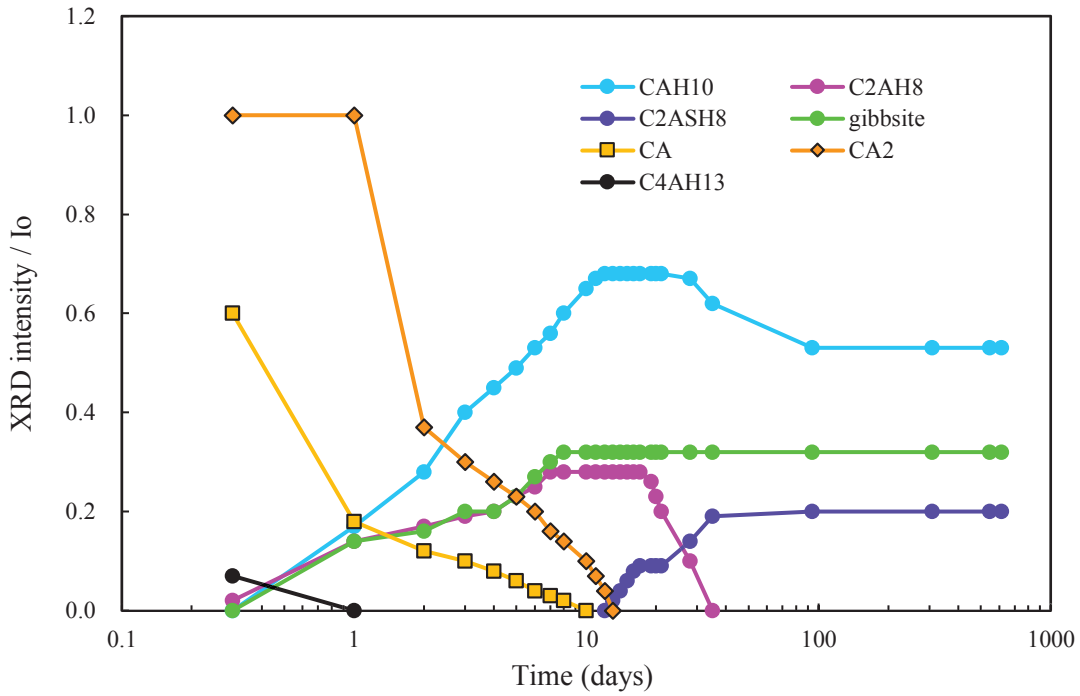

Figure 6. The XRD intensity ratios of different phases and their variations with curing time for the bottle sample hft-21b.

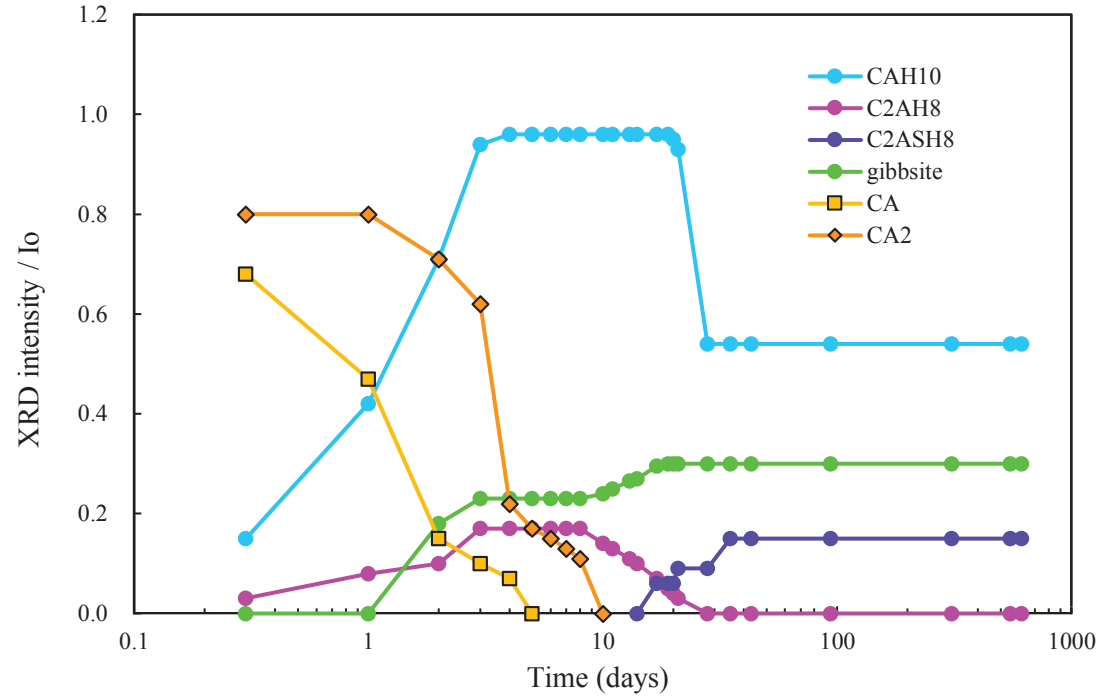

Figure 7. The XRD intensity ratios of different phases and their variations with curing time for the bottle sample hf-21b.

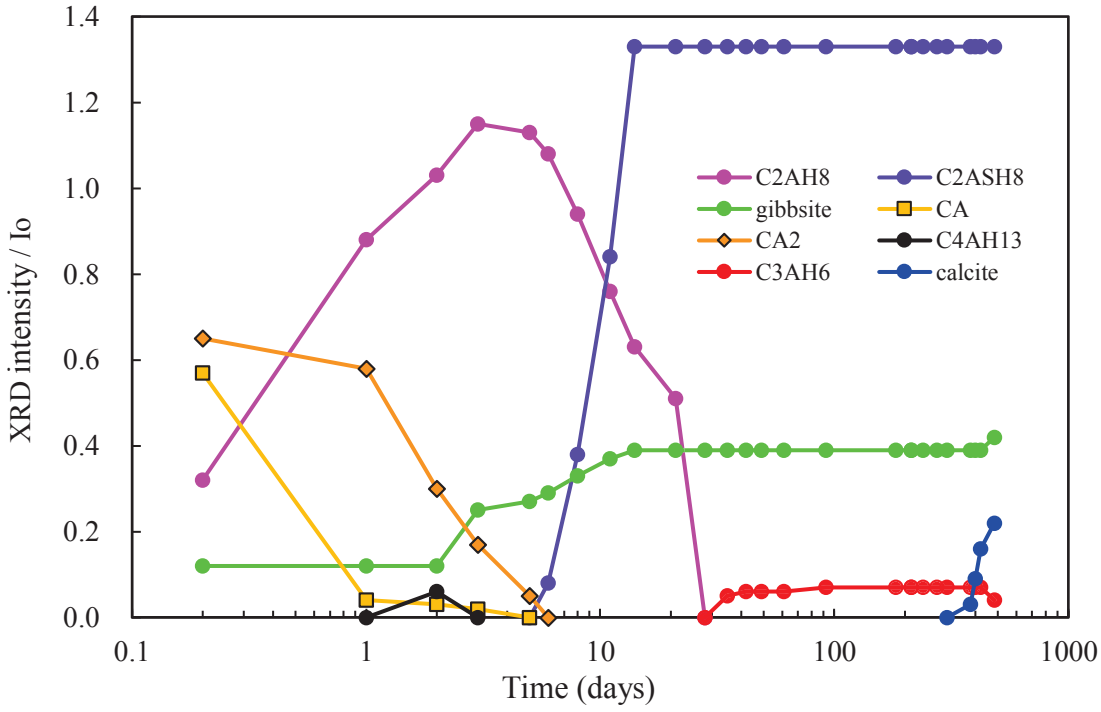

Figure 8. The XRD intensity ratios of different phases and their variations with curing time for the bottle sample hft-30b.

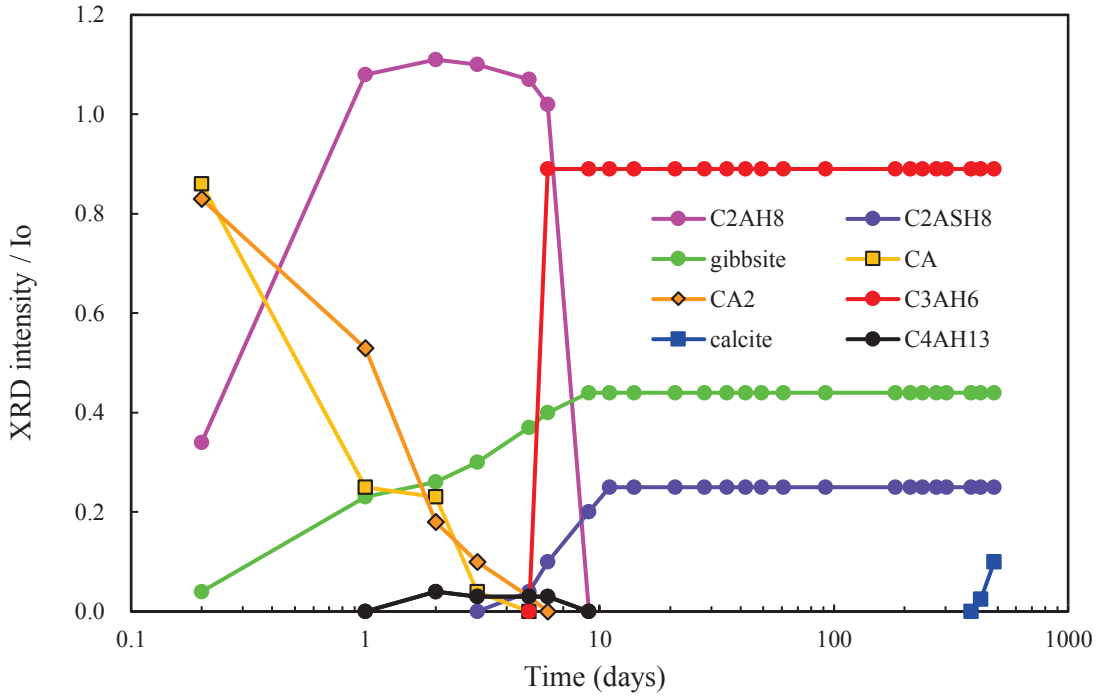

Figure 9. The XRD intensity ratios of different phases and their variations with curing time for the bottle sample hf-30b.

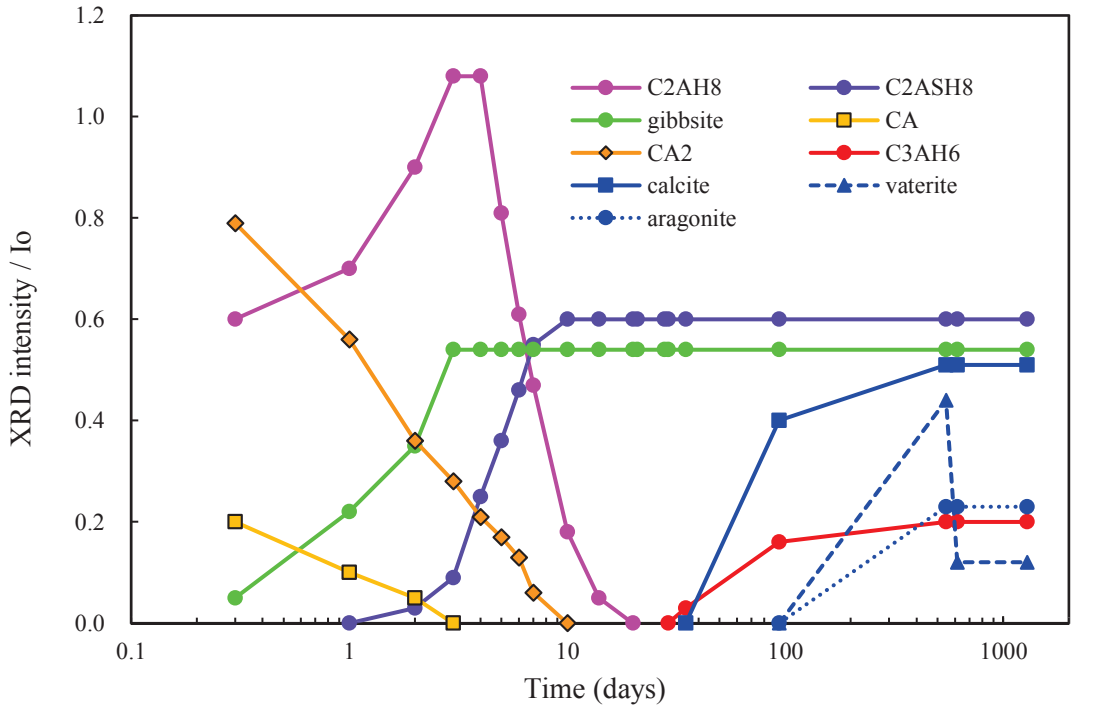

Figure 10. The XRD intensity ratios of different phases and their variations with curing time for the bottle sample hft-35b.

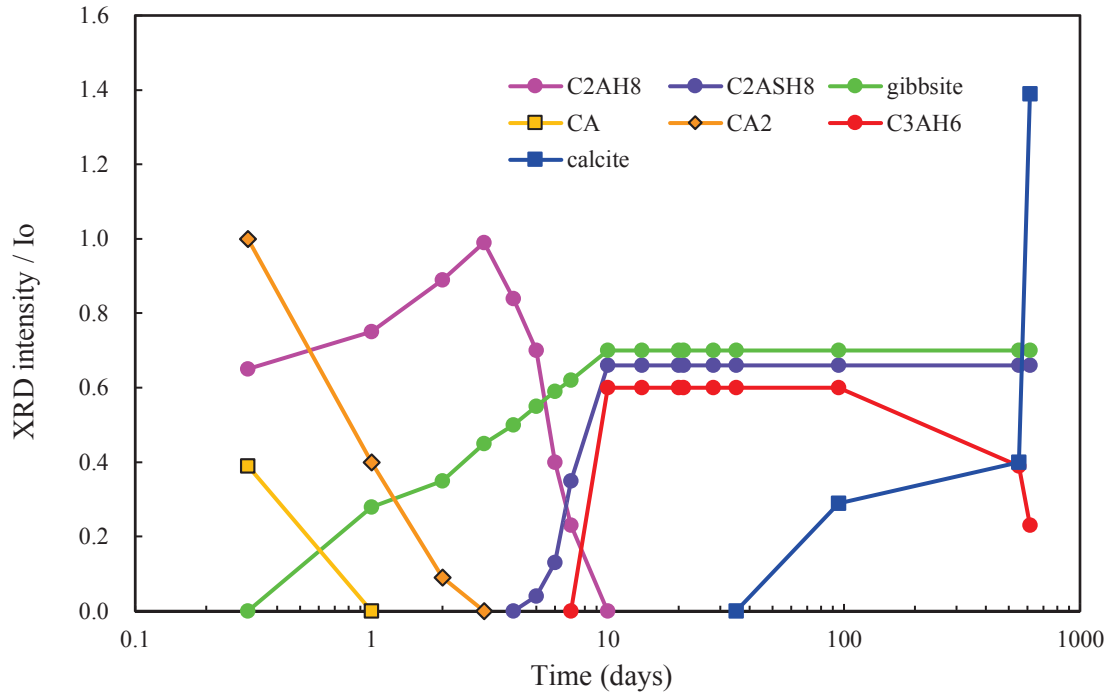

Figure 11. The XRD intensity ratios of different phases and their variations with curing time for the bottle sample hf-35b.

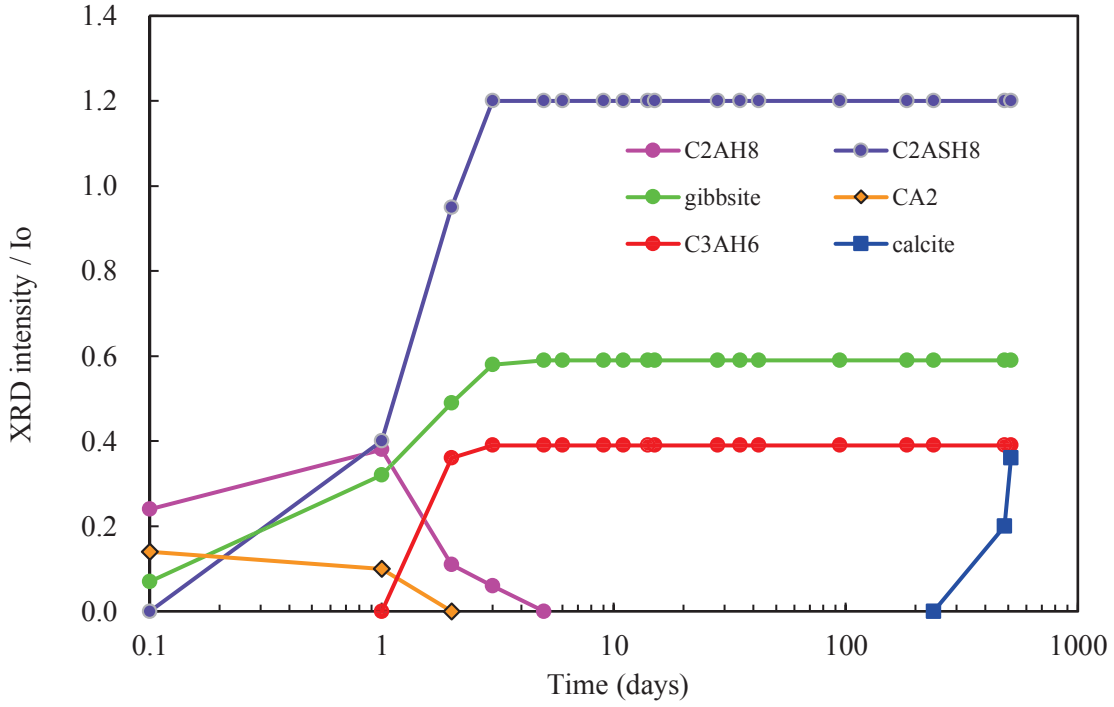

Figure 12. The XRD intensity ratios of different phases and their variations with curing time for the bottle sample hft-50b.

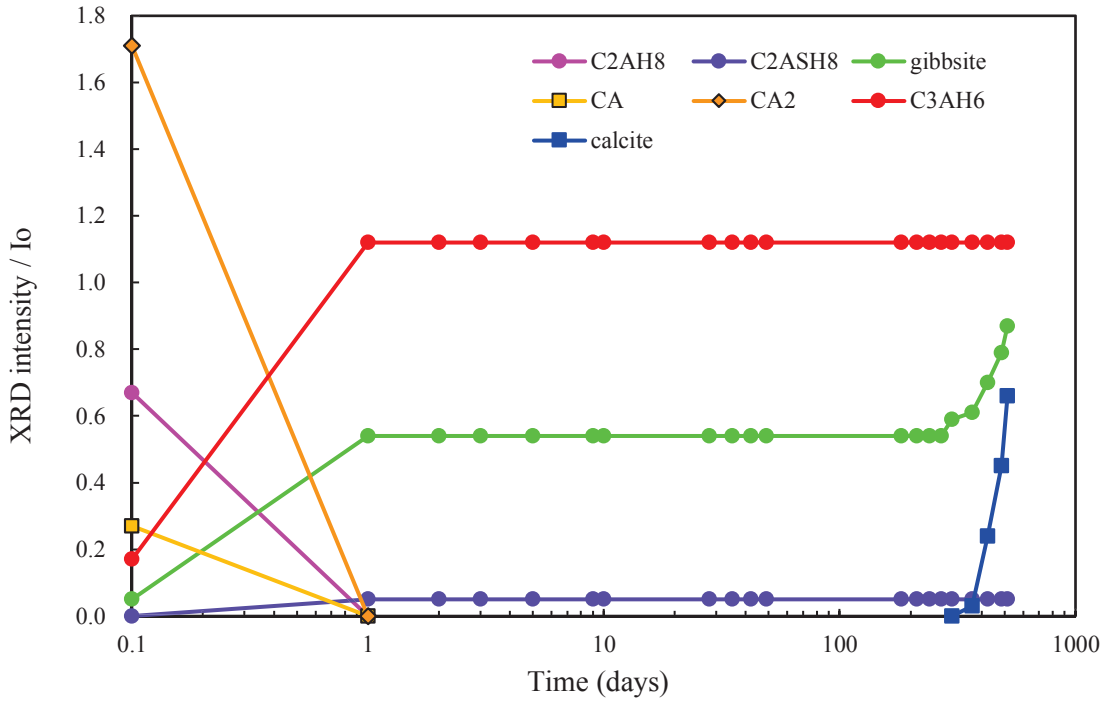

Figure 13. The XRD intensity ratios of different phases and their variations with curing time for the bottle sample hf-50b.

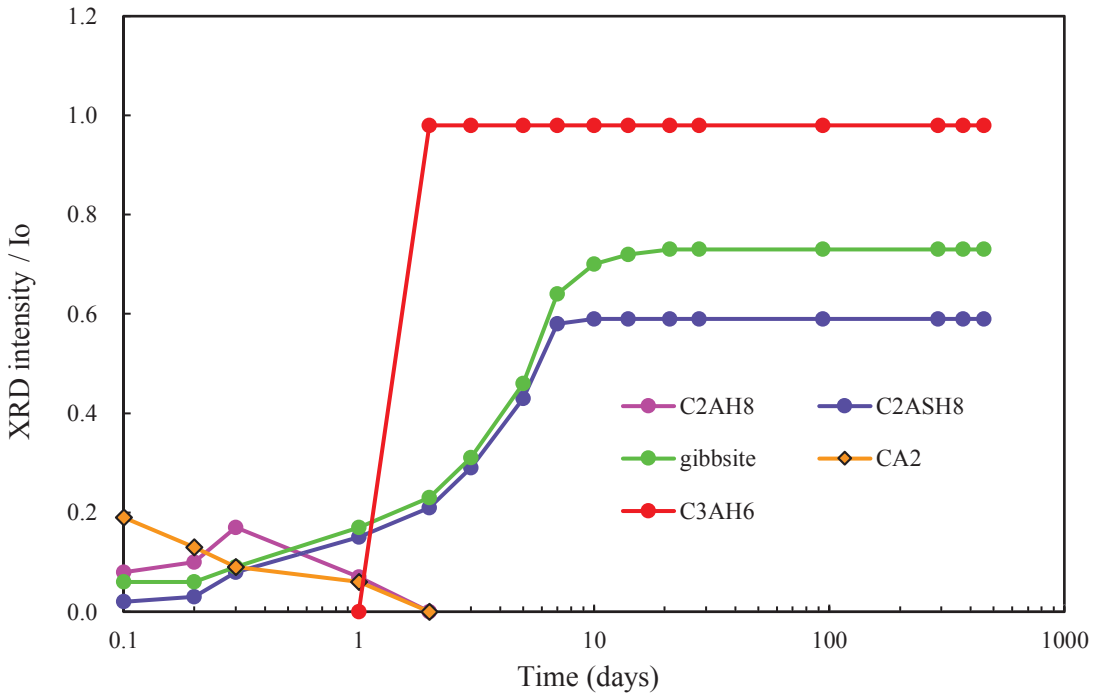

Figure 14. The XRD intensity ratios of different phases and their variations with curing time for the bottle sample hft-60b.

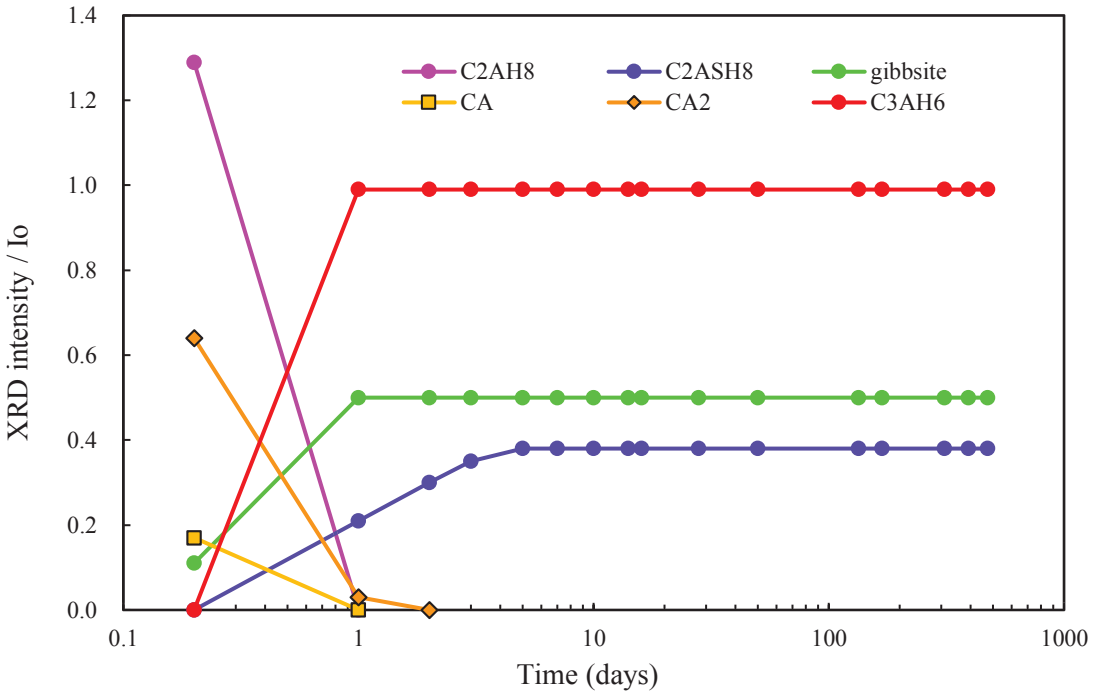

Figure 15. The XRD intensity ratios of different phases and their variations with curing time for the bottle sample hf-60b.

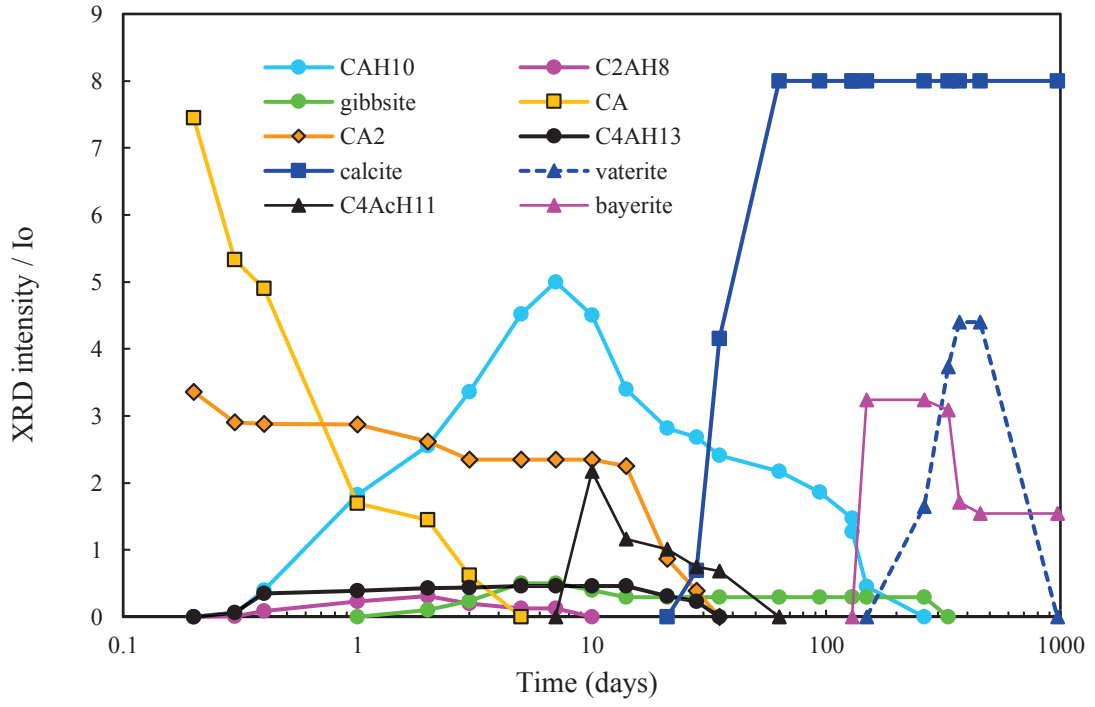

Figure 16. The XRD intensity ratios of different phases and their variations with curing time for the plate sample hft-10p.

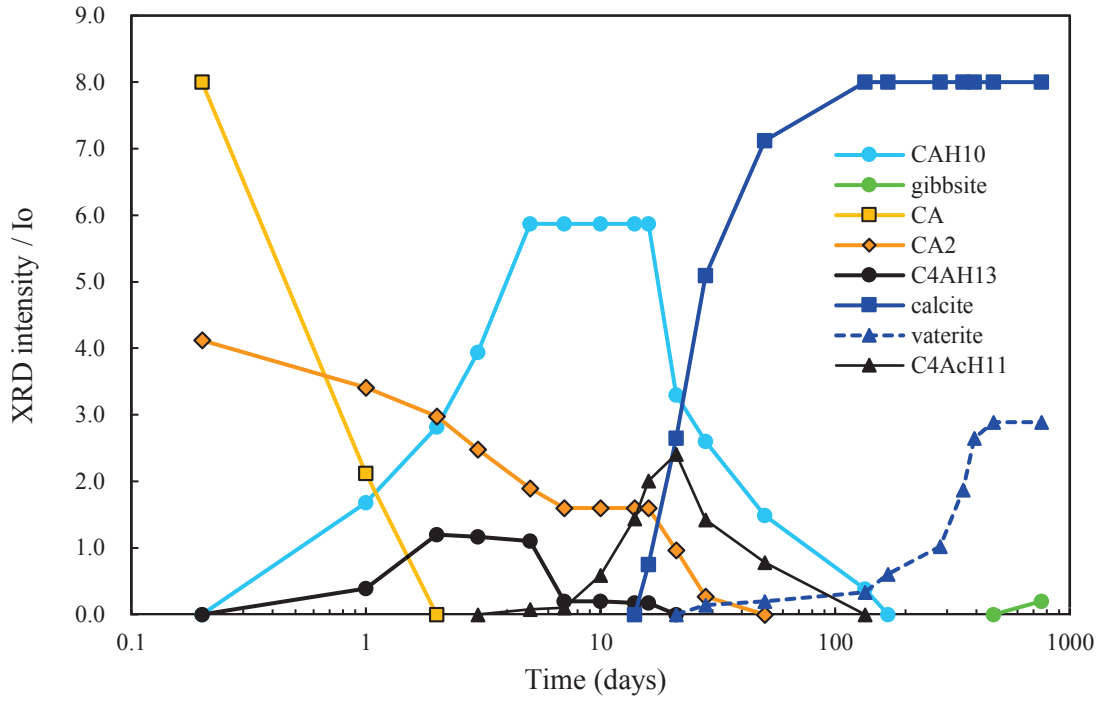

Figure 17. The XRD intensity ratios of different phases and their variations with curing time for the plate sample hf-10p.

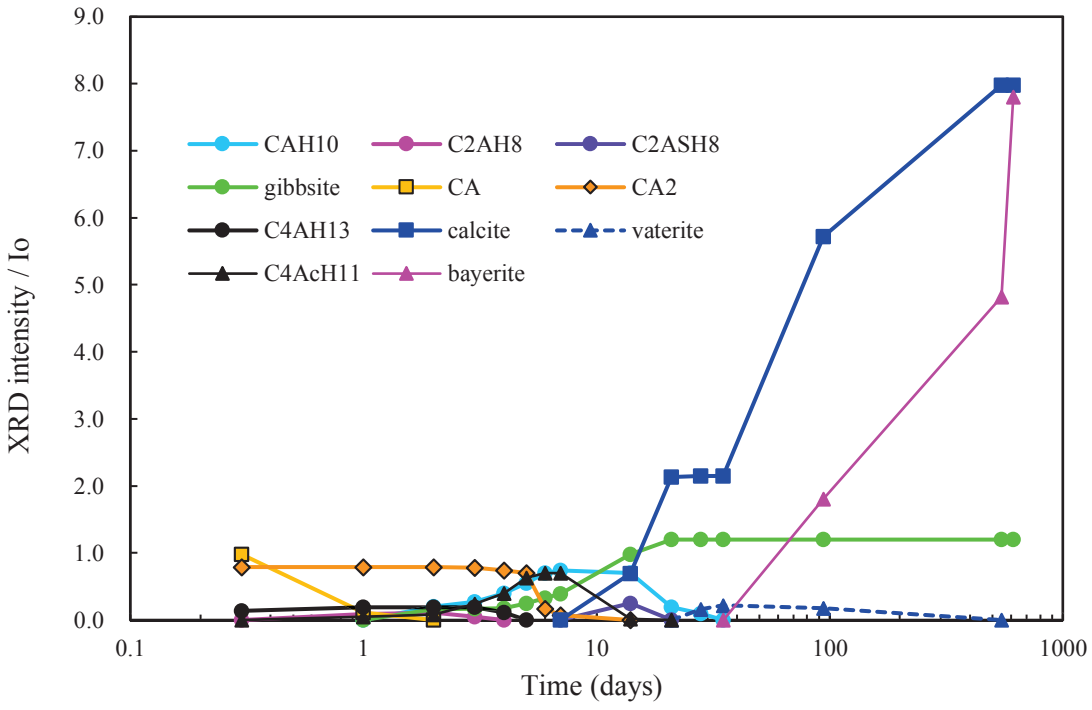

Figure 18. The XRD intensity ratios of different phases and their variations with curing time for the plate sample hft-21p.

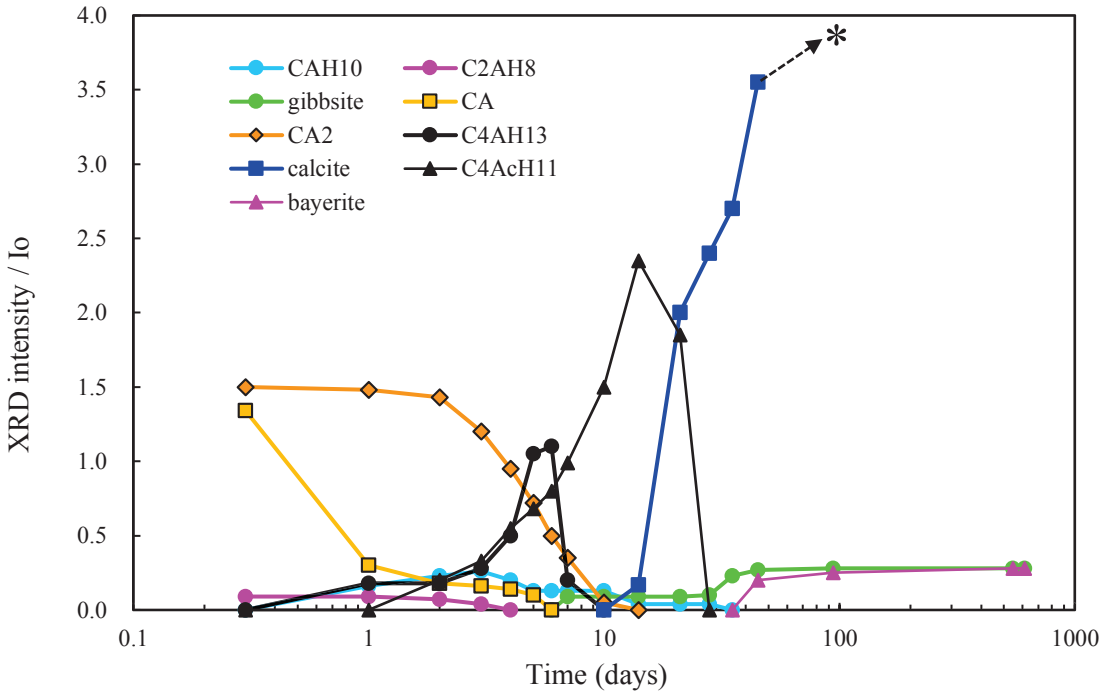

Figure 19. The XRD intensity ratios of different phases and their variations with curing time for the plate sample hf-21p. * represents a point after 94 days for calcite when intensity ratio increased to 7.74 beyond the present plot area.

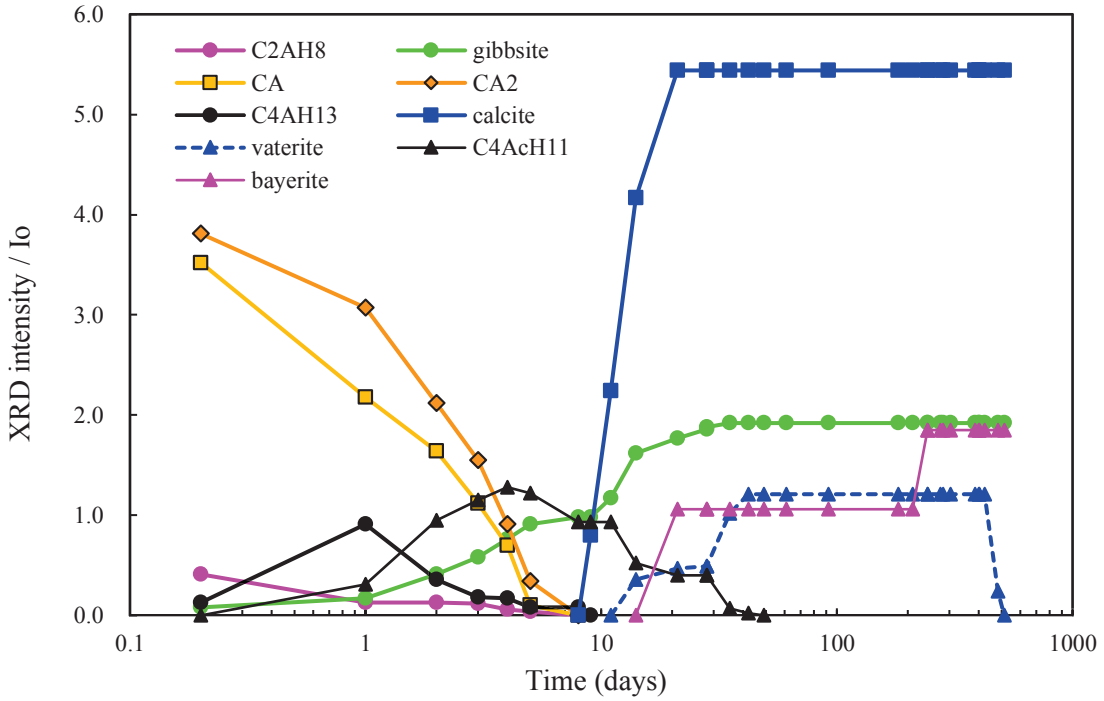

Figure 20. The XRD intensity ratios of different phases and their variations with curing time for the plate sample hft-30p.

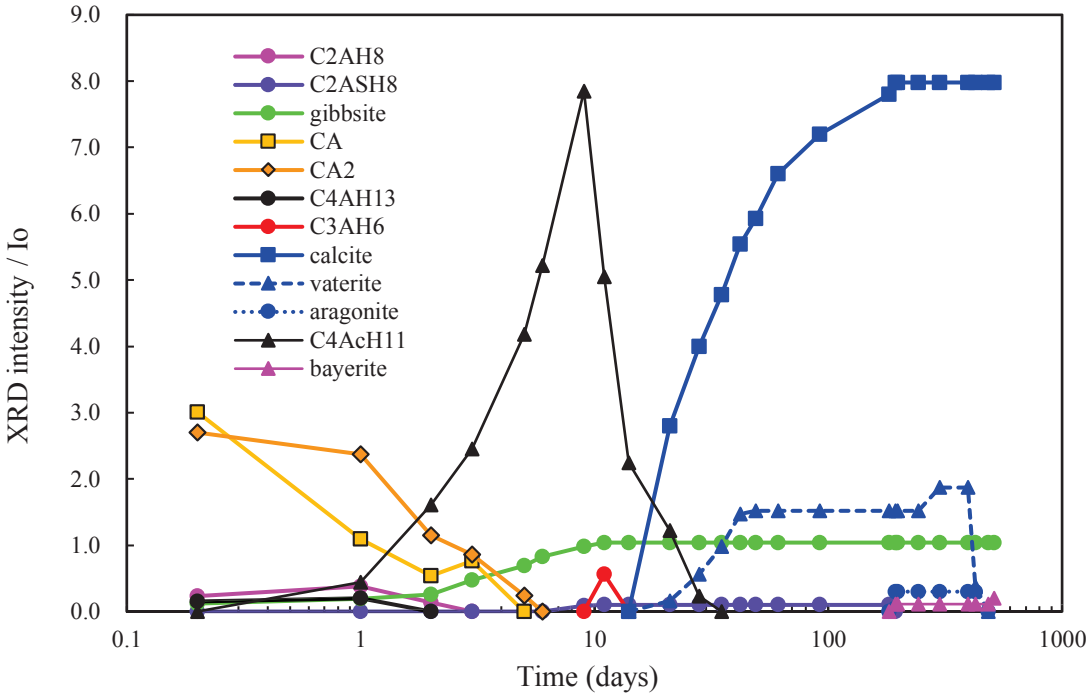

Figure 21. The XRD intensity ratios of different phases and their variations with curing time for the plate sample hf-30p.

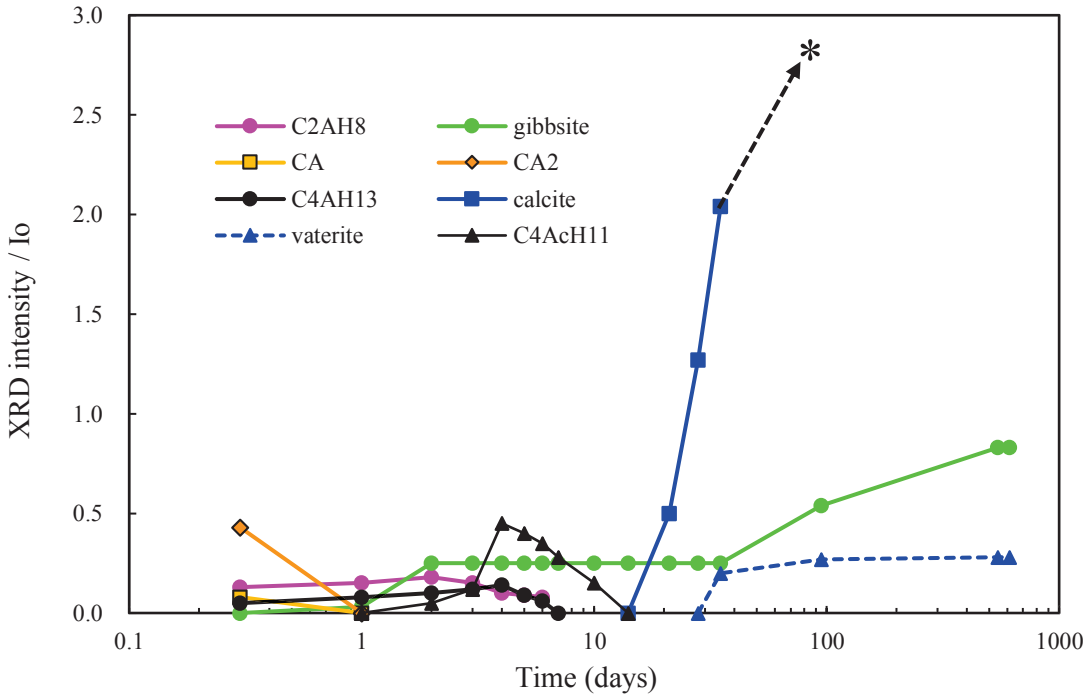

Figure 22. The XRD intensity ratios of different phases and their variations with curing time for the plate sample hft-35p. * represents a point after 95 days for calcite when intensity ratio increased to 3.19 beyond the present plotted area.

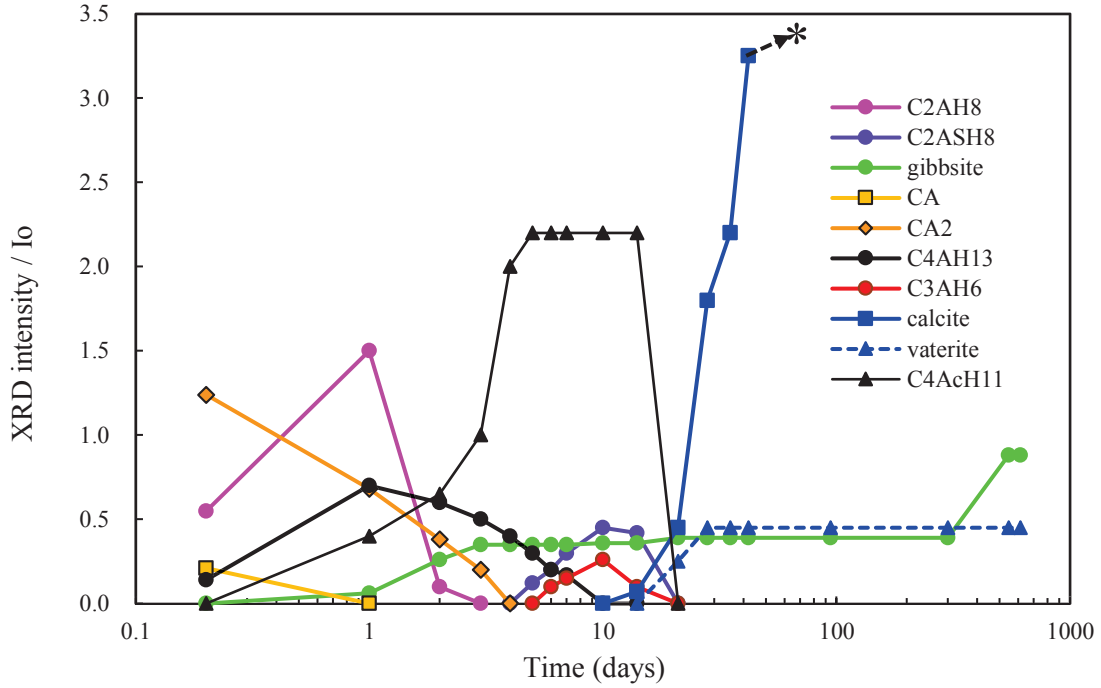

Figure 23. The XRD intensity ratios of different phases and their variations with curing time for the plate sample hf-35p. * represents a point after 94 days for calcite when intensity ratio increased to 3.81 beyond the extent of the present plot area.

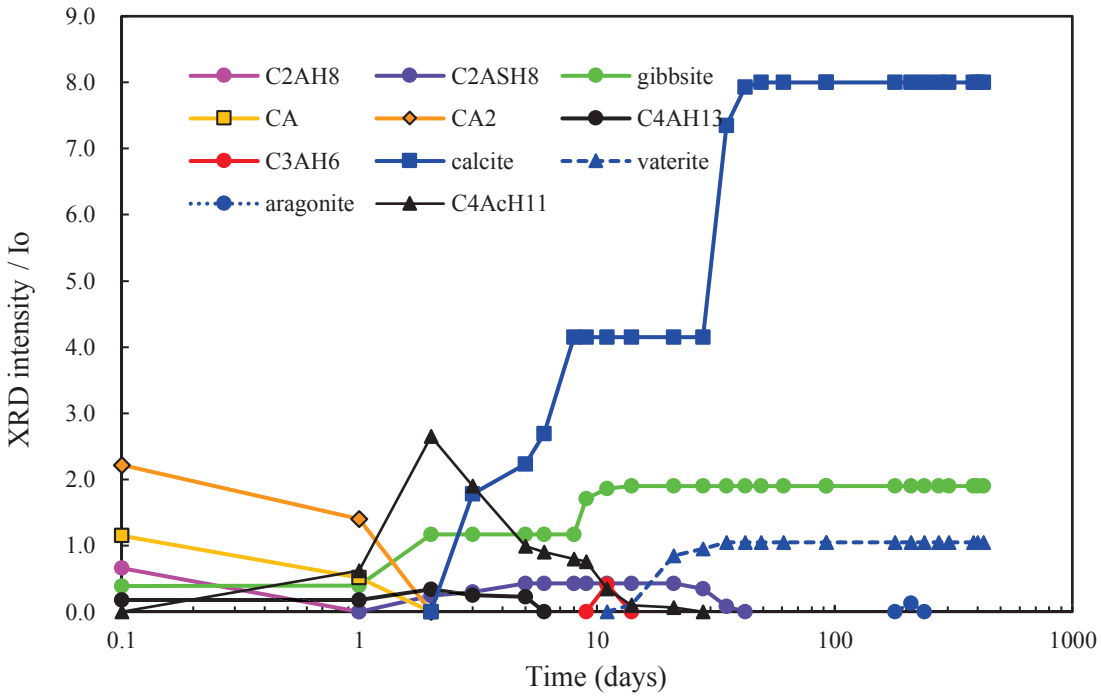

Figure 24. The XRD intensity ratios of different phases and their variations with curing time for the plate sample hft-50p.

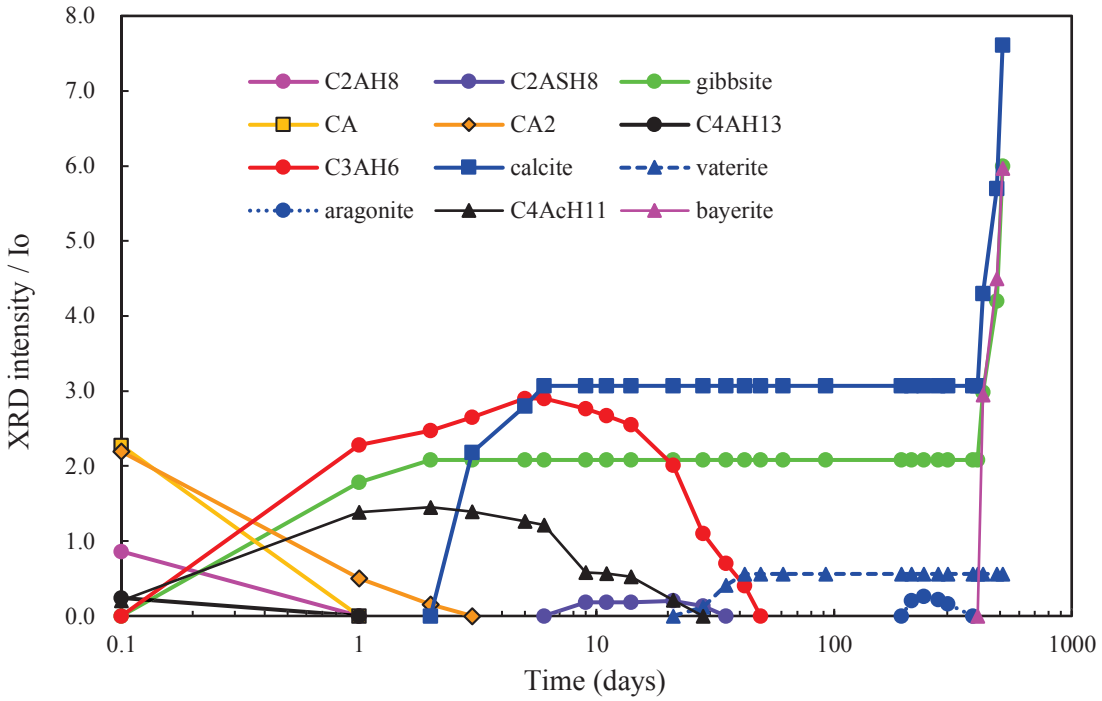

Figure 25. The XRD intensity ratios of different phases and their variations with curing time for the plate sample hf-50p.

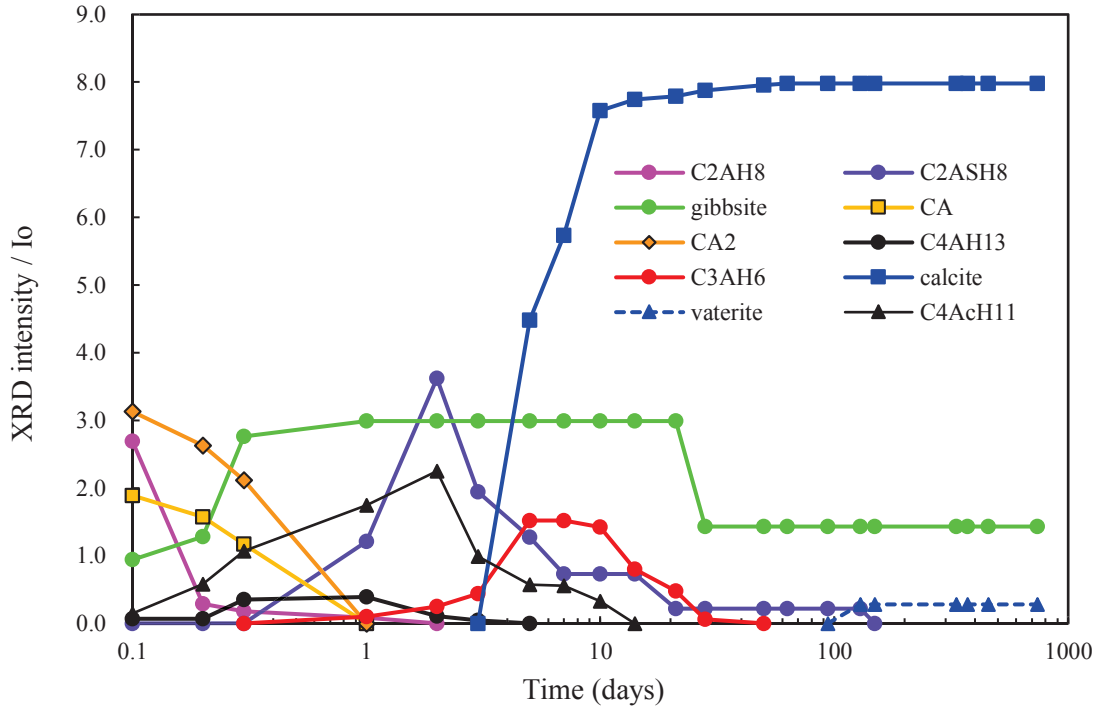

Figure 26. The XRD intensity ratios of different phases and their variations with curing time for the plate sample hft-60p.

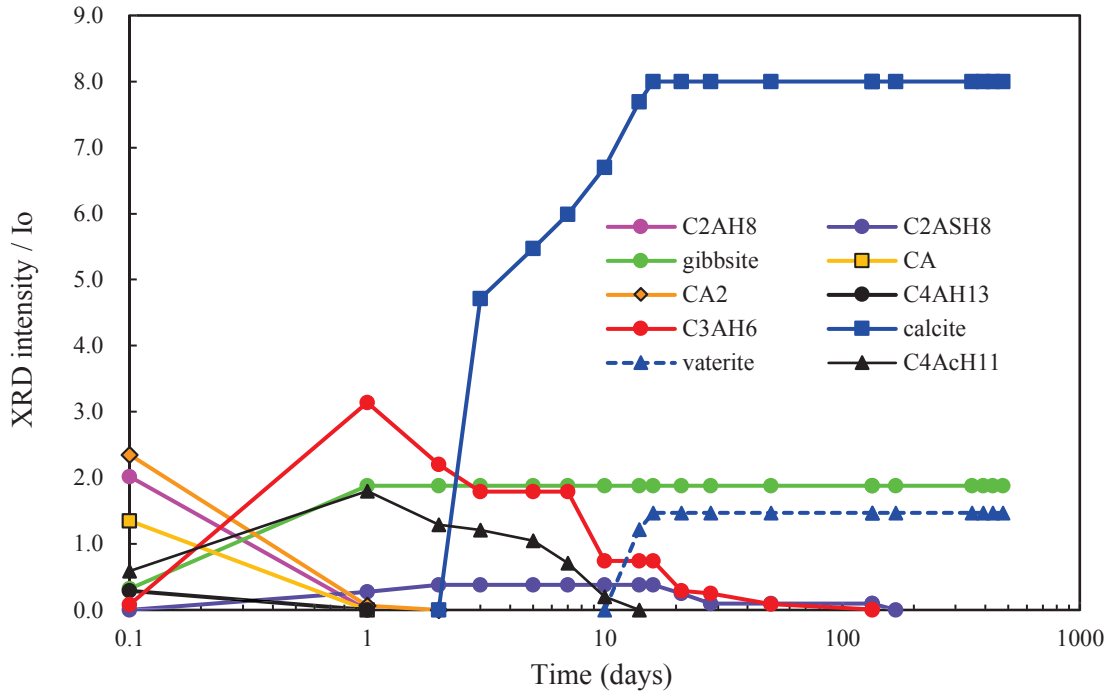

Figure 27. The XRD intensity ratios of different phases and their variations with curing time for the plate sample hf-60p.

Curing time(h)	6	12	18	24	30
hft-10bottle					
hf-10bottle					
hft-21bottle			unconfirmed		
hf-21bottle					

Figure 28. Crystallization times of the CAH_{10} hydrate. Starting points of the arrows indicate the initiation of crystallization of CAH_{10} as confirmed by XRD.

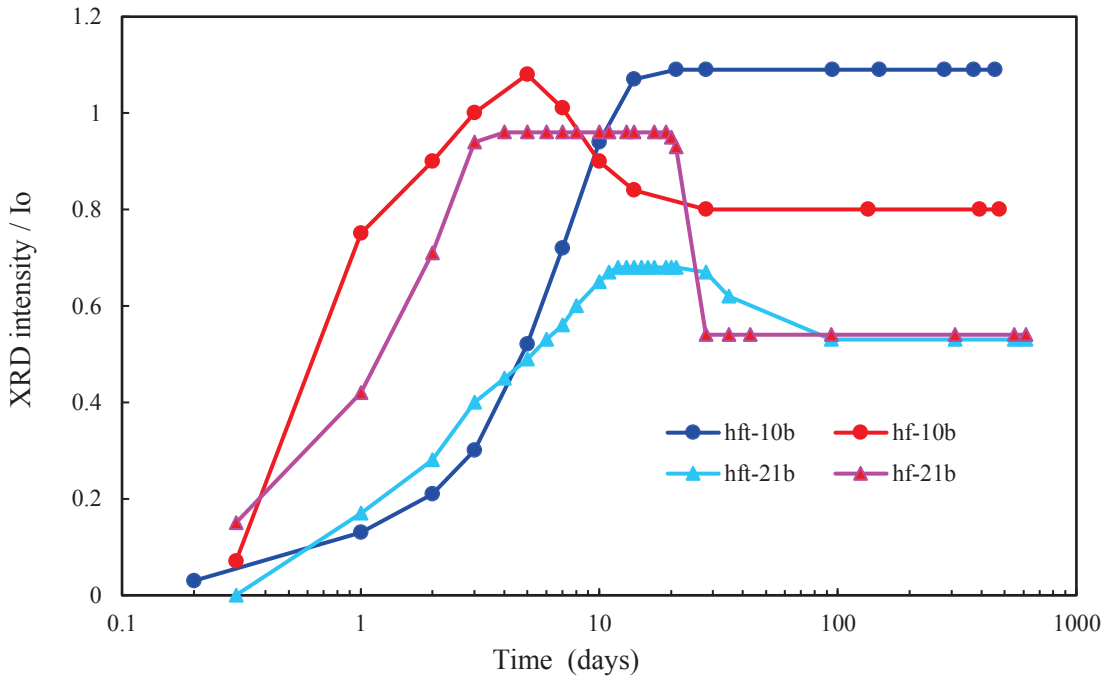

Figure 29. The XRD intensity of long term curing on the CAH_{10} hydrates at 10 °C and 21 °C. Both hft-10b and hf-10b samples are cured at 10 °C, while hft-21b and hf-21b are cured at 21 °C.

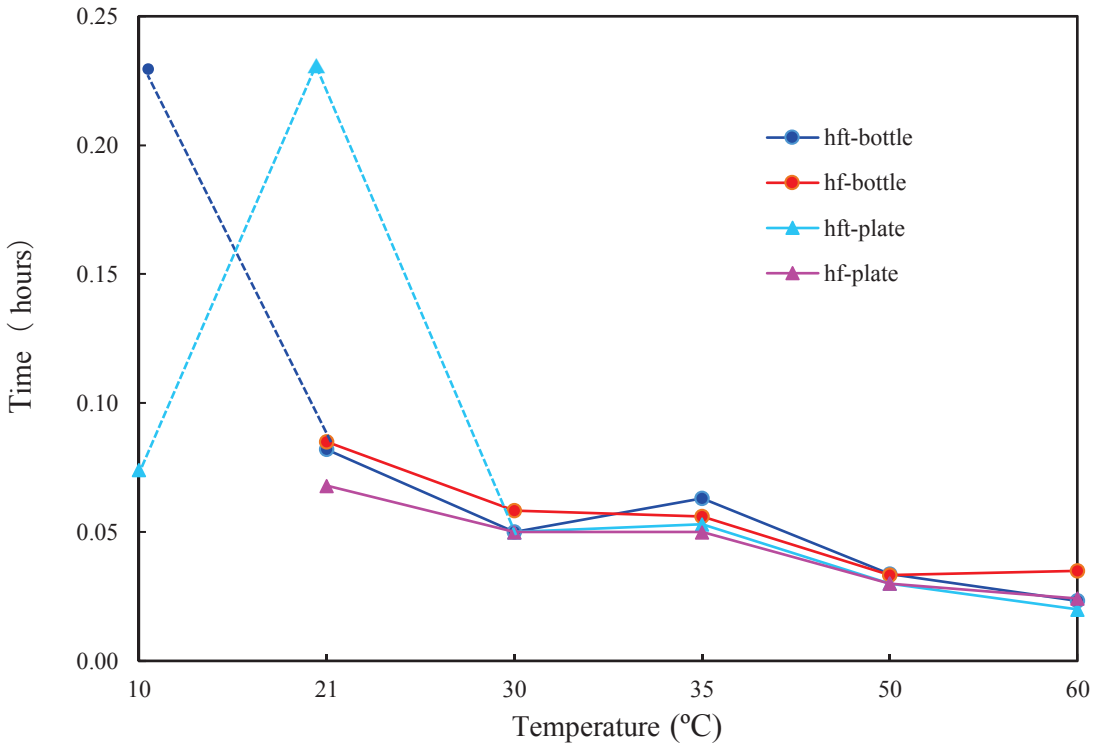

Figure 30. The initiation of crystallization as confirmed by XRD of the C_2AH_8 hydrates. Dotted lines are speculative segments of the hft-plate and hft-bottle samples.

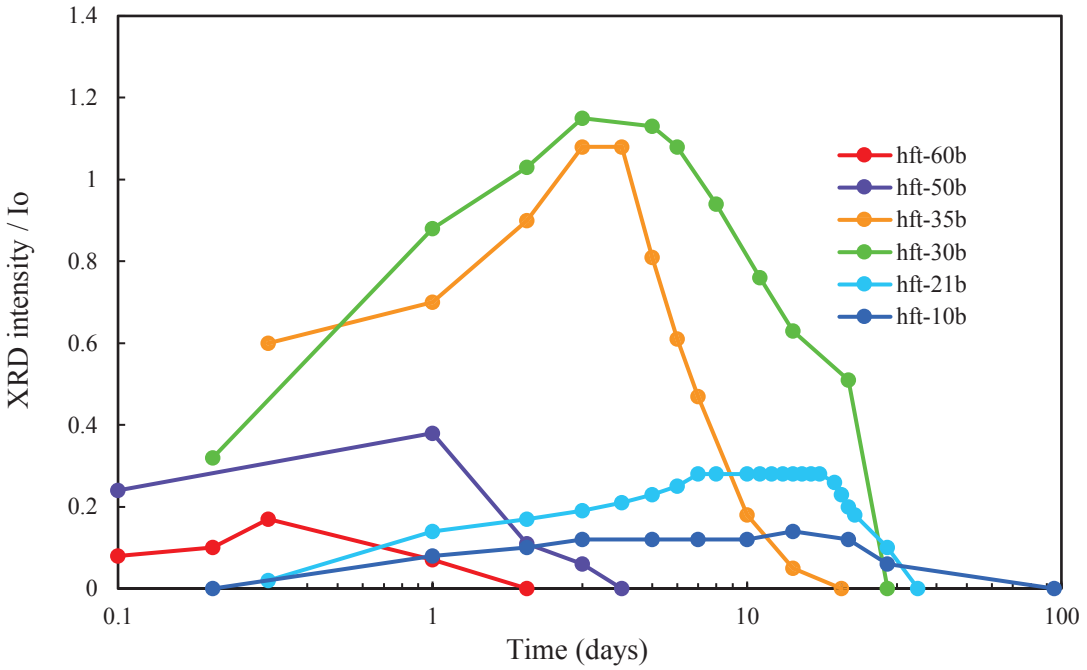

Figure 31. The curing time vs. the XRD intensity ratios of the C_2AH_8 hydrates of the hft bottle samples at different temperatures.

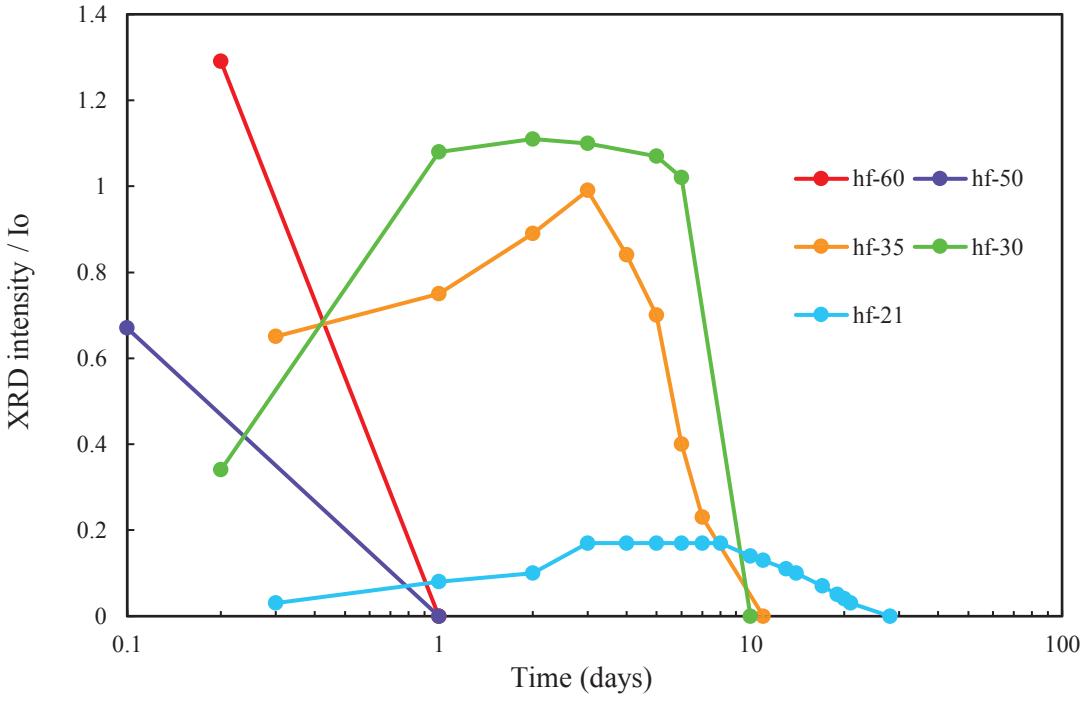

Figure 32. The curing time vs. the XRD intensity on the C_2AH_8 hydrates of the hf bottle samples at different temperatures.

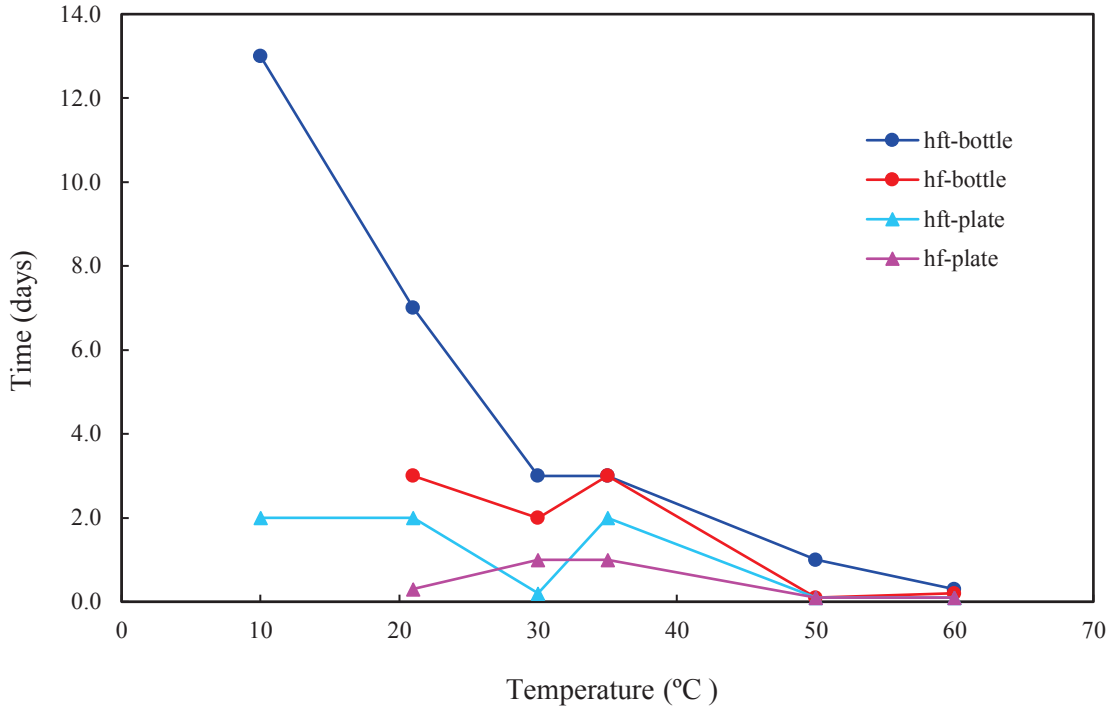

Figure 33. The time required to reach the maximum XRD intensities of the C_2AH_8 hydrates for bottle and plate samples with and without TPP.

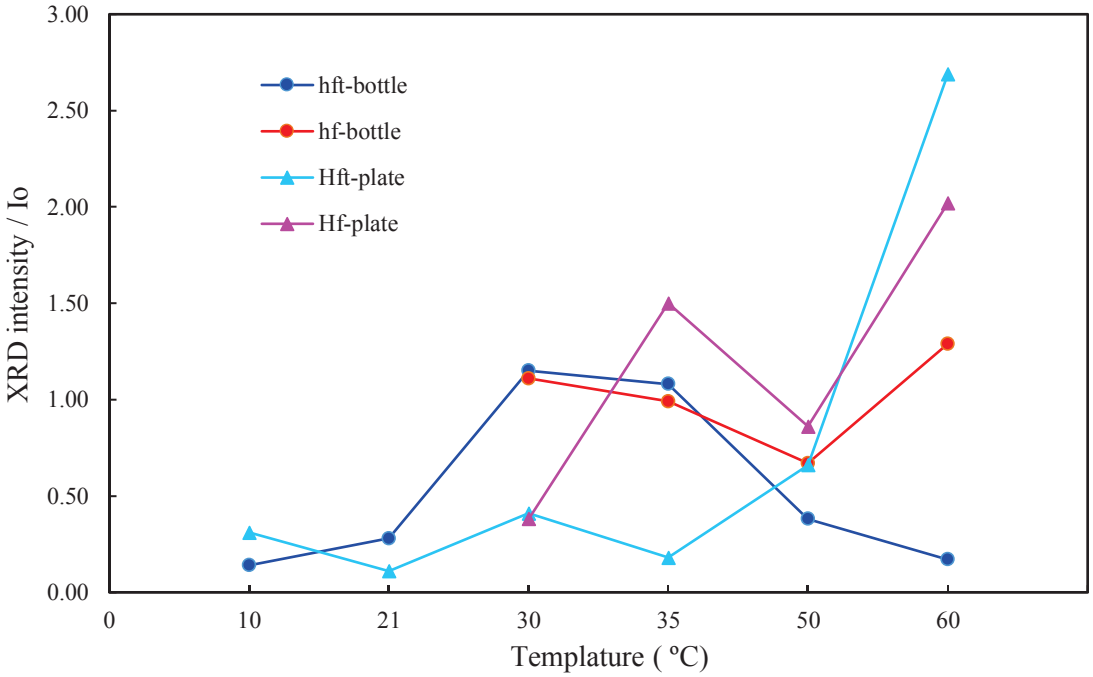

Figure 34. The maximum XRD intensities of the C_2AH_8 hydrates crystallized at different temperatures for both bottle and plate samples.

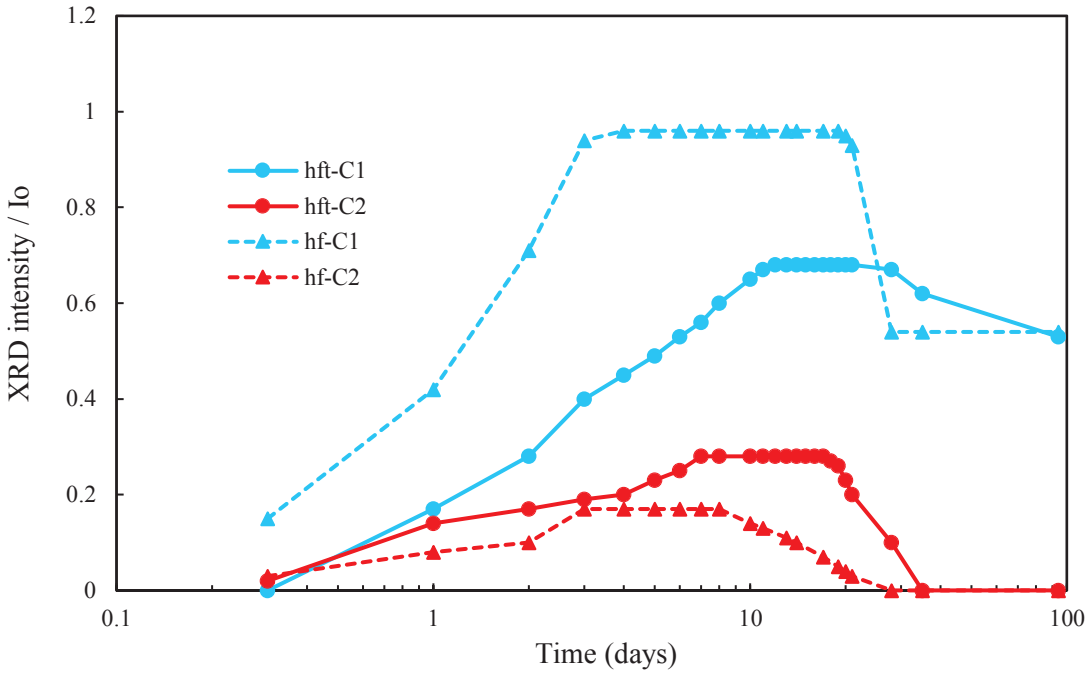

Figure 35. Relationship between XRD intensities and the hydration time for the CAH_{10} hydrates and the C_2AH_8 hydrates at 21 °C curing. hft-C1 is CAH_{10} hydrates of hft-bottle at 21 °C curing and hf-C1 is CAH_{10} hydrates of hf-bottle at 21 °C curing. hft-C2 is C_2AH_8 hydrates of hft-bottle at 21 °C curing and hf-C2 is C_2AH_8 hydrates of hf-bottle at 21 °C curing.

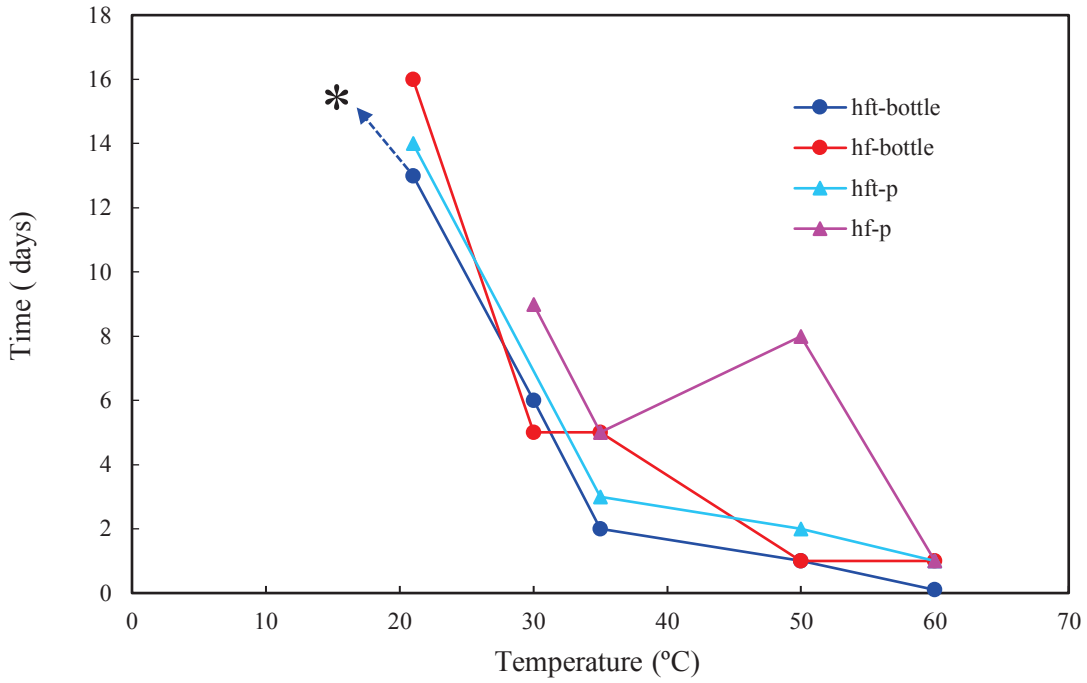

Figure 36. The crystallization time of the stratlingite as confirmed by XRD. * represents a longer duration of 149 days at 10 ºC for hft-bottle sample, which is beyond the present plot area.

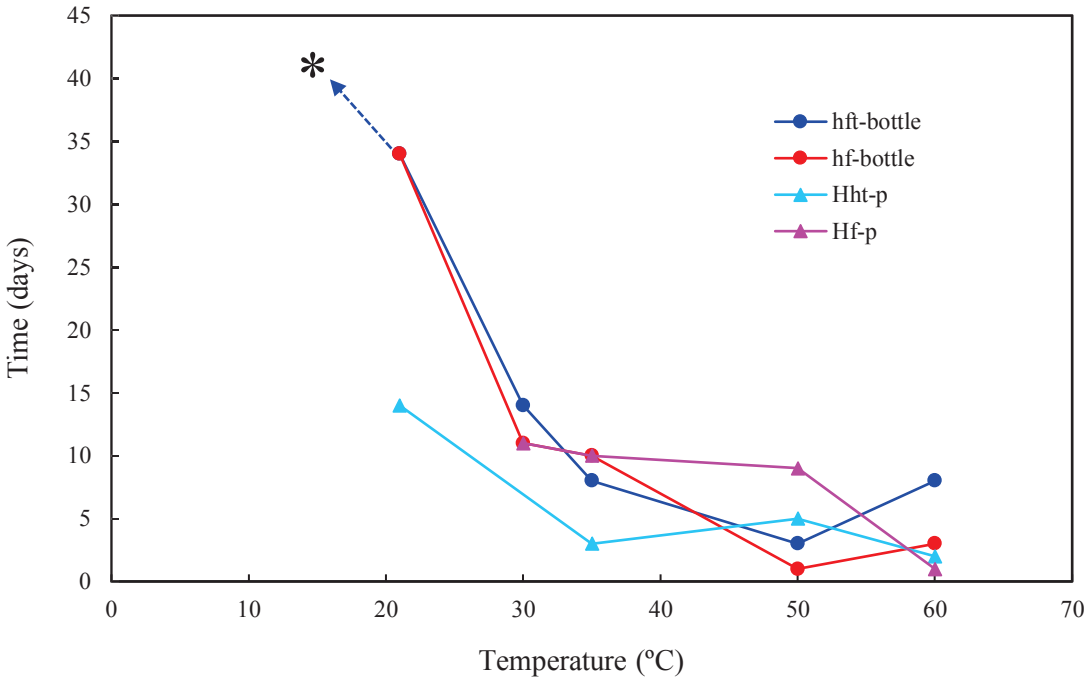

Figure 37. The time required to reach the maximum XRD intensities of the stratlingite at different temperatures for types of samples. * represents a longer duration of 149 days at 10 ºC, which is beyond the present plot area.

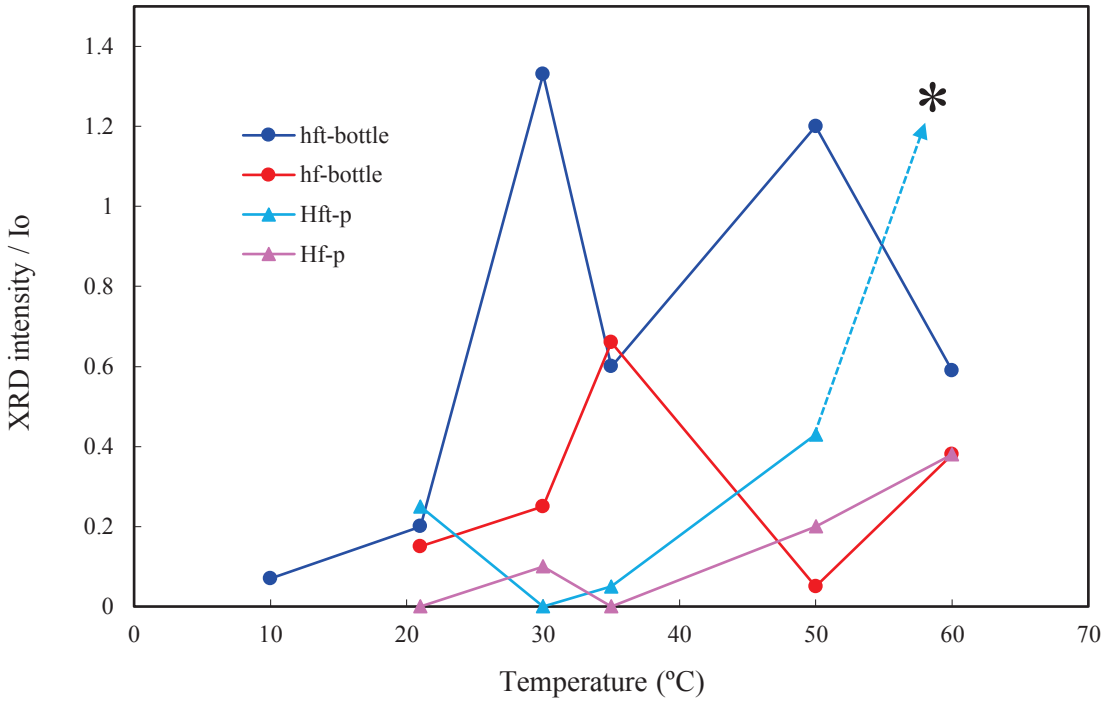

Figure 38. The maximum XRD intensities of the stratlingite at different temperatures. * represents a point of loner duration of 62 days for hft-plate sample at 60 ºC.

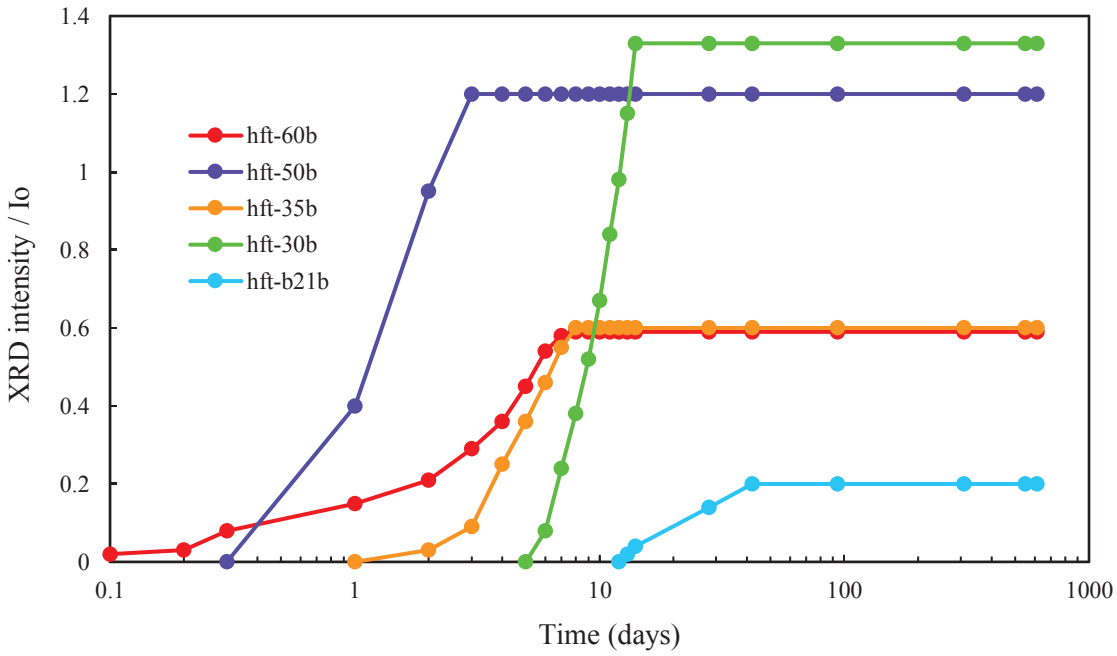

Figure 39. The XRD intensities of the stratlingite of the hft-bottles and their variation with the hydration times.

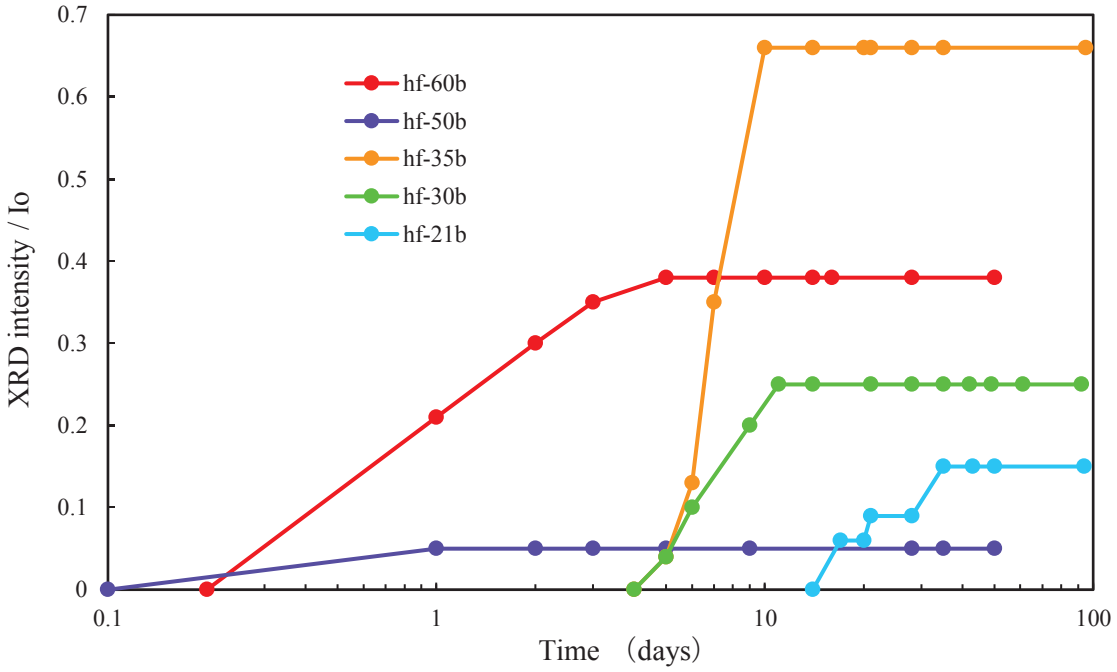

Figure 40. The variation of XRD intensities of the stratlingite of the hf-bottle samples with their curing times.

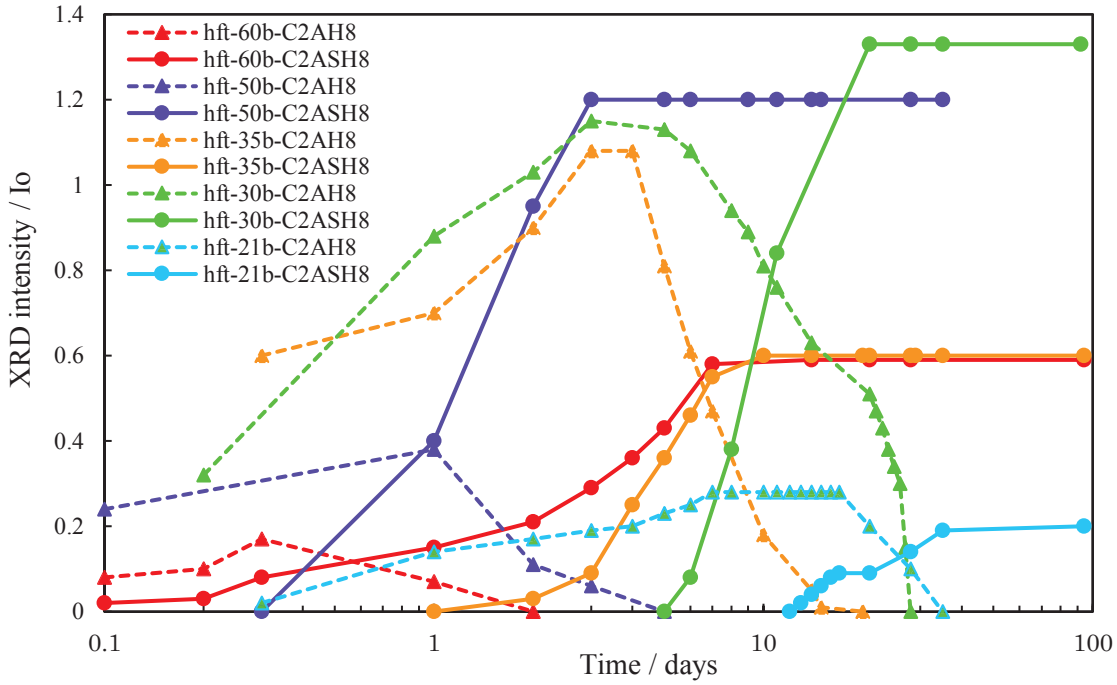

Figure 41. The relative change in XRD intensities of the C_2ASH_8 and the C_2AH_8 hydrates in the hft-bottle samples with respect to hydration times.

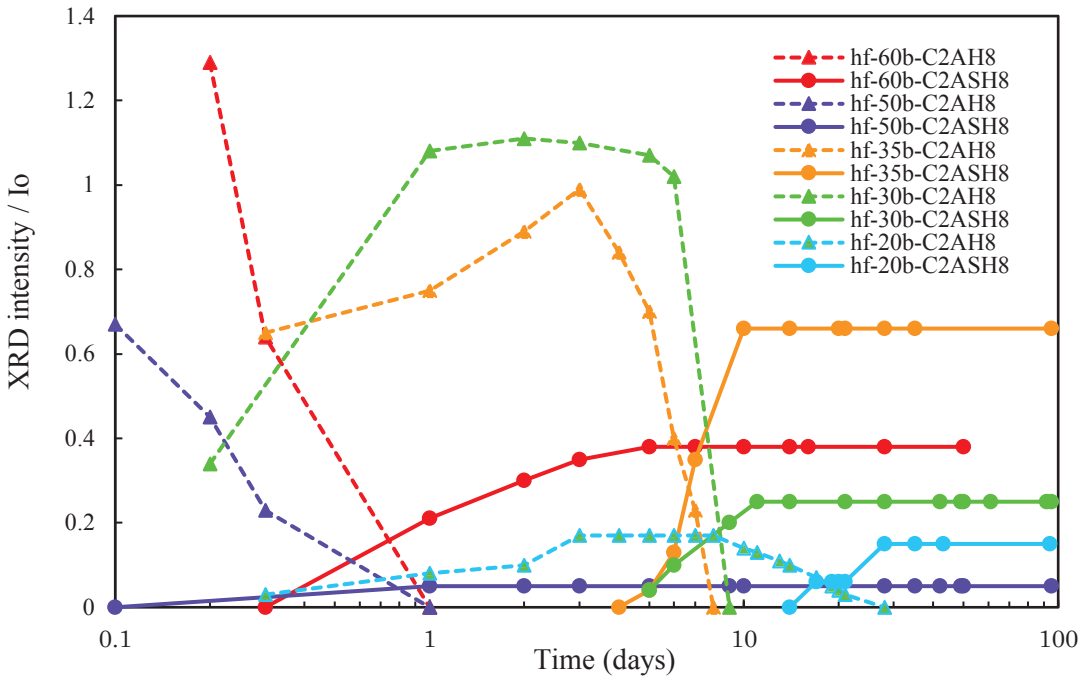

Figure 42. The relative change in XRD intensities of the C_2ASH_8 and the C_2AH_8 hydrates in the hf-bottle samples with respect to hydration times.

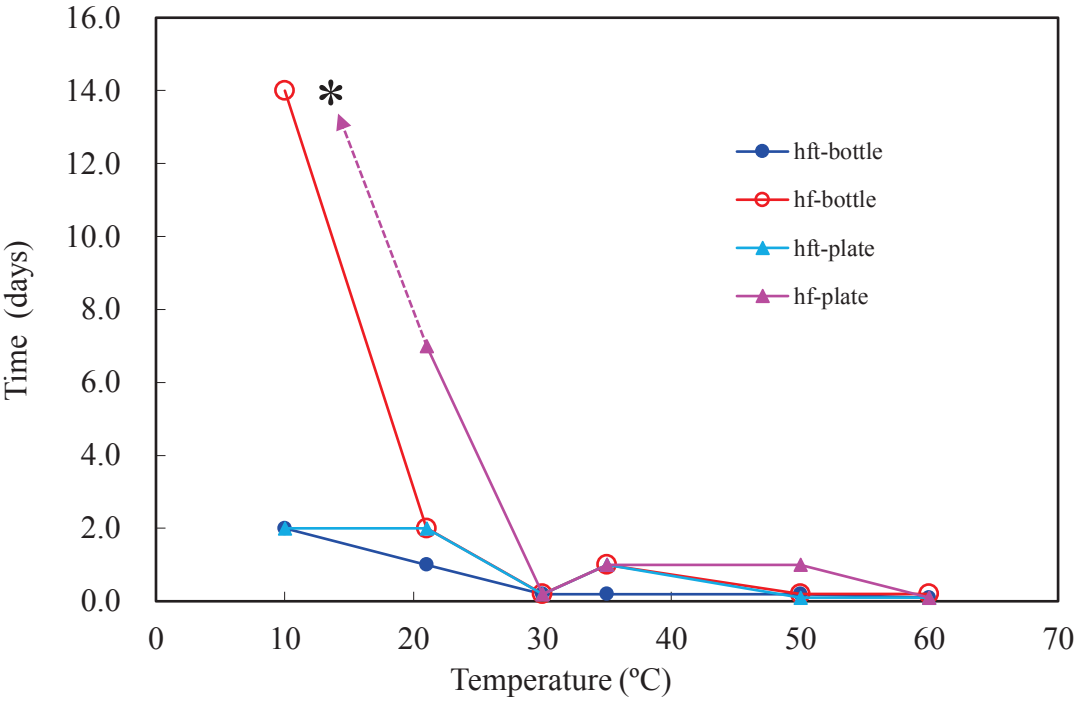

Figure 43. The crystallization time, as confirmed by XRD of the gibbsite in the hft-bottle and hf-bottle samples. * represents a long duration of 759 days at 10 ºC, which is beyond the present plot area.

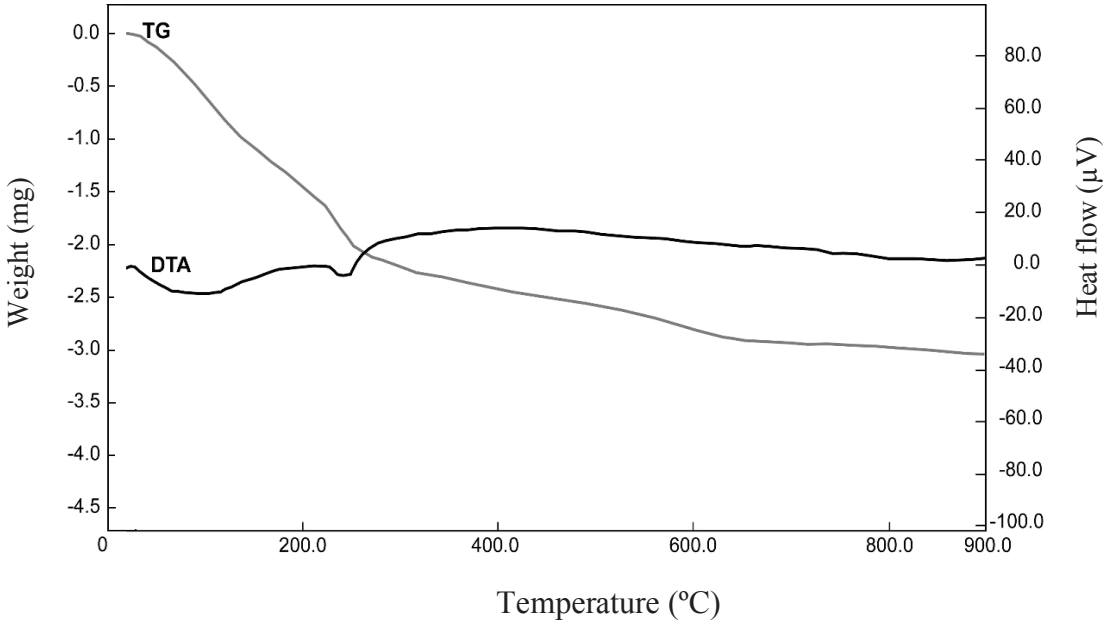

Figure 44. Results of TG-DTA on the crystal-rich portion in the hydrated HACd+SF4.

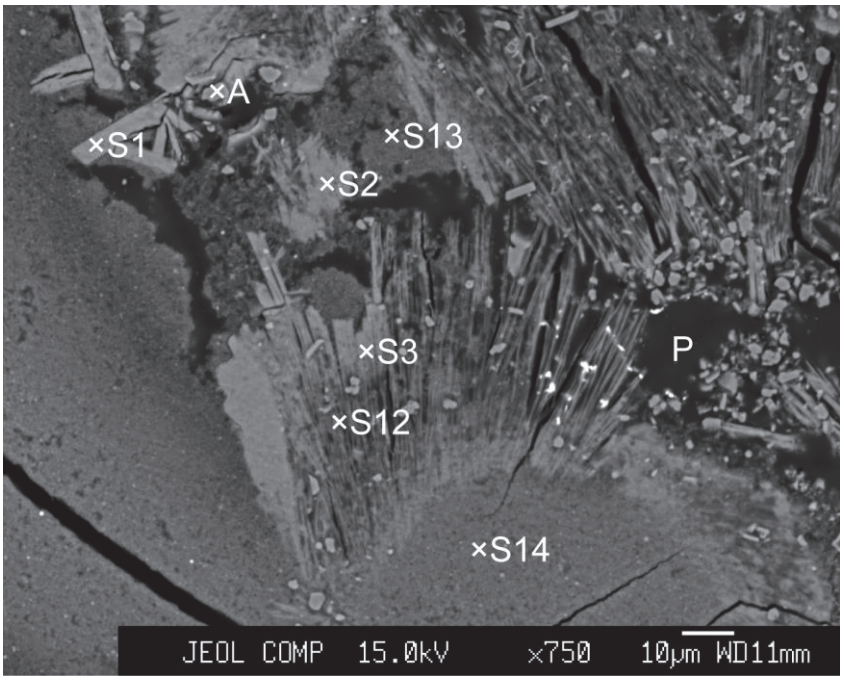

Figure 45. Backscattered electron photomicrograph hydrated HACd+SF4. S1 to S3: Hydrated products; S13 and 14: Cohesion of FS; P: Pore; A: Al_2O_3; numbers indicate analyzed points.

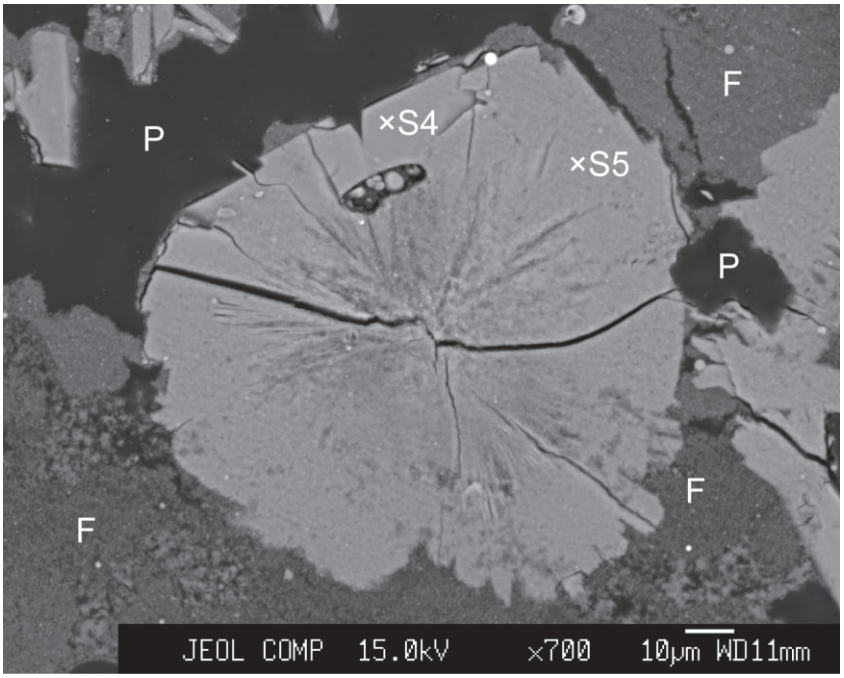

Figure 46. Backscattered electron photomicrograph of the hydrated HACd+SF4. 4 and S5: Hydrated products; F: Cohesion of SF; P: Pore. Numbers indicate analyzed points.

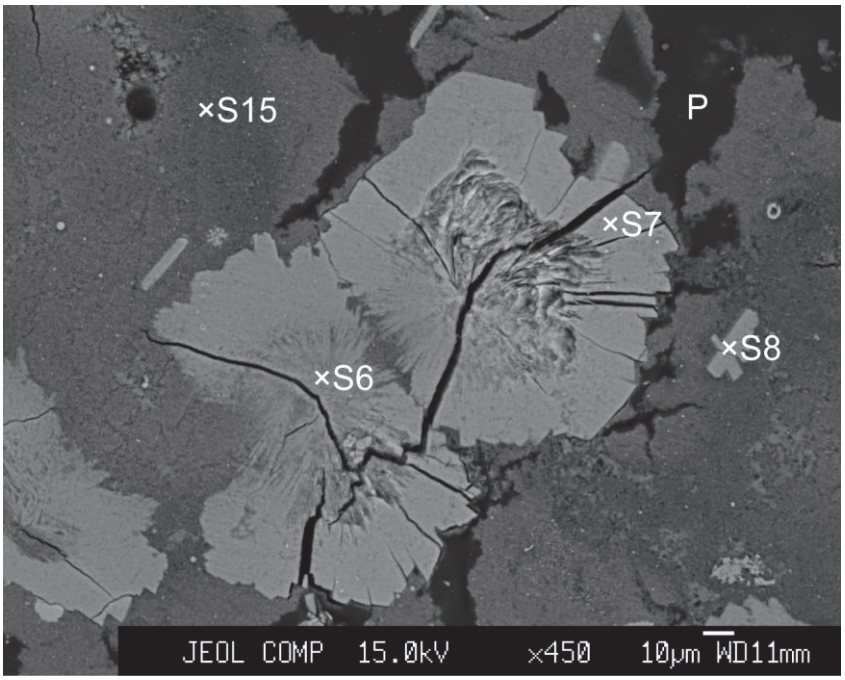

Figure 47. Backscattered electron photomicrograph of the hydrated HACd+SF. S6 to S8: Hydrated products; S15: Cohesion of SF; P: Pore. The numbers indicate analyzed points.

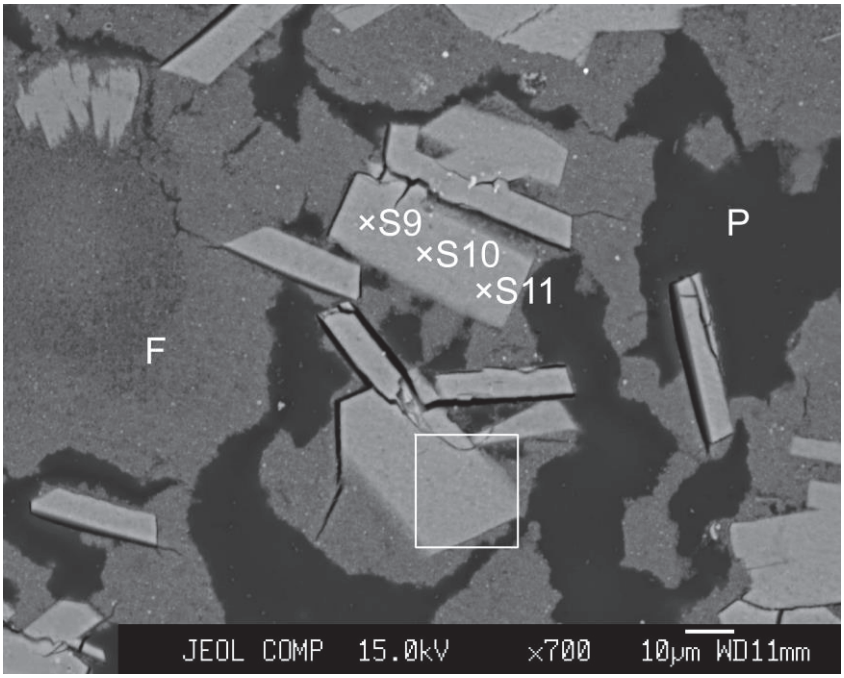

Figure 48. Backscattered electron photomicrograph of the hydrated HACd+SF4. S9 to S11: Hydrated products; F: Cohesion of SF; P: Pore. The numbers indicate analyzed points; White box is the chemically mapped area and the results is shown in plate 5.

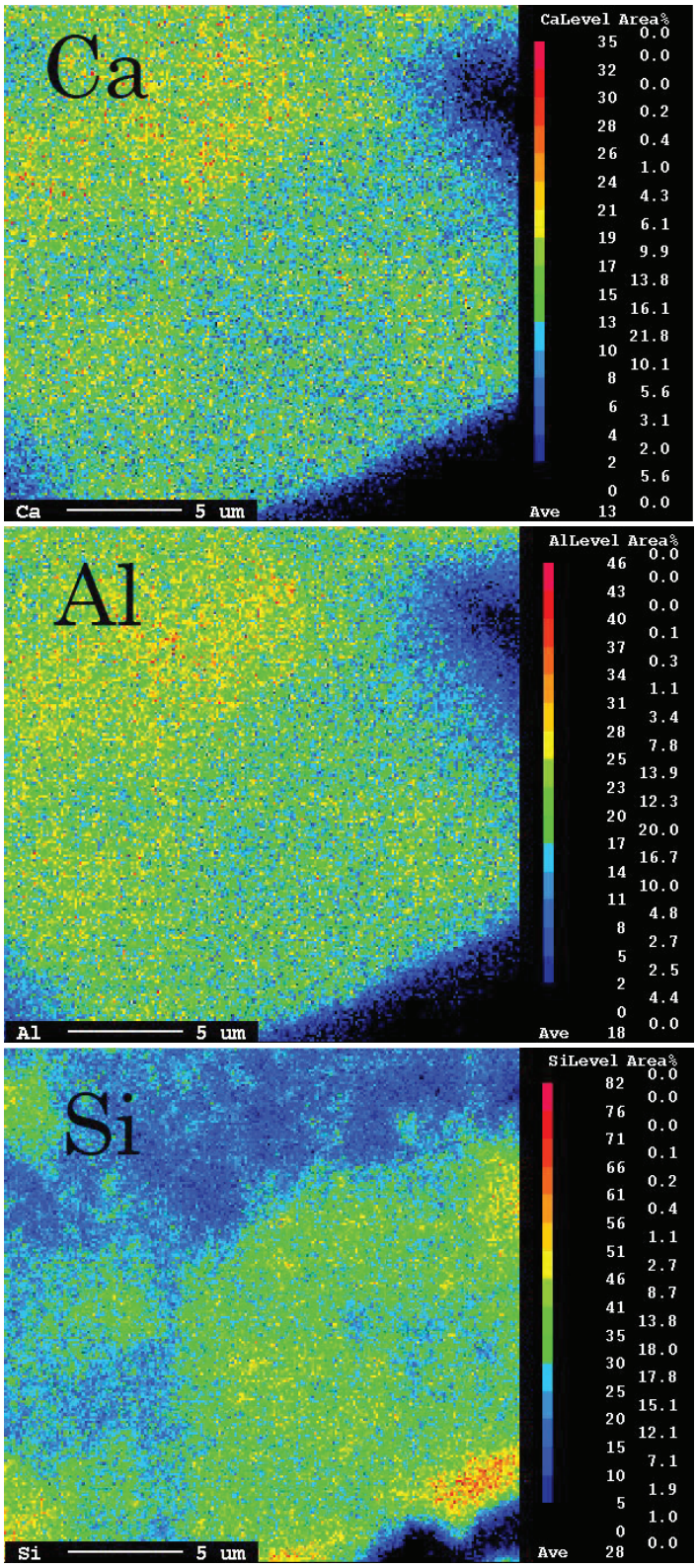

Figure 49. Chemical mapping (Ca, Al, Si) of the hydrated products. The mapped area is shown in figure 48.

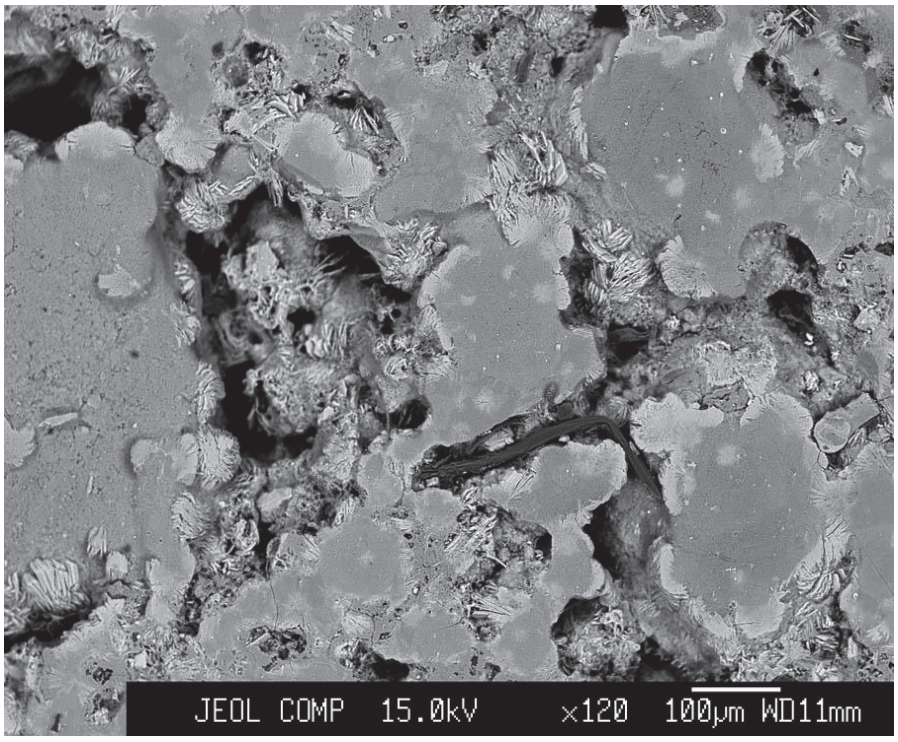

Figure 50. Backscattered electron photomicrograph of the sample hft-21b of the B-group.

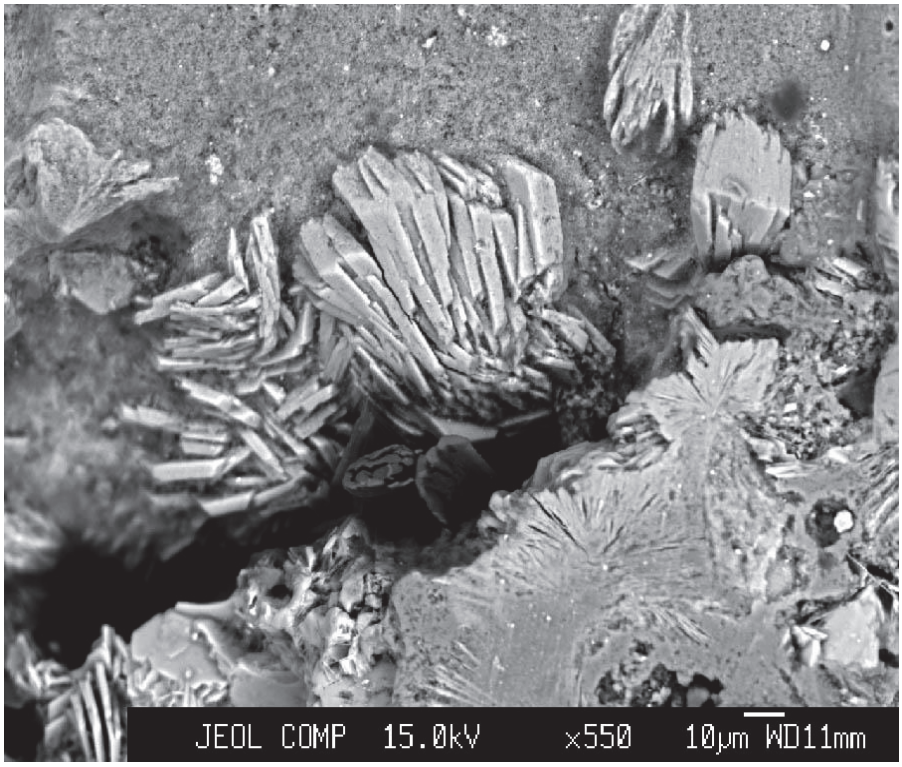

Figure 51. Backscattered electron photomicrograph of the sample hft-21b of the B-group.

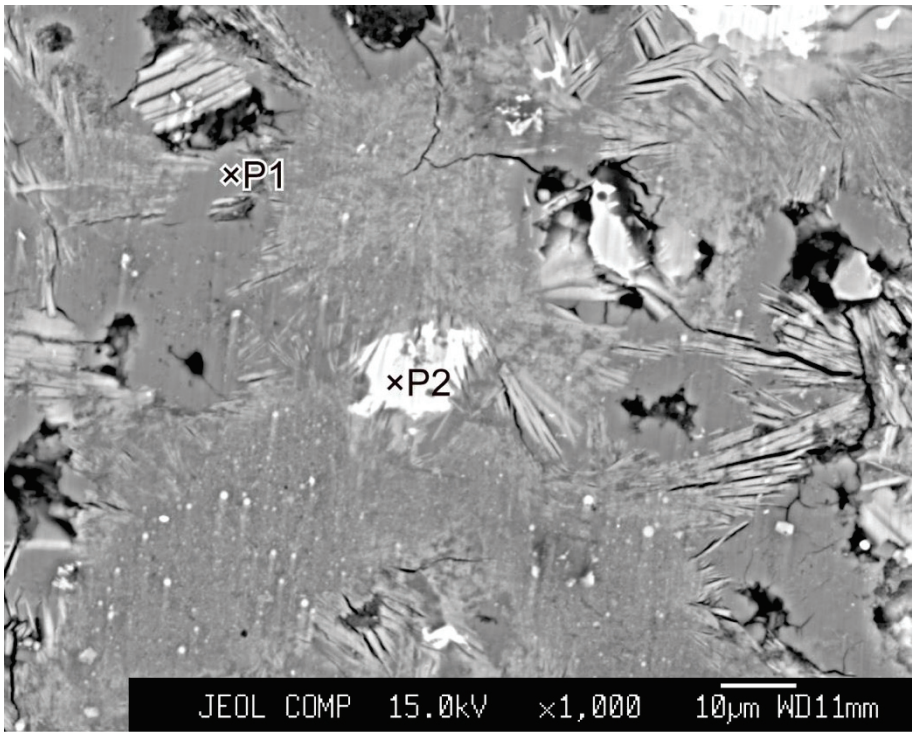

Figure 52. Backscattered electron photomicrograph of the sample hft-21b of the B-group. The numbers indicate analyzed points.

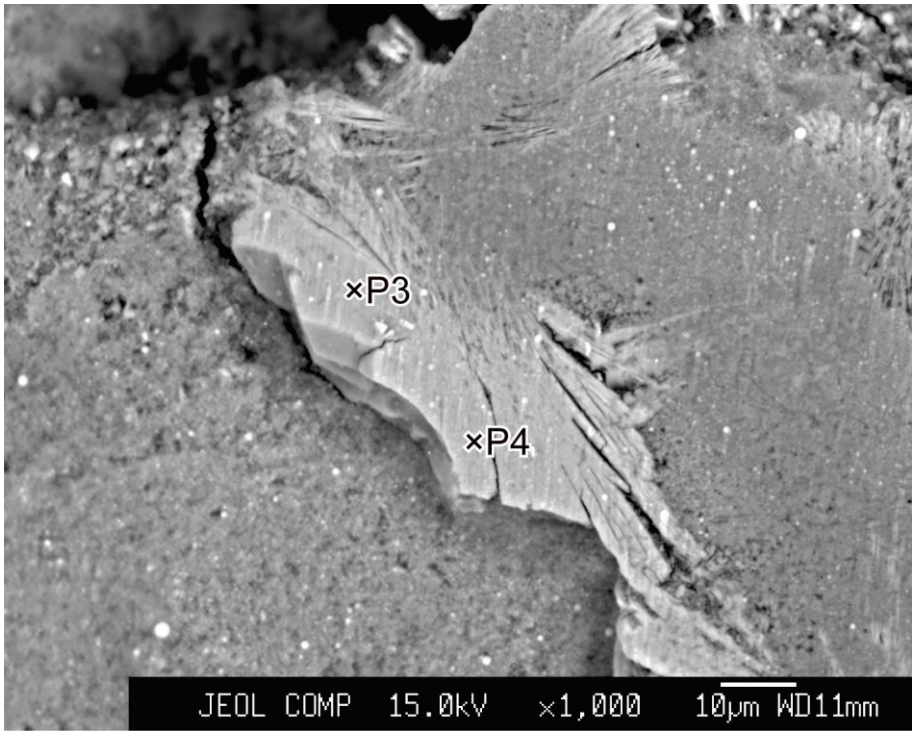

Figure 53. Backscattered electron photomicrograph of the sample hft-21b of the B-group. The numbers indicate analyzed points.

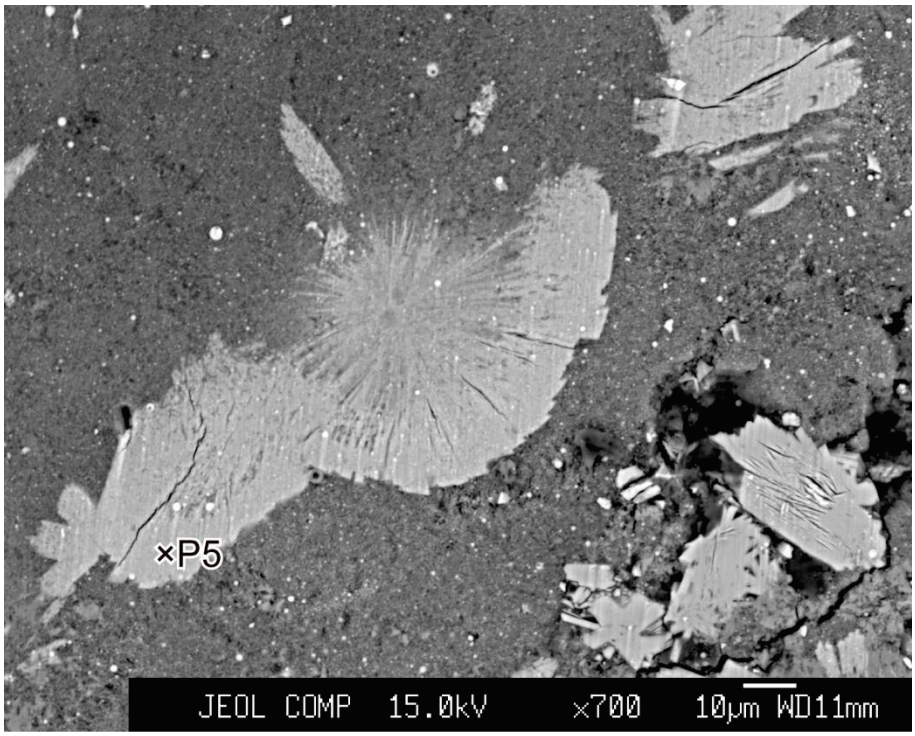

Figure 54. Backscattered electron photomicrograph of the sample hft-21b of the B-group. The number indicate analyzed point.

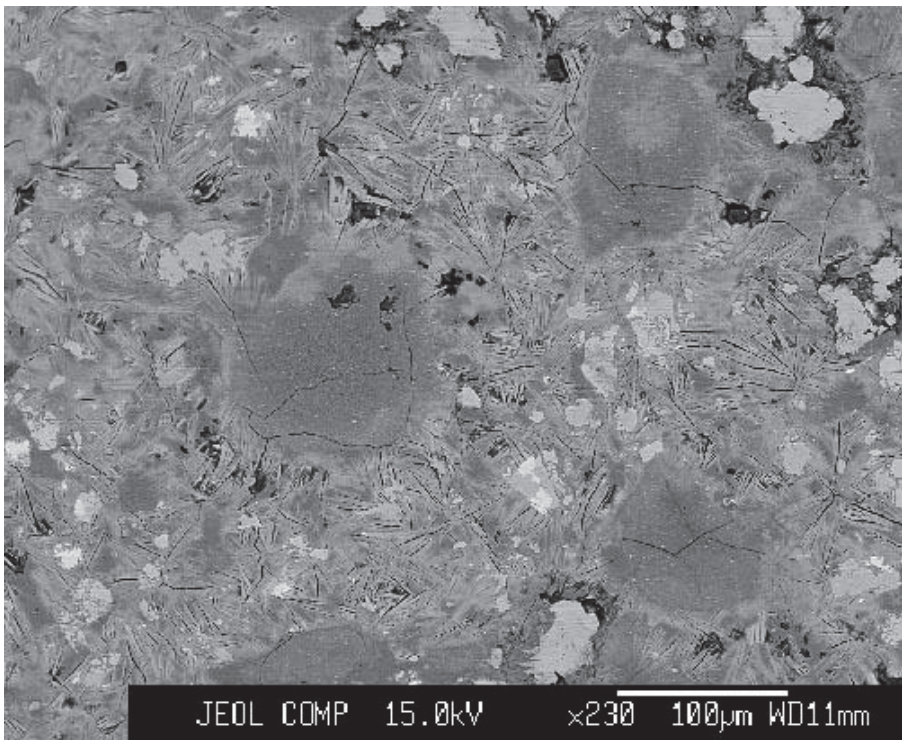

Figure 55. Backscattered electron photomicrograph of the sample hft-35b of the B-group.

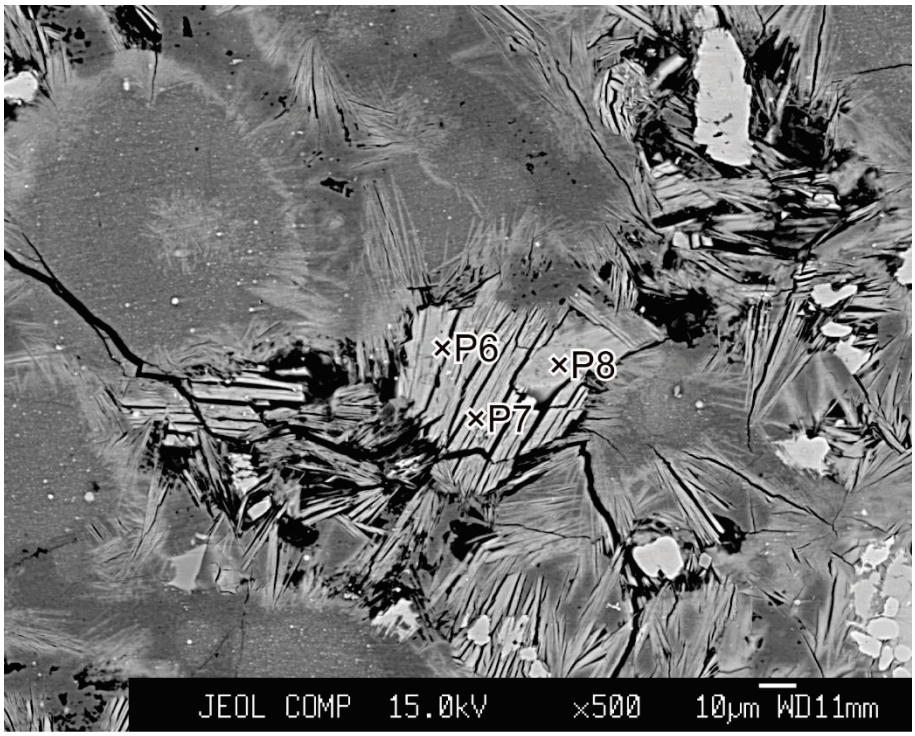

Figure 56. Backscattered electron photomicrograph of the sample hft-35b of the B-group. The numbers indicate analyzed points.

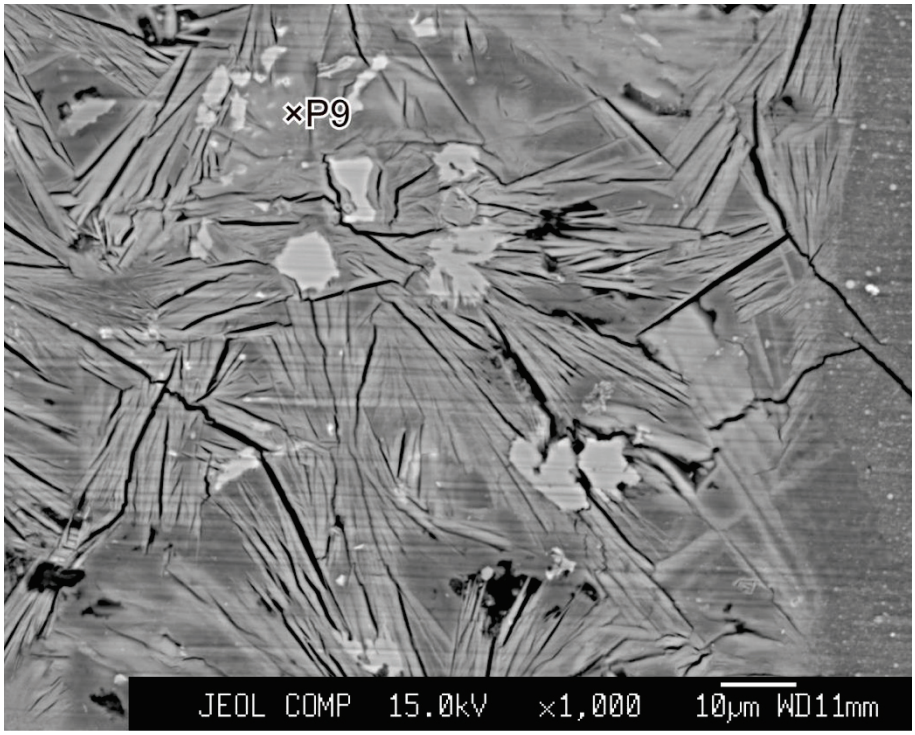

Figure 57. Backscattered electron photomicrograph of the sample hft-35b of the B-group. The number indicates analyzed point.

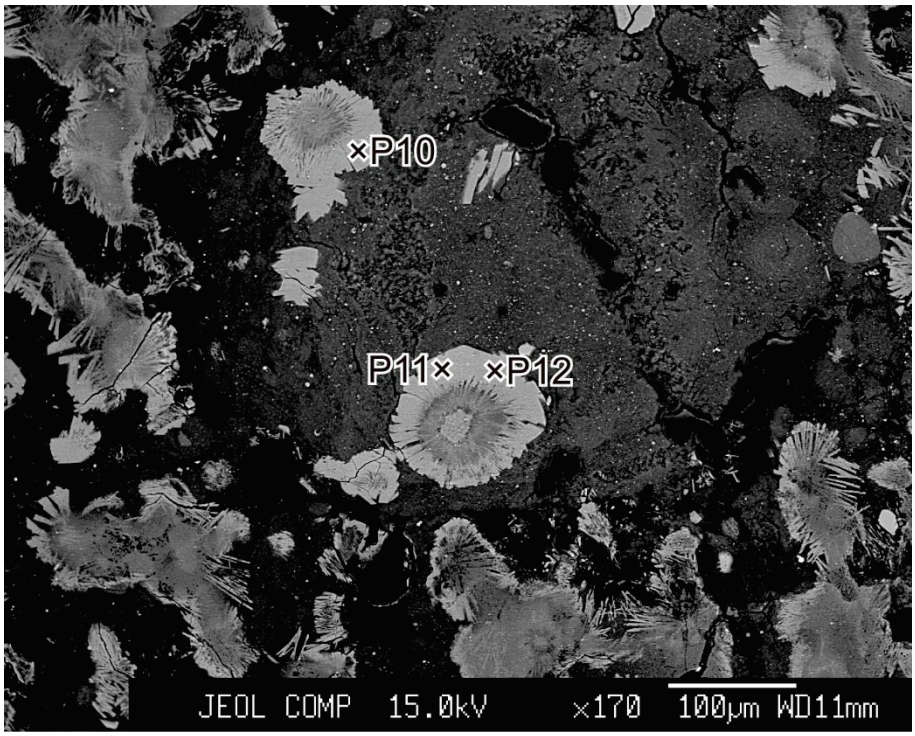

Figure 58. Backscattered electron photomicrograph of the sample hft-21b of the B-group. The numbers indicate analyzed points.

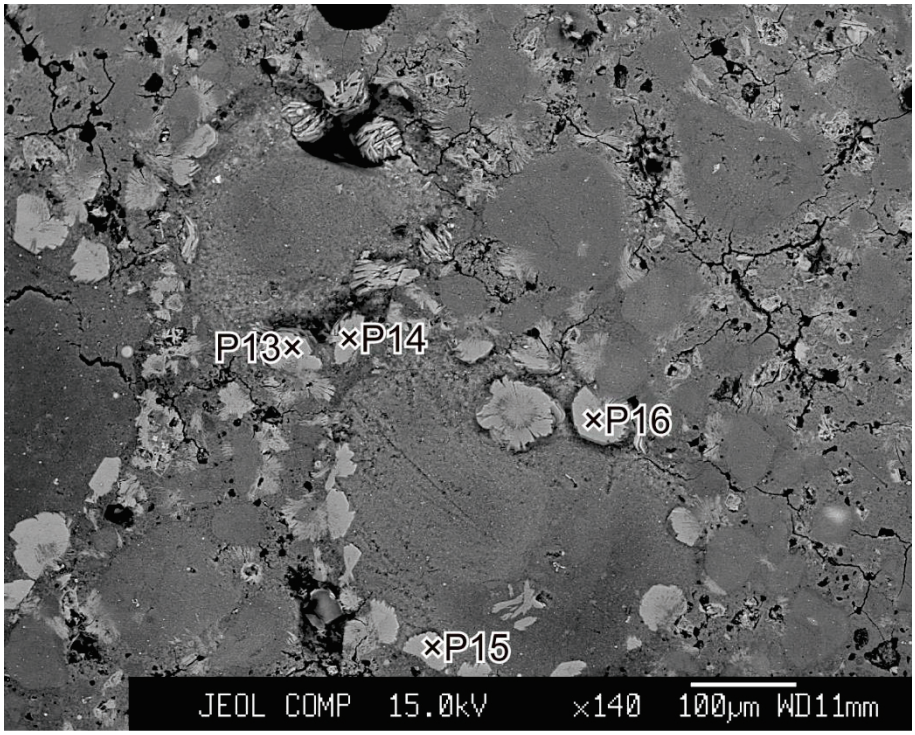

Figure 59. Backscattered electron photomicrograph of the sample hf-21b of the B-group. The numbers indicate analyzed points.

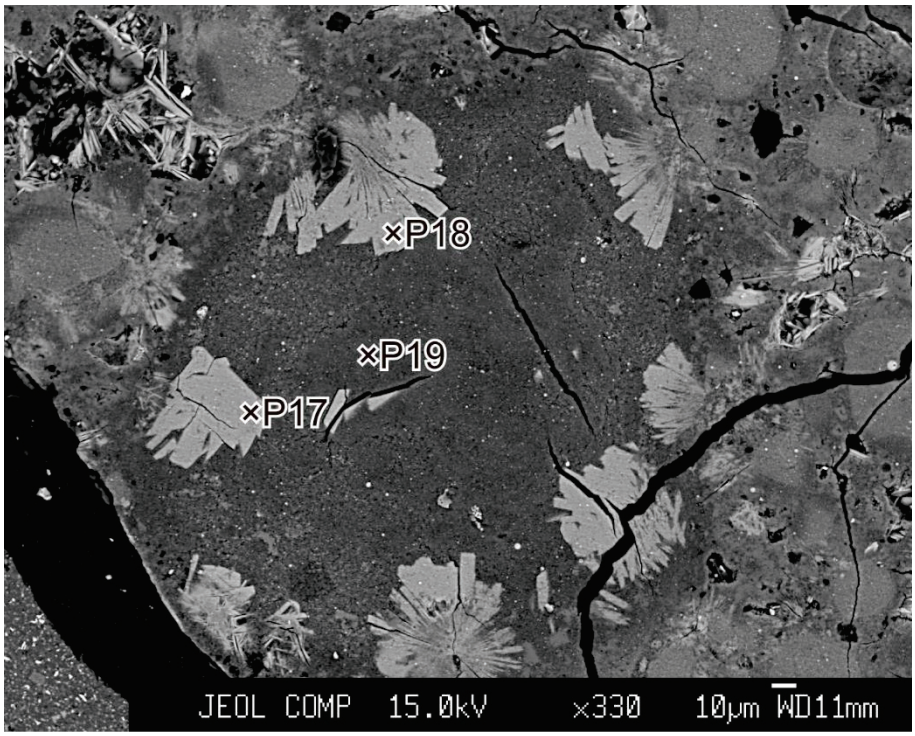

Figure 60. Backscattered electron photomicrograph of the sample hf-21b of the B-group. The numbers indicate analyzed points.

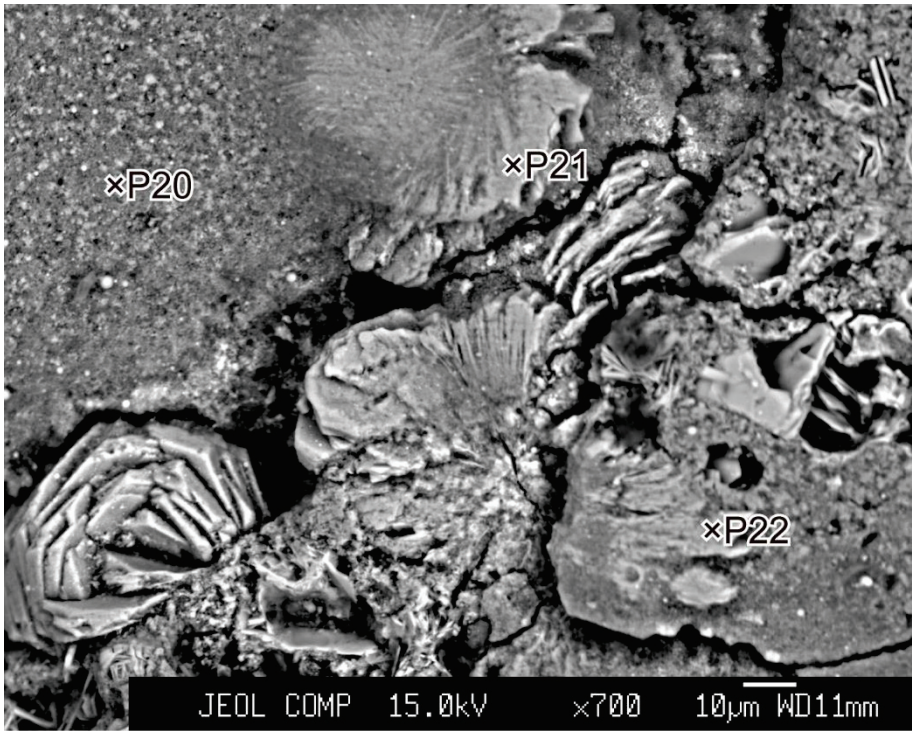

Figure 61. Backscattered electron photomicrograph of the sample hf-21b of the B-group. The numbers indicate analyzed points.

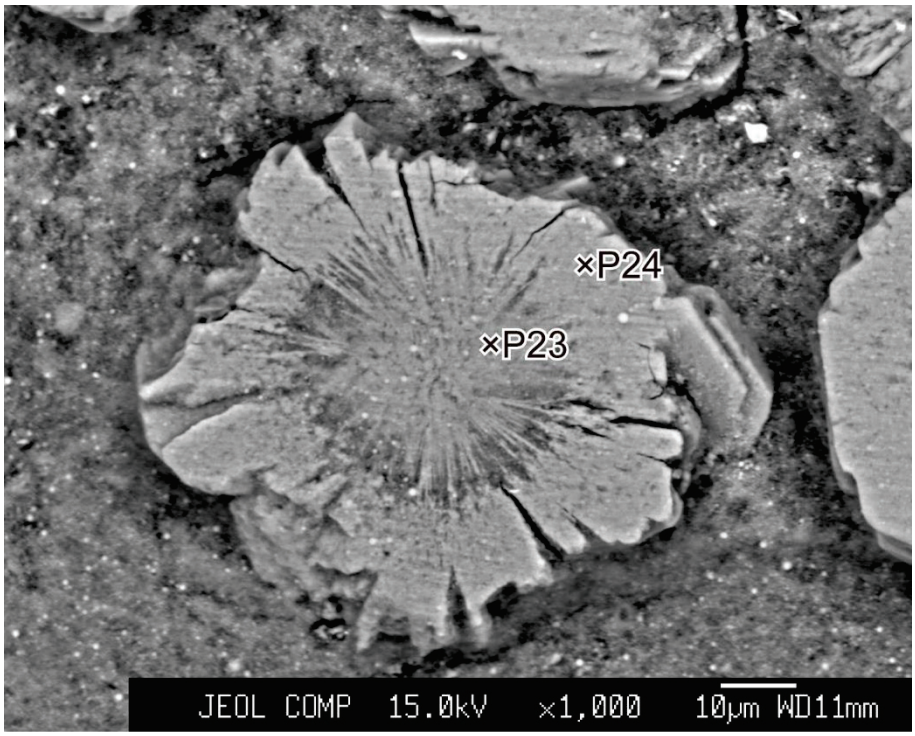

Figure 62. Backscattered electron photomicrograph of the sample hf-21b of the B-group. The numbers indicate analyzed points.

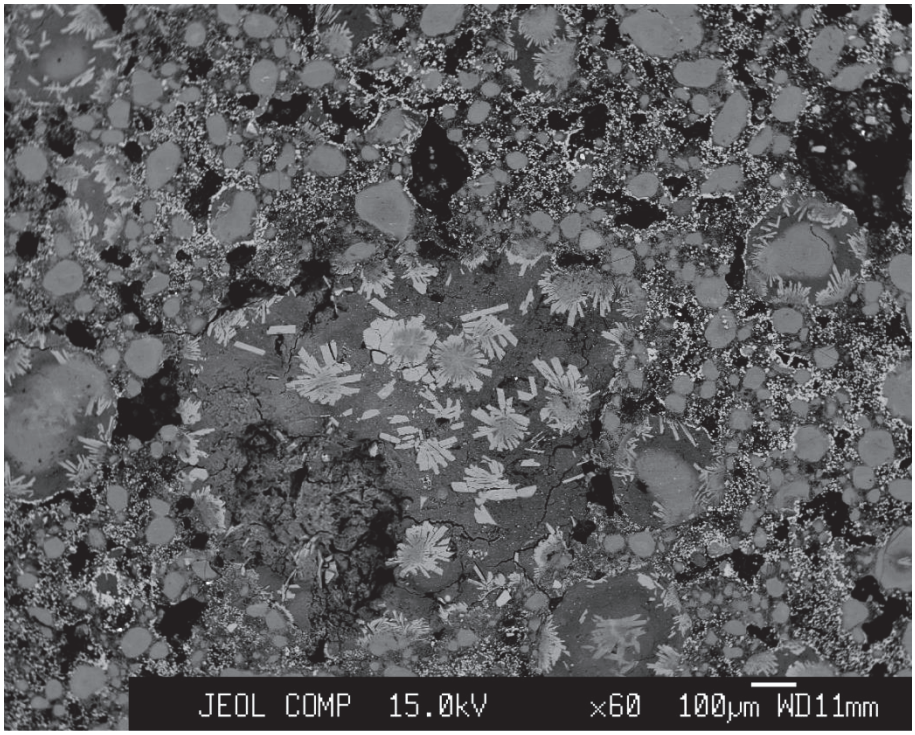

Figure 63. Backscattered electron photomicrograph of the sample hf-35b of the B-group.

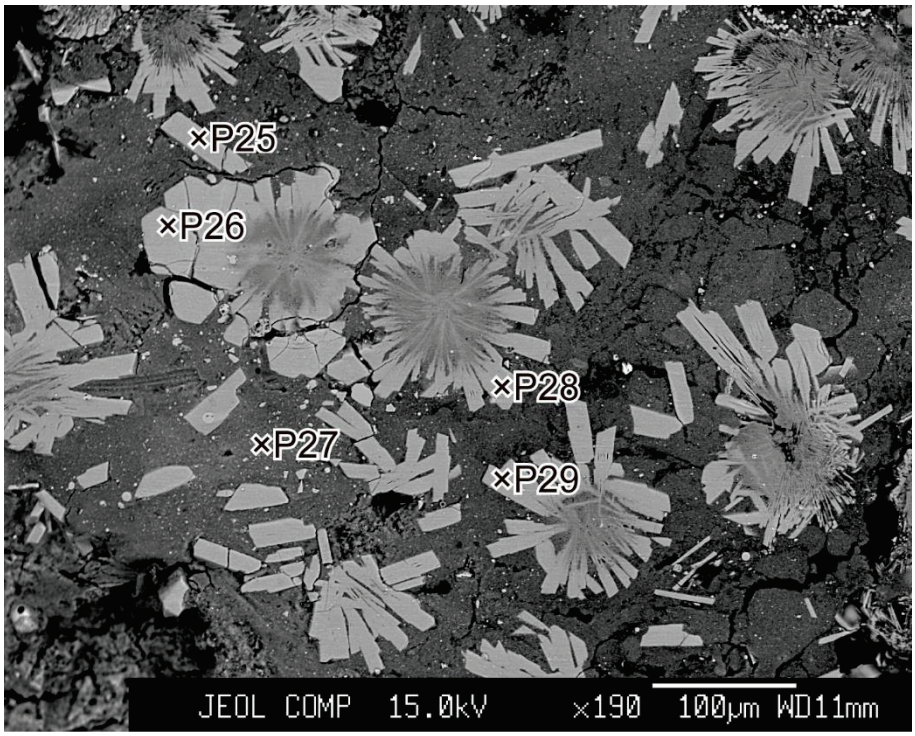

Figure 64. Backscattered electron photomicrograph of an enlarged part of the surface around center position of 9a plate. The numbers indicate analyzed points.

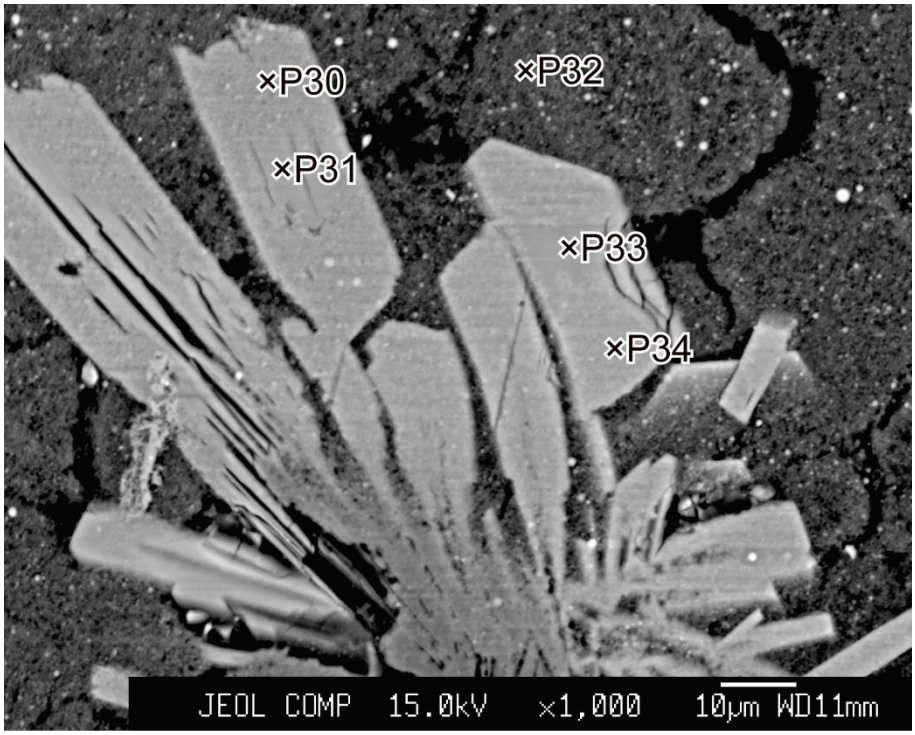

Figure 65. Backscattered electron photomicrograph of an enlarged part of the surface around right down position of 9b plate. The numbers indicate analyzed points.

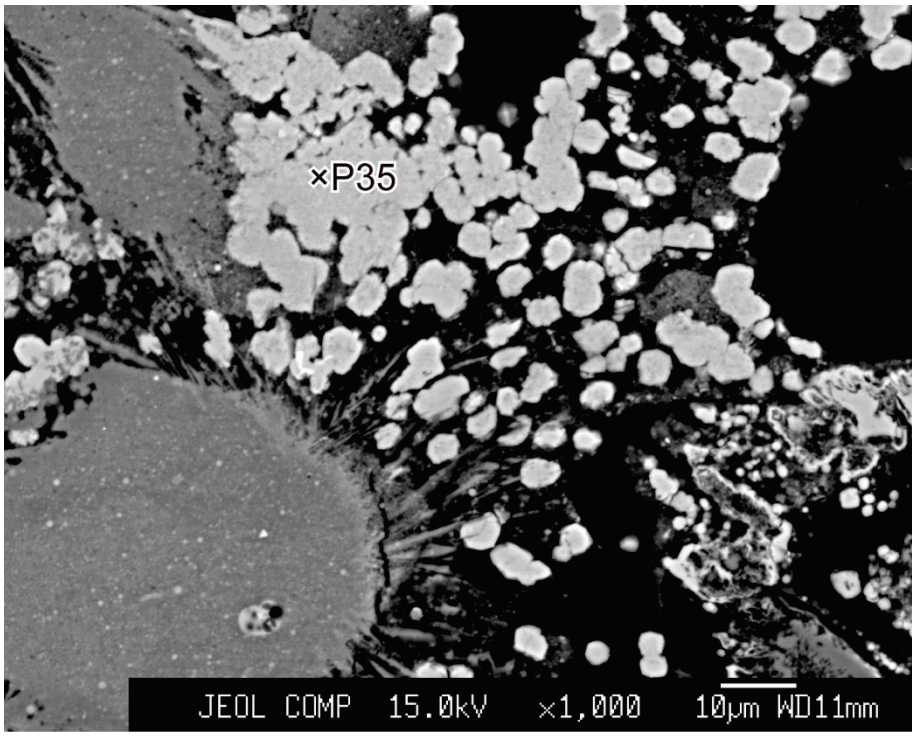

Figure 66. Backscattered electron photomicrograph of the sample hf-35b of the B-group. The number indicates analyzed point.

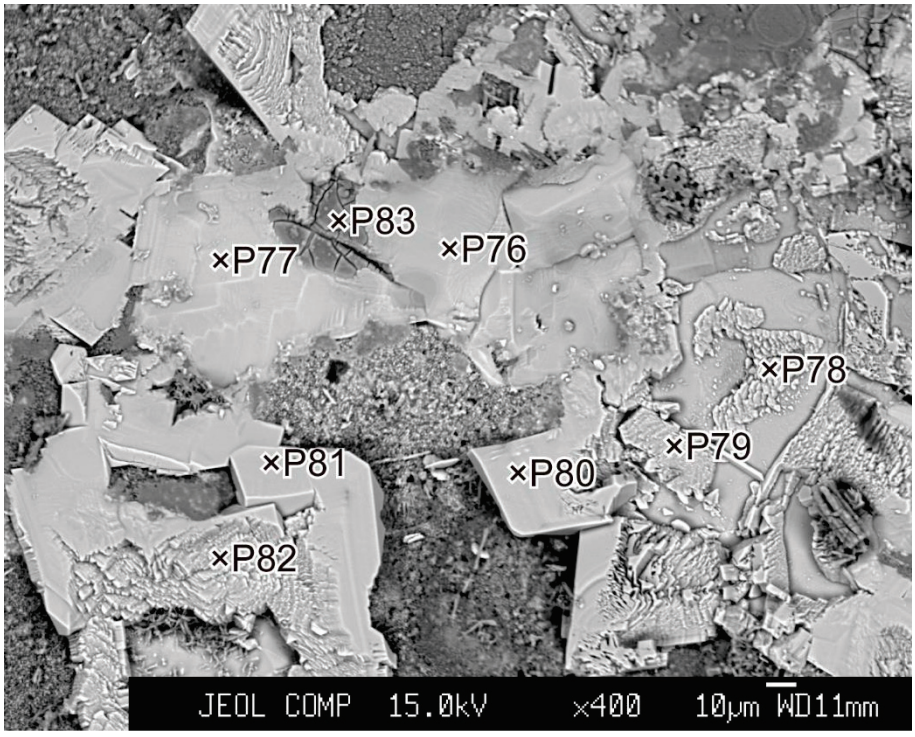

Figure 67. Backscattered electron photomicrograph of the sample hft-21p of the B-group. The numbers indicate analyzed points.

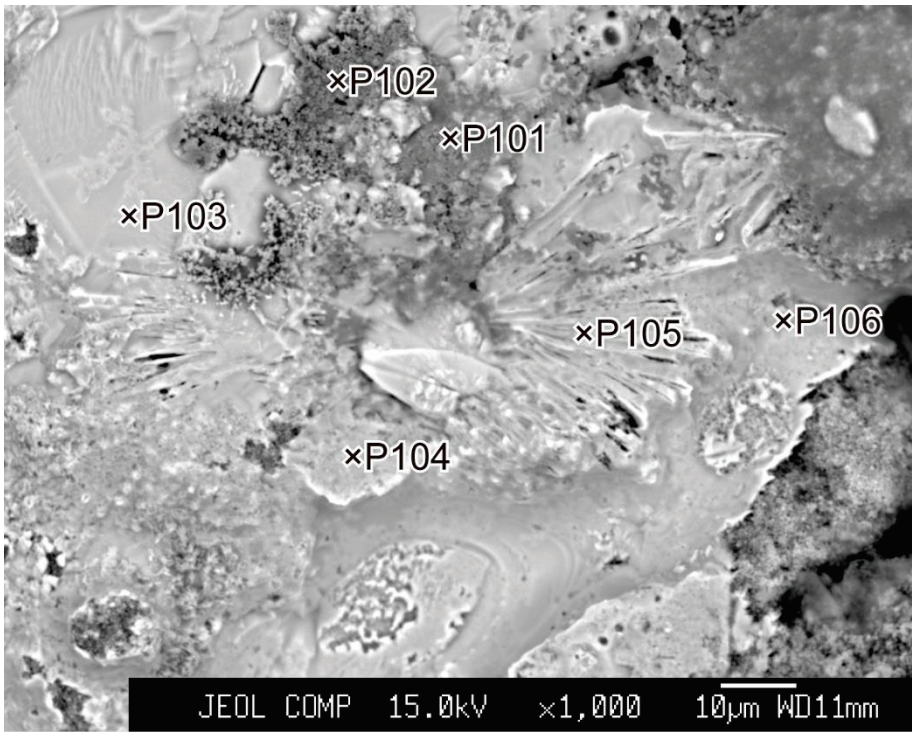

Figure 68. Backscattered electron photomicrograph of the sample hft-35p of the B-group. The numbers indicate analyzed points.

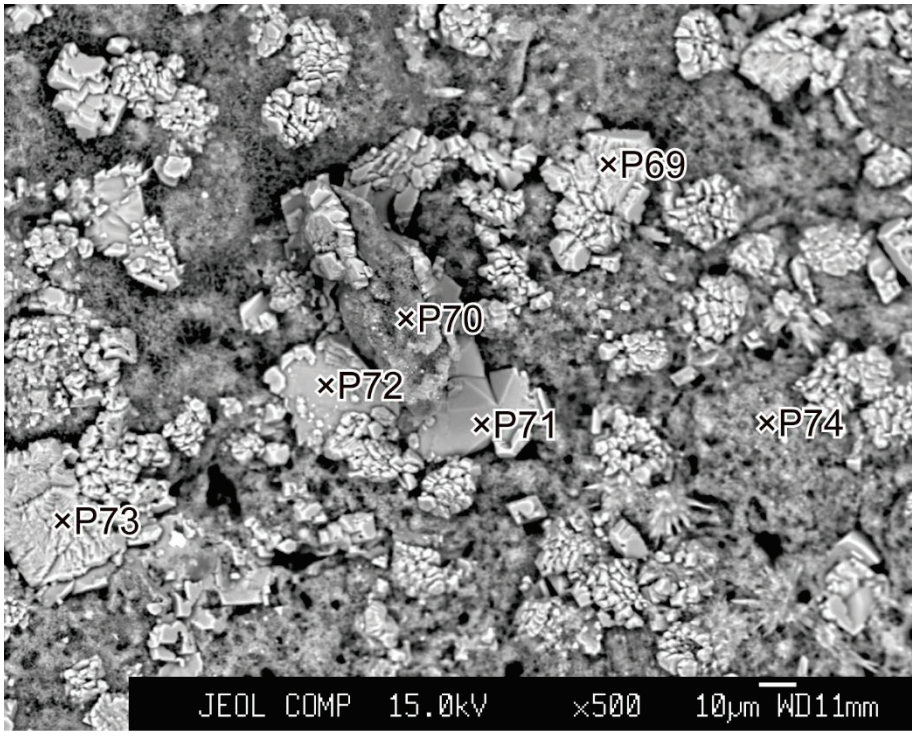

Figure 69. Backscattered electron photomicrograph of the sample hf-21p of the B-group. The numbers indicate analyzed points.

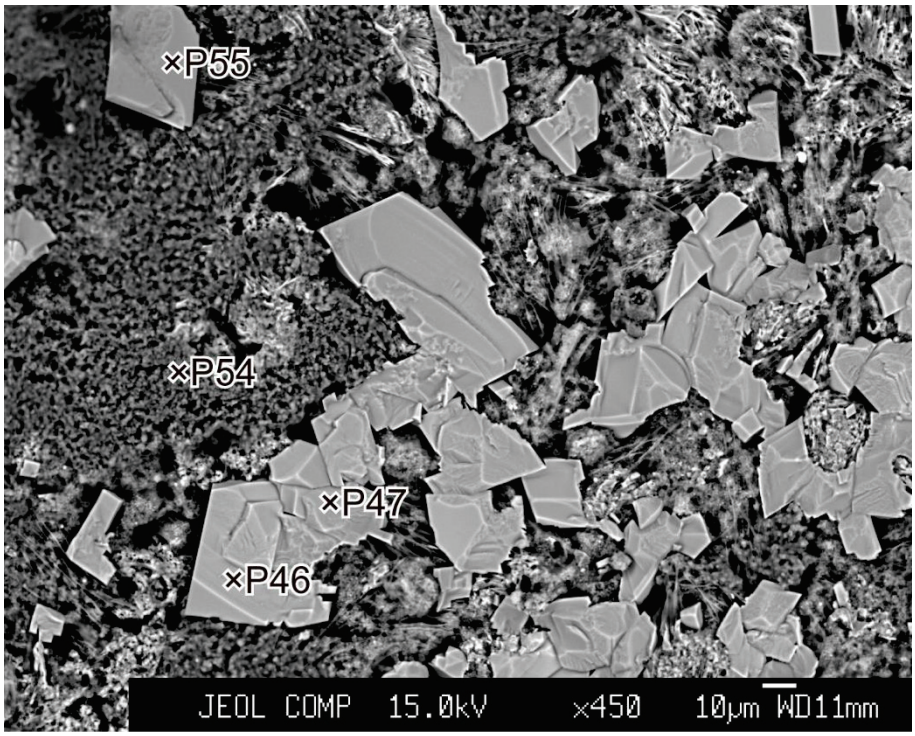

Figure 70. Backscattered electron photomicrograph of the sample hf-35p of the B-group. The numbers indicate analyzed points.

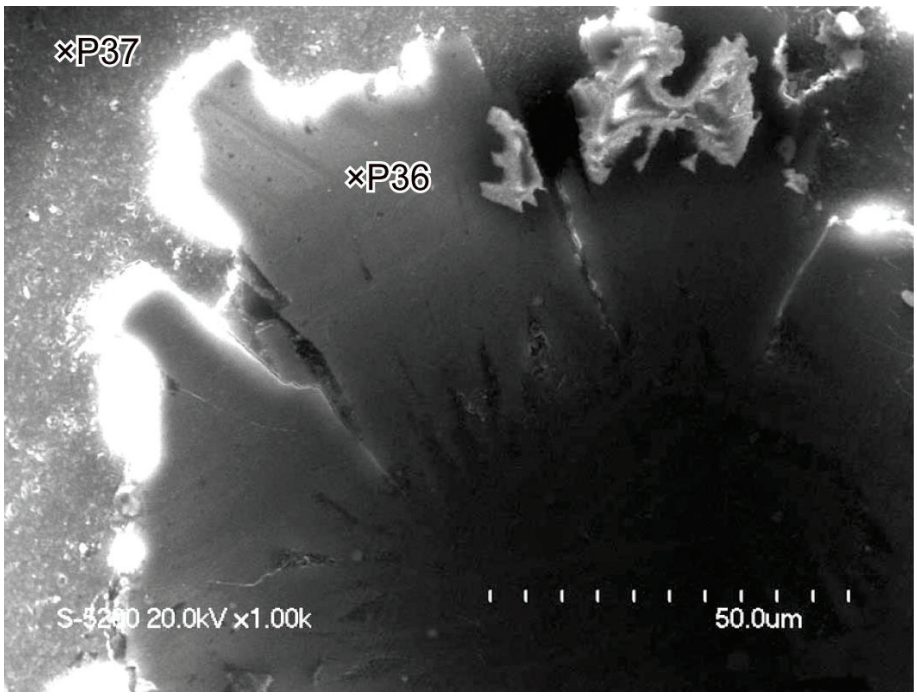

Figure 71. Secondary electron photomicrograph of the sample hf-35b of the B-group. The numbers indicate analyzed points.

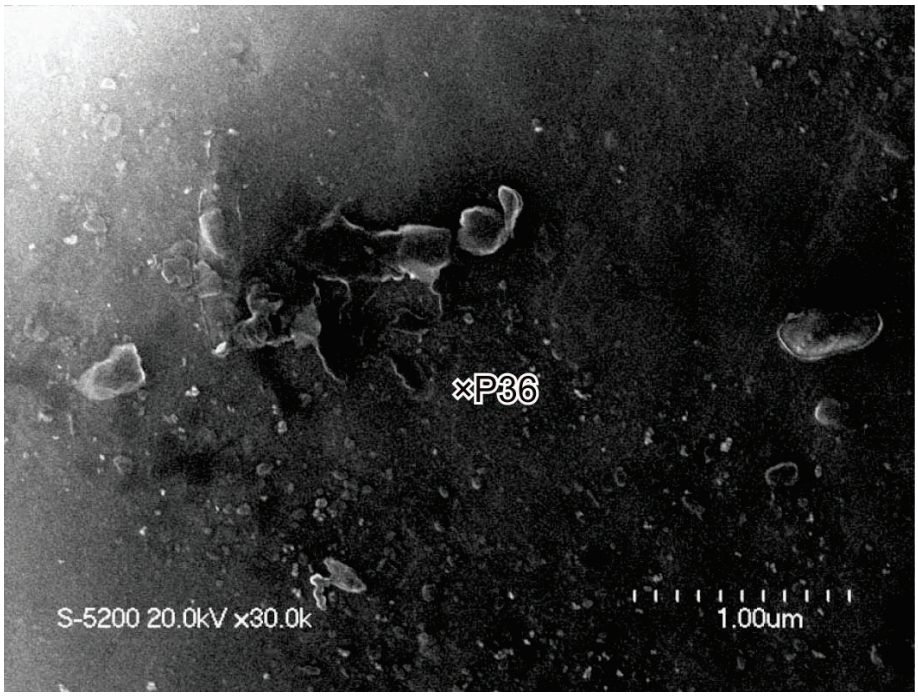

Figure 72. Secondary electron photomicrograph of an enlarged part of the surface around P36 in the sample hf-35b of the B-group. The number indicates analyzed point.

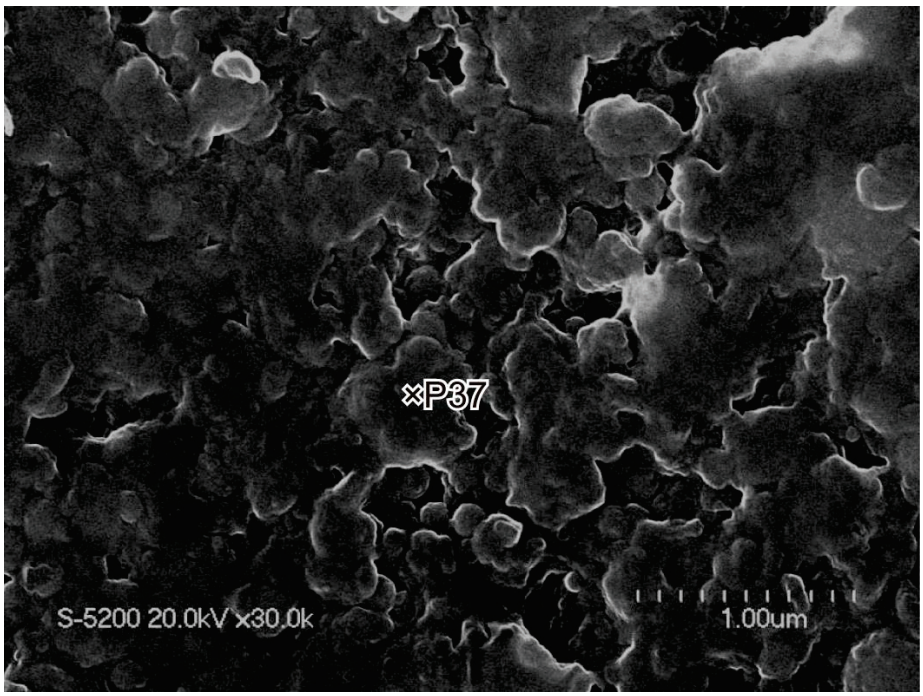

Figure 73. Secondary electron photomicrograph of an enlarged part of the surface around P36 in the sample hf-35b of the B-group. The number indicate analyzed point.

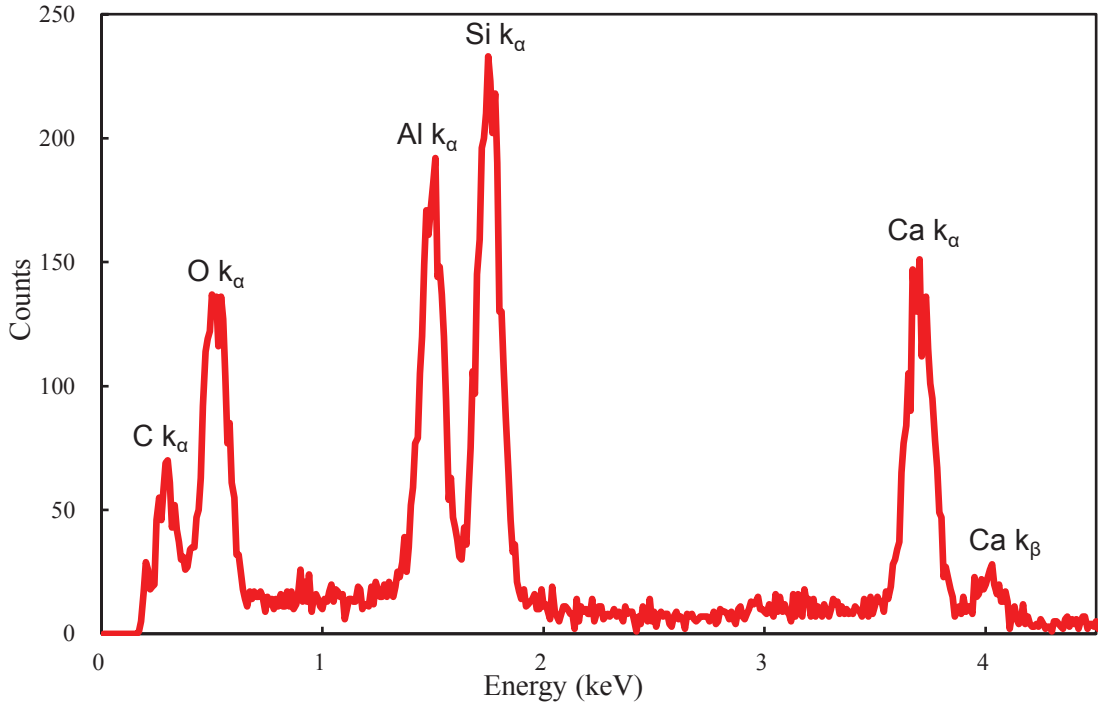

Figure 74. Result of EDX elemental analysis on the P36 in the figures71 and 72. Peaks for elements are noted.

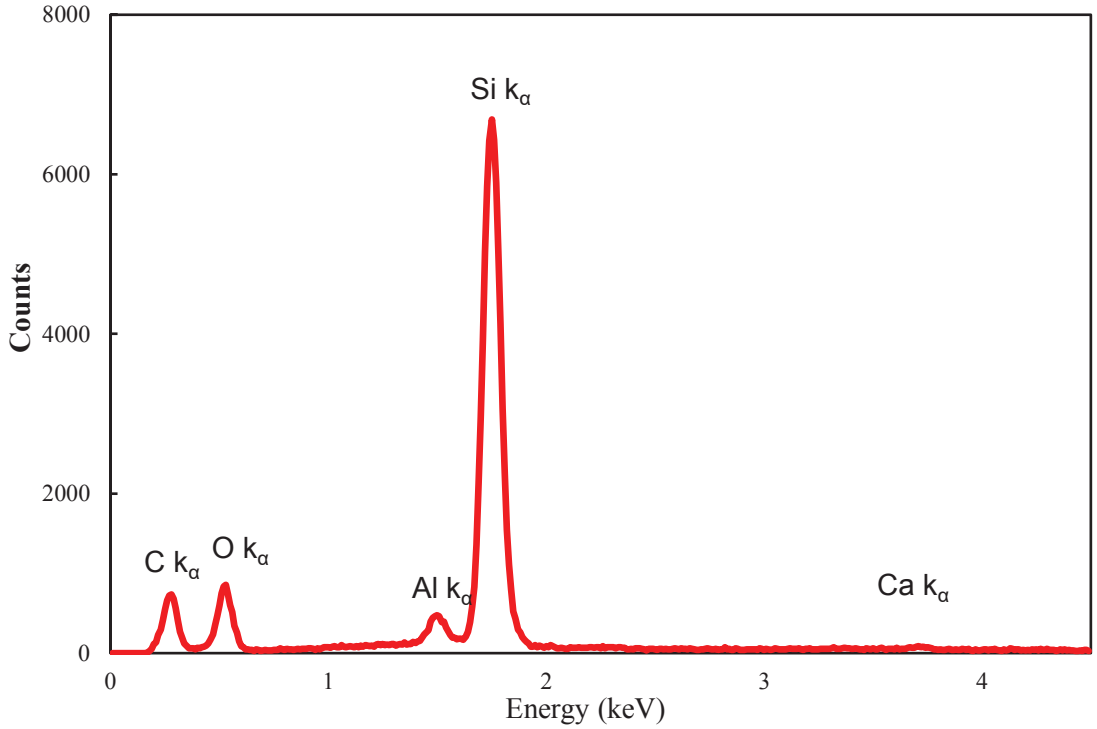

Figure 75. Result of EDX elemental analysis on the P37 in the figure 73.

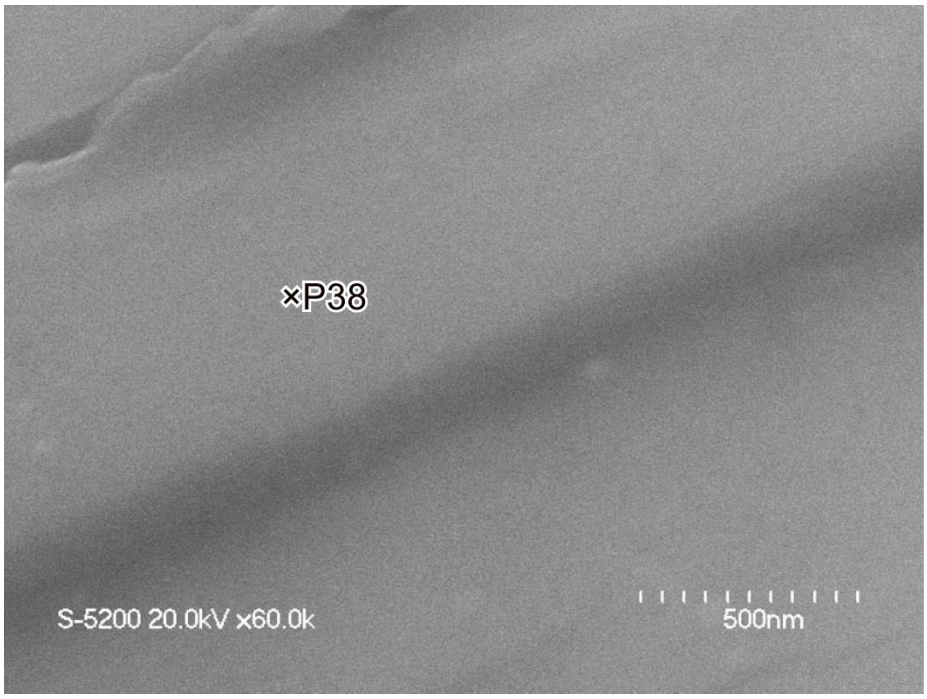

Figure 76. Secondary electron photomicrograph of the sample hf-35b of the B-group. The number indicates analyzed point.

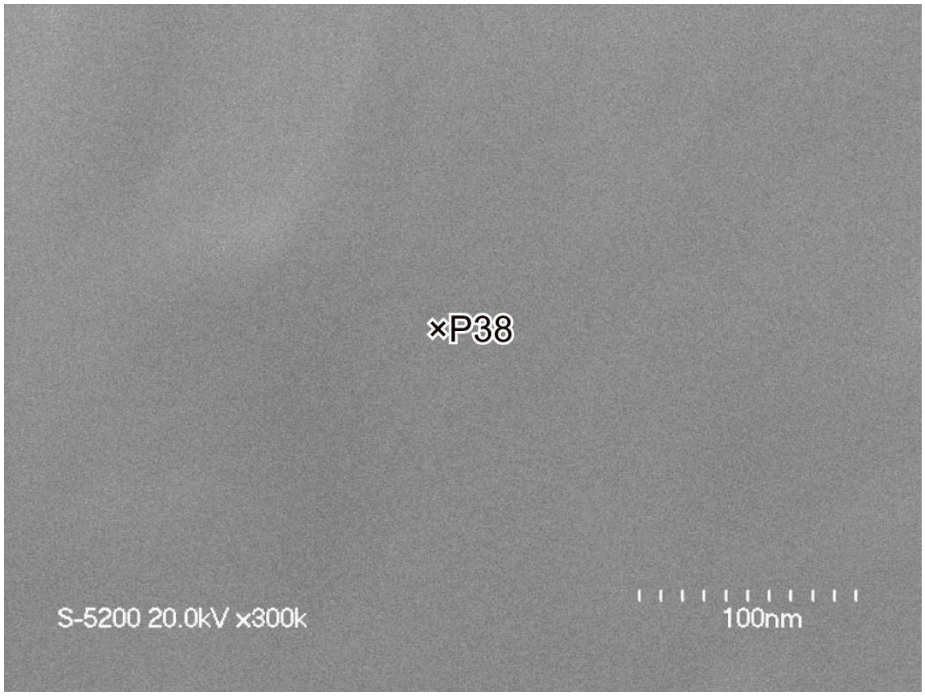

Figure 77. Secondary electron photomicrograph of an enlarged part of the surface around P38 in the sample hf-35b of the B-group.

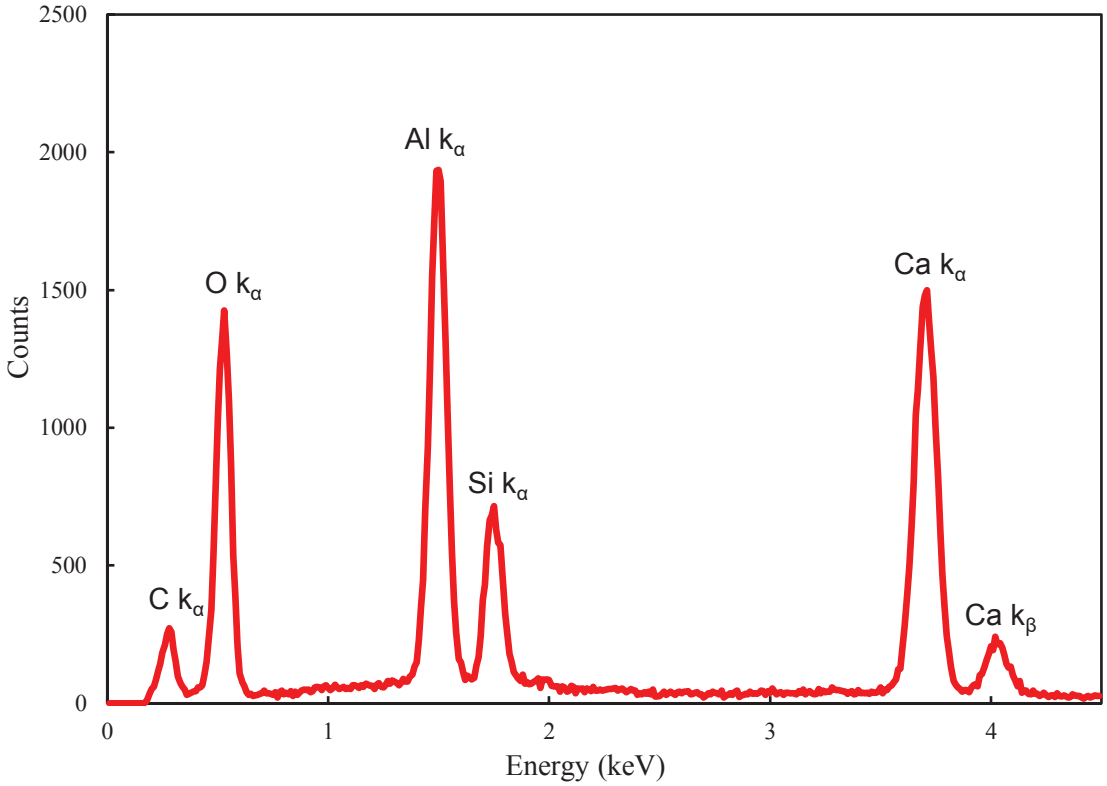

Figure 78. Result of EDX elemental analysis on the P38 in the figures 76 and 77.